

November 12, 2024

Electrostatics of Salt-Dependent Reentrant Phase Behaviors Highlights Diverse Roles of ATP in Biomolecular Condensates

Yi-Hsuan LIN,^{1,2,†,§} Tae Hun KIM,^{1,2,3,4,†,§} Suman DAS,^{1,5,§} Tanmoy PAL,¹
Jonas WESSÉN,¹ Atul Kaushik RANGADURAI,^{1,2,3,4} Lewis E. KAY,^{1,2,3,4}
Julie D. FORMAN-KAY^{2,1} and Hue Sun CHAN^{1,*}

¹Department of Biochemistry, University of Toronto, Toronto, Ontario M5S 1A8, Canada

²Molecular Medicine, Hospital for Sick Children, Toronto, Ontario M5G 0A4, Canada

³Department of Molecular Genetics, University of Toronto,
Toronto, Ontario M5S 1A8, Canada

⁴Department of Chemistry, University of Toronto, Toronto, Ontario M5S 3H6, Canada

⁵Department of Chemistry, Gandhi Institute of Technology and Management,
Visakhapatnam, Andhra Pradesh 530045, India

[†]Present address: HTuO Biosciences, 1001 West Broadway, Suite 300, Vancouver, British Columbia V6H 4B1, Canada.

[‡]Present address: Department of Biochemistry, School of Medicine,
Case Western Reserve University, Cleveland, Ohio 44106, U.S.A.

[§]Contributed equally.

^{*}Correspondence information:

Hue Sun CHAN. E-mail: huesun.chan@utoronto.ca

Tel: (416)978-2697; Fax: (416)978-8548

Department of Biochemistry, University of Toronto, Medical Sciences Building – 5th Fl.,
1 King's College Circle, Toronto, Ontario M5S 1A8, Canada.

Abstract

Liquid-liquid phase separation (LLPS) involving intrinsically disordered protein regions (IDRs) is a major physical mechanism for biological membraneless compartmentalization. The multifaceted electrostatic effects in these biomolecular condensates are exemplified here by experimental and theoretical investigations of the different salt- and ATP-dependent LLPSs of an IDR of messenger RNA-regulating protein Caprin1 and its phosphorylated variant pY-Caprin1, exhibiting, e.g., reentrant behaviors in some instances but not others. Experimental data are rationalized by physical modeling using analytical theory, molecular dynamics, and polymer field-theoretic simulations, indicating that interchain ion bridges enhance LLPS of polyelectrolytes such as Caprin1 and the high valency of ATP-magnesium is a significant factor for its colocalization with the condensed phases, as similar trends are observed for other IDRs. The electrostatic nature of these features complements ATP's involvement in π -related interactions and as an amphiphilic hydrotrope, underscoring a general role of biomolecular condensates in modulating ion concentrations and its functional ramifications.

Significance Statement

A major contributing mechanism in the assembly of biomolecular condensates is liquid-liquid phase separation. Here, a combined experimental-theoretical approach elucidates how phase behaviors of intrinsically disordered protein regions (IDRs) are affected by their amino acid sequences—including charge, aromatic and phosphorylation patterns—as well as ATP and the valencies of salt ions in the aqueous milieu. Significant electrostatic effects are highlighted by the consistency between our theoretical and experimental results for an IDR of translation-regulating protein Caprin1, including strong partitioning of ATP into the Caprin1 condensate. This physical perspective and the efficient computational approaches developed here should offer general insights into condensates scaffolded by polyampholytic and polyelectrolytic IDRs, including their potential functional role in regulating ion concentrations for biochemical reactions.

Introduction

Broad-based recent efforts have uncovered many intriguing features of biomolecular condensates, revealing and suggesting myriad known and potential biological functions [1–3]. These assemblies are underpinned substantially, though not exclusively, by liquid-liquid phase separation (LLPS) of intrinsically disordered regions (IDRs) as well as folded domains of proteins and nucleic acids [4, 5], while more complex equilibrium and non-equilibrium mechanisms also contribute [6–14].

Electrostatics plays major roles in biophysical and biochemical processes [15, 16]. Because of the relatively high compositions of charge residues in IDRs, electrostatics is particularly important for IDR LLPS [17, 18], which is often also facilitated by π -related interactions [19, 20], hydrophobicity, hydrogen bonding [21, 22], and is modulated by temperature [7, 23], hydrostatic pressure [4, 24], osmolytes [4], RNA [25–28], salt, pH [29], molecular crowding [30–32] and post-translational modifications (PTMs) [1, 33–35]. Multivalency underlies many aspects of IDR properties [36–40]. Here, we focus primarily on how PTM- and salt-modulated multivalent charge-charge interactions might alter IDR condensate behaviors and their possible functional ramifications. In general, electrostatic effects on IDR LLPS [17, 27, 29, 41] are dependent upon their sequence charge patterns [42–48]. Intriguingly, some IDRs undergo reentrant phase separation [4] or dissolution [49] when temperature, pressure [4], salt [50, 51], RNA [49, 52], or concentrations of small molecules such as heparin [53] is varied. Reentrance, especially when induced by salt and RNA, suggest a subtle interplay between multivalent sequence-specific charge-charge interactions and hydrophobic, non-ionic [50, 51], cation- π [49, 52], or π - π interactions.

An important modulator of biomolecular LLPS is adenosine triphosphate (ATP). As energy currency, ATP hydrolysis is utilized to synthesize or break chemical bonds and drive transport to regulate “active liquid” properties such as concentration gradients and droplet sizes [9, 54]. Examples include ATP-driven assembly of stress granules [55], splitting of bacterial biomolecular condensates [56], and destabilization of nucleolar aggregates [57]. ATP can also influence biomolecular LLPS without hydrolysis, akin to other LLPS promoters or suppressors [58, 59] that are effectively ligands of the condensate scaffold [60], or through ATP’s effect on lowering free $[Mg^{2+}]$ [61]. Notably, as an amphiphilic hydrotrope [62] with intracellular concentrations much higher than that required for an energy source, ATP is also seen to afford an important function independent of hydrolysis by solubilizing proteins, preventing LLPS and destabilizing aggregates, as exemplified by measurements on several proteins including fused in sarcoma (FUS) [63].

Subsequent investigations indicate, however, that hydrolysis-independent [ATP] effects on biomolecular LLPS are neither invariably monotonic for a given system nor universal across different systems. For instance, ATP promotes, not suppresses, LLPS of an IgG1 antibody [64], basic IDPs [65], and enhances LLPS of full-length and the C-terminal domain (CTD) of FUS at low [ATP] but prevents LLPS at high [ATP] [66]. The latter reentrant behavior has been surmised to arise from ATP binding bivalently [66, 67] or trivalently [68] to charged residues arginine (R) or lysine (K) by a combination of cation- π and electrostatic interactions, an effect also seen in the ATP-mediated LLPS of basic IDPs [65]. A similar scenario was invoked for the reentrant phase behavior of transactive response DNA-binding protein of 43 kDa (TDP-43) [69].

While π -related interactions are important for biomolecular LLPS in general [19, 20] and their interplay with electrostatics likely underlies reentrant biomolecular phase behaviors modulated by RNA [49, 52] or simple salts [50], the degree to which electrostatics alone can, in large measure, rationalize hydrolysis-independent ATP-modulated biomolecular phase reentrance has not been sufficiently appreciated. This question deserves attention. For instance, the suppression of cold-inducible RNA-binding protein condensation by ATP has been suggested to be electrostatically driven [70]. The aforementioned ATP-modulated reentrant phase behavior of FUS [66, 67] is reminiscent of the 236-residue N-terminal IDR of DEAD-box RNA helicase Ddx4's lack of LLPS at low [NaCl] (< 15–20 mM), LLPS at higher [NaCl] [71] and decreasing LLPS propensity when [NaCl] is further increased [17, 18]. Indeed, the finding that FUS CTD (net charge per residue (NCPR) = 15/156 = 0.096) exhibits ATP-dependent reentrant phase behaviors while the N-terminal domain (NCPR = 3/267 = 0.011) does not [67] is consistent with electrostatics-based theory for the difference in salt-dependent LLPS of polyelectrolytes and polyampholytes [71] and a recent atomic simulation study of direct and indirect salt effects on LLPS [72].

With this in mind, we seek to delineate the degree to which theories focusing primarily on electrostatics can rationalize experimental ATP-related LLPS data on the 103-residue C-terminal IDR of human cytoplasmic activation/proliferation-associated protein-1 (Caprin1). Full-length Caprin1 (709 amino acid residues) is a ubiquitously expressed phosphoprotein that regulates stress [73–76] and neuronal [77] granules, is necessary for normal cellular proliferation [78, 79], and may be essential for long-term memory [80]. Caprin1 dysfunction leads to multiple diseases such as nasopharyngeal carcinoma [81] as well as language impairment and autism spectrum disorder [82], via, e.g., Caprin1's modulation of the function of the fragile X mental retardation protein (FMRP) [26, 33, 77]. The C-terminal 607–709 Caprin1 IDR, referred to simply as Caprin1 below, is biophysically and functionally significant: It is sufficient for LLPS in vitro [33], important for assembling stress granules in the cell [73, 74], and has a substantial body of experiments [33, 83–85] for comparison with theory. Since tyrosine phosphorylations of Caprin1 in vivo [86] may regulate translation in neurons [33], the Caprin1 system is also useful for gaining insights into phosphorregulation of biomolecular condensates [87–89].

Recent advances in theory and computation enable modeling of sequence-specific IDR LLPS [18, 72, 88, 90–96]. Among the approaches, polymer chain models of IDRs are inherently more realistic in capturing sequence properties than models without a chain description such as patchy particle theory [58]. For chain models, all-atom simulation offer a high degree of geometric and energetic realism but its high computational cost often makes it difficult to achieve sufficient sampling and equilibration for the large system sizes that are needed for modeling biomolecular LLPS [72]. However, even coarse-grained explicit-chain simulation affords more realistic geometric and energetic representations than analytical theory, but analytical theory offers significant advantages in numerical tractability [97]. For our present purposes, the analytical rG-RPA formulation [71], which synthesizes Kuhn-length renormalization (renormalized Gaussian, rG) and random phase approximation (RPA) [18] to treat both high-net-charge polyelectrolytes and essentially net-neutral polyampholytes [71], is particularly well suited for Caprin1 and its phosphorylated variant pY-Caprin1. To gain deeper insights into the pertinent physical

principles and to assess possible limitations of this analytical approximation, we further leverage a methodological combination of rG-RPA [71], field-theoretic simulation (FTS) [91, 98], and coarse-grained explicit-chain molecular dynamics (MD) [88, 94] to better elucidate the effects of salt, phosphorylation, and ATP on LLPS of Caprin1 and pY-Caprin1.

Results

Overview of key observations from complementary approaches

The complementary nature of our multiple methodologies allows us to focus sharply on the electrostatic aspects of hydrolysis-independent role of ATP in biomolecular condensation by comparing ATP's effects with those of simple salt. Here, Caprin1 and pY-Caprin1 are modeled minimally as heteropolymers of charged and neutral beads in rG-RPA and FTS. ATP and ATP-Mg are modeled as simple salts (single-bead ions) in rG-RPA whereas they are modeled with more structural complexity as short charged polymers (multiple-bead chains) in FTS, though the latter models are still highly coarse-grained. Despite this modeling difference, rG-RPA and FTS both rationalize experimentally observed ATP- and NaCl-modulated reentrant LLPS of Caprin1 and a lack of a similar reentrance for pY-Caprin1 as well as a prominent colocalization of ATP with the Caprin1 condensate. Consistently, the same contrasting trends in the effect of NaCl on Caprin1 and pY-Caprin1 are also seen in our coarse-grained MD simulations, though polymer field theories tend to overestimate LLPS propensity [99]. The robustness of the theoretical trends across different modeling platforms underscores electrostatics as a significant component in the diverse roles of ATP in the context of its well-documented ability to modulate biomolecular LLPS via hydrophobic and π -related effects [63, 65, 67]. Analyses of these other nonelectrostatic effects are mostly beyond the scope of the present work but their impact are nevertheless illustrated by the Flory-Huggins interactions augmented to rG-RPA to quantitatively account for experimental data and our MD simulation of the arginine-to-lysine Caprin1 mutants. These findings are detailed below.

Physical theories of Caprin1 and phosphorylated Caprin1 LLPSs as those of polyelectrolytes and polyampholytes

The 103-residue Caprin1 is a highly charged IDR with 19 charged residues [Fig. 1a and *Supporting Information (SI Appendix)*, Fig. S1]: 15 R, 1 K, and 3 aspartic acids (D); fraction of charged residues = $19/103 = 0.184$ and NCPR = $13/103 = 0.126$. With a substantial positive net charge, Caprin1's phase behaviors are markedly different from those of polyampholytic IDRs with nearly zero net charge such as Ddx4 to which early sequence-specific LLPS theories were targeted [17, 18]. Instead, Caprin1 behaves like chemically synthesized polyelectrolytes [100]. In contrast, when most or all of the 7 tyrosines (Y) in the Caprin1 IDR are phosphorylated (pY), negative charges are added to produce a near-net-neutral polyampholyte. Mass spectrometry indicates that the experimental sample of highly phosphorylated Caprin1 consists mainly of a mixture of IDRs with 6 or 7 phosphorylations (*SI Appendix*, Fig. S2). We refer to this experimental sample as pY-Caprin1 below. For simplicity, we use only the Caprin1 IDR with 7 pYs to model the behavior of this experimental sample in our theoretical/computational formulations, partly to avoid the combinatoric

complexity of sequences with 5 or 6 pYs. Accordingly, since the charge of a pY is ≈ -2 at the experimental pH = 7.4, -14 charges are added to Caprin1 for our model pY-Caprin1, resulting in a polyampholyte with a very small NCPR = $-1/103 = -0.00971$ (Fig. 1b). Both the experimental pY-Caprin1 (NCPR $\approx \pm 1/103 = \pm 0.00971$) and model pY-Caprin1 are expected to exhibit phase properties similar to other polyampholytic IDRs.

While sequence-specific RPA has been applied successfully to model electrostatic effects on the LLPSs of various polyampholytic IDRs [7, 18, 44, 94, 101], RPA is less appropriate for polyelectrolytes with large NCPR [102–104] because of its treatment of polymers as ideal Gaussian chains [105]. Traditionally, theories for polyelectrolytes tackle their peculiar conformations by various renormalized blob constructs [100, 102], two-loop polymer field theory [106], modified thermodynamic perturbation theory [107], and renormalized Gaussian fluctuation (RGF) theory [99, 108], among others. As such, these formulations are mostly designed for homopolymers, making it difficult to apply directly to heteropolymeric biopolymers. In order to analyze Caprin1 and pY-Caprin1 LLPSs, we utilize rG-RPA [71], which combines Gaussian chains of effective (renormalized) Kuhn length with the key idea of RGF [43].

Phase properties predicted by rG-RPA theory for Caprin1 and pY-Caprin1 with monovalent counterions and salt are in agreement with experiment

Fig. 1c and d show that the salt- and temperature (T)-dependent phase diagrams predicted by rG-RPA with an augmented Flory-Huggins (FH) mean-field $\chi(T) = \epsilon_h/T^* + \epsilon_s$ parameter for nonelectrostatic interactions, where ϵ_h and ϵ_s are the enthalpic and entropic contributions, respectively, and T^* is reduced temperature [18, 71] (Eq. 10 of ref. [18] and “rG-RPA+FH” theory in *SI Appendix*), are in reasonable agreement with experiment using bulk [Caprin1] (initial overall concentration) $\approx 200 \mu\text{M}$. (Concentrations are provided in molarity and also as mass density in Fig. 1 and subsequent figures). The rG-RPA+FH results in Fig. 1c indicate that (i) Caprin1 undergoes LLPS below 20°C with 100 mM NaCl, and that (ii) LLPS propensity, quantified by the upper critical solution temperature (UCST), increases with [NaCl]. These predictions are consistent with experimental data, including the observation that Caprin1 does not phase separate at room temperature without salt, ATP, RNA or other proteins, though Caprin1 LLPS can be triggered by adding wildtype (WT) and phosphorylated FMRP and/or RNA (overall [Caprin1] $\gtrsim 10 \mu\text{M}$) [33], NaCl [83], or ATP (overall [Caprin1] = 400 μM) [84]. The trend here is also in line with other theories of polyelectrolytes [108]. In contrast, rG-RPA+FH results in Fig. 1d for pY-Caprin1 shows decreasing LLPS propensity with increasing [NaCl], consistent with experimental data and the expected salt dependence of LLPS of nearly net-neutral polyampholytic IDRs such as Ddx4 [18].

Interestingly, the decrease in some of the condensed-phase [pY-Caprin1]s with decreasing T (orange and green symbols for $\lesssim 20^\circ\text{C}$ in Fig. 1d trending toward slightly lower [pY-Caprin1]) may suggest a hydrophobicity-driven lower critical solution temperature (LCST)-like reduction of LLPS propensity as temperature approaches $\sim 0^\circ\text{C}$ as in cold denaturation of globular proteins [7, 23] though the hypothetical LCST is below 0°C and therefore not experimentally accessible. If that is the case, the LLPS region would resemble those with both an UCST and a LCST [4]. As far as simple modeling is

concerned, such a feature may be captured by a FH model wherein interchain contacts are favored by entropy at intermediate to low temperatures and by enthalpy at high temperatures, thus entailing a heat capacity contribution in $\chi(T)$, with $\epsilon_h \rightarrow \epsilon_h(T)$, $\epsilon_s \rightarrow \epsilon_s(T)$ [7, 109, 110], beyond the temperature-independent ϵ_h and ϵ_s used in Fig. 1c,d and Fig. 2. Alternatively, a reduction in overall condensed-phase concentration can also be caused by formation of heterogeneous locally organized structures with large voids at low temperatures even when interchain interactions are purely enthalpic (Fig. 4 of ref. [111]).

Salt-IDR two-dimensional phase diagrams are instrumental for exploring broader phase properties

Fig. 1c and d, though informative, are computed by a restricted rG-RPA+FH that assumes a spatially uniform $[\text{Na}^+]$. For a more comprehensive physical picture, we now examine possible differences in salt concentration between the IDR-dilute and condensed phases by applying unrestricted rG-RPA+FH to compute two-dimensional salt-Caprin1/pY-Caprin1 phase diagrams (Fig. 2).

As stated in *Materials and Methods* and *SI Appendix*, here we define “counterions” and “salt ions”, respectively, as the small ions with charges opposite and identical in sign to that of the net charge, Q , of a given polymer. For the Caprin1/NaCl system, since Caprin1’s net charge is positive, Na^+ is salt ion and Cl^- is counterion. Overall electric neutrality of the system implies that the concentrations (ρ ’s) of polymer (ρ_p), counterions (ρ_c), and salt ions (ρ_s) are related by

$$|Q|\rho_p + z_s\rho_s = z_c\rho_c, \quad (1)$$

where z_s and z_c are, respectively, the valencies of salt ions and counterions. For Caprin1 and pY-Caprin1, $Q = +13$ and -1 , respectively, and $(z_s, z_c) = (1, 1)$, $(1, 2)$, and $(2, 4)$ are models for different small-ion species in the system. Specifically, in Fig. 2, we identify the $z_s = 1$ salt ion as Na^+ (Fig. 2a–f) and the $z_c = 1$ counterion as Cl^- (Fig. 2a–d), the $z_c = 2$ counterion as $(\text{ATP-Mg})^{2-}$ (Fig. 2g,h), the $z_s = 2$ salt ion as Mg^{2+} and the $z_c = 4$ counterion as ATP^{4-} (Fig. 2i–l). As mentioned above, in the present rG-RPA formulation, $(\text{ATP-Mg})^{2-}$ and ATP^{4-} are modeled minimally as a single-bead ion. They are represented by charged polymer models with more structural complexity in the FTS models below.

Behavioral trends of rG-RPA-predicted Na^+ -Caprin1 two-dimensional phase diagrams are consistent with experiment

Notably, Fig. 2a,b ($z_s = z_c = 1$) predicts that Caprin1 does not phase separate without Na^+ , consistent with experiment, indicating that monovalent counterions alone (Cl^- in this case) are insufficient for Caprin1 LLPS. When $[\text{Na}^+]$ is increased, the system starts to phase separate at a small $[\text{Na}^+] \lesssim 0.1$ M, with LLPS propensity increasing to a maximum at $[\text{Na}^+] \sim 1$ M before decreasing at higher $[\text{Na}^+]$, in agreement with experiment (Fig. 3a, blue data points) and consistent with Caprin1 LLPS propensity increasing with $[\text{NaCl}]$ from 0.1 to 0.5 M (Fig. 1c). The predicted reentrant dissolution of Caprin1 condensate at high $[\text{Na}^+]$ in Fig. 2a is consistent with measurement up to $[\text{Na}^+] \approx 4.6$ M indicating a significant decrease in LLPS propensity when $[\text{Na}^+] \gtrsim 2.5$ M (Fig. 3a), though the gradual decreasing trend suggests that complete dissolution of condensed droplets is not likely even when NaCl reaches its saturation concentration of ~ 6 M.

The negative tieline slopes in Fig. 2a,b predict that Na^+ is partially excluded from the Caprin1 condensate. This “salt partitioning” is most likely caused by Caprin1’s net positive charge and is consistent with published research on polyelectrolytes with monovalent salt [108, 112, 113]. Here, the rG-RPA predicted trend is consistent with our experiment showing significantly reduced $[\text{Na}^+]$ in the Caprin1-condensed phase compared to the Caprin1-dilute phase (Table 1), although the larger experimental reduction of $[\text{Na}^+]$ in the Caprin1 condensed droplet relative to our theoretical prediction remains to be elucidated. In contrast, for the near-neutral, very slightly negative model pY-Caprin1 (Fig. 2c,d), rG-RPA predicts LLPS at $[\text{Na}^+] \approx 0$, and the positive tieline slopes indicate that $[\text{Na}^+]$ is higher in the condensed than in the dilute phase. Consistent with Fig. 1d, Fig. 2c shows that pY-Caprin1 LLPS propensity always decreases with increasing $[\text{Na}^+]$.

rG-RPA-predicted salt-IDR two-dimensional phase diagrams underscore effects of counterion valency on LLPS

Interestingly, a different salt dependence of Caprin1 LLPS is predicted when the salt ion remains monovalent but the monovalent counterion Cl^- is replaced by a divalent $z_c = 2$ anion modeling $(\text{ATP-Mg})^{2-}$ (as a one-bead ion) under the simplifying assumption that ATP^{4-} and Mg^{2+} do not dissociate in solution. The corresponding rG-RPA results (Fig. 2e–h) indicate that, in the present of divalent counterions (needed for overall electric neutrality of the Caprin1 solution), Caprin1 can undergo LLPS without the monovalent salt (Na^+) ions (LLPS regions extend to $[\text{Na}^+] = 0$ in Fig. 2e,f; i.e., $\rho_s = 0$, $\rho_c > 0$ in Eq. (1)), because the configurational entropic cost of concentrating counterions in the Caprin1 condensed phase is lesser for divalent ($z_c = 2$) than for monovalent ($z_c = 1$) counterions as only half of the former are needed for approximate electric neutrality in the condensed phase.

Other predicted differences between monovalent (Fig. 2a,b) and divalent (Fig. 2e,f) counterions’ impact on Caprin1 LLPS include: (i) The maximum condensed-phase [Caprin1] at low $[\text{Na}^+]$ is lower with monovalent than with divalent counterions ($[\text{Caprin1}] \sim 40 \text{ mM}$ vs. $\sim 70 \text{ mM}$). (ii) The $[\text{Na}^+]$ at the commencement of reentrance (i.e., at the maximum condensed-phase [Caprin1]) is much higher with monovalent than with divalent counterions ($[\text{Na}^+] \sim 1 \text{ M}$ vs. $\sim 0.1 \text{ M}$). (iii) $[\text{Na}^+]$ is depleted in the Caprin1 condensate with both monovalent and divalent counterions when overall $[\text{Na}^+]$ is high (negative tieline slopes for $[\text{Na}^+] \gtrsim 2 \text{ M}$ in Fig. 2a,e). However, for lower overall $[\text{Na}^+]$, $[\text{Na}^+]$ is slightly higher in the Caprin1 condensate with divalent but not with monovalent counterions (slightly positive tieline slopes for $[\text{Na}^+] \lesssim 2 \text{ M}$ in Fig. 2e,f). This prediction suggests that under physiological $[\text{Na}^+] = 150 \sim 170 \text{ mM}$, monovalent positive salt ions such as Na^+ can be attracted, somewhat counterintuitively, into biomolecular condensates scaffolded by positively-charged polyelectrolytic IDRs in the presence of divalent counterions. This phenomenon arises because the positively charge monovalent salt ions are attracted to the negatively charged divalent counterions in the protein-condensed phase.

rG-RPA is consistent with experimental [ATP-Mg]-dependent Caprin1 reentrant phase behaviors

For the $z_s = 2$, $z_c = 4$ case in Fig. 2i–l modeling $(\text{ATP-Mg})^{2-}$ complex dissociating completely in solution into Mg^{2+} salt ions and ATP^{4-} counterions (modeled as single-bead

ions), rG-RPA predicts Caprin1 LLPS with ATP^{4-} (Fig. 2k,l) in the absence of Mg^{2+} (the LLPS region includes the horizontal axes in Fig. 2i,j), likely because the configurational entropy loss of tetravalent counterions in the Caprin1 condensate is less than that of divalent and monovalent counterions. Tetravalent counterions also increase the theoretical maximum condensed-phase [Caprin1] to $\gtrsim 120$ mM. At the commencement of reentrance (maximum condensed-phase [Caprin1] in Fig. 2i,j), $[\text{Mg}^{2+}] \sim 0.4$ M, which is intermediate between the corresponding $[\text{Na}^+] \sim 1.0$ and 0.1 M, respectively, for monovalent and divalent counterions with $(z_s, z_c) = (1, 2)$ and $(1, 1)$. All tieline slopes for Mg^{2+} and ATP^{4-} in Fig. 2i-l are significantly positive, except in an extremely high-salt region with $[\text{Mg}^{2+}] > 8$ M, indicating that $[(\text{ATP-Mg})^{2-}]$ is almost always substantially enhanced in the Caprin1 condensate. These observations from analytical theory will be corroborated by FTS below with the introduction of structurally more realistic models of $(\text{ATP-Mg})^{2-}$, ATP^{4-} together with the possibility of simultaneous inclusion of Na^+ , Cl^- , and Mg^{2+} in the FTS models of Caprin1/pY-Caprin1 LLPS systems. Despite the tendency for polymer field theories to overestimate LLPS propensity and condensed-phase concentrations quantitatively because they do not account for ion condensation [99]—which can be severe for small ions with more than ± 1 charge valencies as in the case of condensed $[\text{Caprin1}] \gtrsim 120$ mM in Fig. 2i-l, our present rG-RPA-predicted semi-quantitative trends are consistent with experiments indicating $[\text{ATP-Mg}]$ -dependent reentrant phase behavior of Caprin1 (Fig. 3a, red data points, and Fig. 3b) and that $[\text{Mg}^{2+}]$ as well as $[\text{ATP}^{4-}]$ are significantly enhanced in the Caprin1 condensate by a factor of ~ 5 –60 for overall $[\text{ATP-Mg}] = 3$ –30 mM (Table 2).

Coarse-grained MD with explicit small ions is useful for investigating subtle salt dependence in biomolecular LLPS

To gain deeper insights, we extend the widely-utilized coarse-grained explicit-chain MD model for biomolecular condensates [88, 94, 114] to include explicit small cations and anions (*Materials and Methods*). ATP-mediated LLPS of short basic peptides was studied recently using all-atom simulations indicating ATP engaging in electrostatic and cation- π bridging interactions [65]. Here, we limit the small ions in our coarse-grained MD simulations of Caprin1 and pY-Caprin1 LLPS to Na^+ and Cl^- , focusing on the physical origins of reentrance or lack thereof as well as the effects of arginine-to-lysine (RtoK) mutations on Caprin1. Coarse-grained models allow for the study of larger systems (IDPs of longer chain lengths and more IDPs in the system), though they cannot provide insights into more subtle structural and energetic effects as in all-atom simulations [50, 65, 72]. For computational efficiency, here we neglect solvation effects that can arise from the directional hydrogen bonds among water molecules (see, e.g., ref. [115]) by treating other aspects of the aqueous solvent implicitly as in most, though not all [97, 101] applications of the methodology [88]. Several coarse-grained interaction schemes were used in recent MD simulations of biomolecular LLPS [88, 94, 96, 116–119]. Since we are primarily interested in general principles rather than quantitative details of the phase behaviors of Caprin1 and its RtoK mutants, here we adopt the Kim-Hummer (KH) energies for pairwise amino acid interactions derived from contact statistics of folded protein structures [88], which can largely capture the experimental effects of R vs K on LLPS [94].

Explicit-ion MD rationalizes experimentally observed [NaCl]-dependent Caprin1 reentrant phase behaviors and depletion of Na^+ in Caprin1 condensate
 Consistent with experiment (Fig. 3) and rG-RPA (Fig. 2a-d), explicit-ion coarse-grained MD results in Fig. 4 show [NaCl]-dependent reentrant phase behavior for Caprin1 but not for pY-Caprin1 (non-monotonic and monotonic trends indicated, respectively, by the grey arrows in Fig. 4a,b). In other words, the critical temperature T_{cr} , which is defined as the maximum temperature (UCST) of a given phase diagram (binodal, or coexistence curve), increases then decreases with addition of NaCl for Caprin1 but T_{cr} always decreases with increasing [NaCl] for pY-Caprin1. Moreover, consistent with the rG-RPA-predicted tielines in Fig. 2a-d (negative slopes for Caprin1 and positive slopes for pY-Caprin1), Fig. 4e,g show that Na^+ is slightly depleted in the Caprin1 condensed droplet, exhibiting the same trend as that in experiment (Fig. 3a, blue data points; and Table 1) but is enhanced in the pY-Caprin1 droplet (Fig. 4f,h). Because model temperatures in Fig. 4a,b and subsequent MD results are given in units of the MD-simulated T_{cr} of WT Caprin1 at [NaCl] = 0 (denoted as T_{cr}^0 here), the T_{cr} s of systems with higher or lower LLPS propensities than WT Caprin1 at zero [NaCl] is characterized, respectively, by $T_{\text{cr}}/T_{\text{cr}}^0 > 1$ or < 1 .

Fig. 4e,g show that $[\text{Cl}^-]$ is enhanced while $[\text{Na}^+]$ is depleted in the Caprin1 droplet. By comparison, Fig. 4f,h show that both $[\text{Cl}^-]$ and $[\text{Na}^+]$ are enhanced in the pY-Caprin1 droplet with an excess of $[\text{Na}^+]$ to balance the negatively charged pY-Caprin1 (Fig. 4h). The enhancement of $[\text{Cl}^-]$ in the Caprin1 condensed phase depicted in Fig. 4f,h is further illustrated in Fig. 5a-d by comparing the entire simulation box with a condensed droplet in the middle (Fig. 5a) with individual distributions of the Caprin1 IDR (Fig. 5b), Na^+ (Fig. 5c), and Cl^- (Fig. 5d). A similar trend, also attributed to charge effects, was observed in explicit-water, explicit-ion MD simulations in the presence of a preformed condensate of the N-terminal RGG domain of LAF-1 with a positive net charge [120]. For Caprin1, Fig. 5e,f suggests that, as counterion, Cl^- can coordinate two positively charged R residues and thereby stabilize indirect counterion-bridged interchain contacts among polycationic Caprin1 molecules to promote LLPS, consistent with an early lattice-model analysis of generic polyelectrolytes [104] and a recent atomic simulation study of the IDP A1-LCD [72].

Explicit-ion MD offers insights into counterion-mediated interchain bridging interactions among condensed Caprin1 molecules

To assess the extent to which Cl^- -mediated bridging interactions (as illustrated in Fig. 5f) contribute to condensation of polyelectrolytic IDRs, we examine the relative positions of positively charged arginine residues (Arg^+) and negatively charged counterions (Cl^-) of a Caprin1 solution under phase-separation conditions in which essentially all Caprin1 molecules are in the condensed phase, using 4,000 frames (MD snapshots) of an equilibrated salt-free ($[\text{NaCl}] = 0$) ensemble of 100 WT Caprin1 chains (net charge per chain = +13) with 1,300 Cl^- counterions at $T < T_{\text{cr}}^0$ as an example (Fig. 6). For simplicity, we focus on Arg^+-Cl^- interactions because the overwhelming majority (15/16) of the positively charged residues in Caprin1 are arginines. The computed radial distribution function, $\rho(r)$, of Cl^- around a given Arg^+ exhibits a sharp peak at small r that drops to a minimum at $r \approx 11 \text{ \AA}$ (Fig. 6a), indicating a strong spatial association between the oppositely charged Arg^+ and Cl^- as expected. Indeed, within the ensemble we analyze,

$5,121,148/(4,000 \times 1,300) = 98.5\%$ of the Cl^- ions are within 11 Å of an Arg^+ . We next enumerate putative bridging interactions involving two Arg^+ s on different Caprin1 chains and one Cl^- (Fig. 6b) by identifying three-bead configurations in which the distance of Cl^- to each of the two Arg^+ s is ≤ 11 Å (within the dominant small- r peak of $\rho(r)$ in Fig. 6a), which implies that the distance between the two Arg^+ s is ≤ 22 Å. In our ensemble, $4,519,387/(4,000 \times 1,300) = 86.9\%$ of the Cl^- counterions are identified to be in one or more of a total of 25,112,331 such putative bridging interaction configurations. This means that, on average, each Cl^- is involved in $25,112,331/4,519,387 = 5.56$ configurations, and thus are coordinating ≈ 4 Arg^+ s because there are 6 (≈ 5.56) ways of pairing 4 Arg^+ s. Fig. 6c shows the distribution of putative bridging configurations with respect to $\text{Arg}^+-\text{Arg}^+$ distance R . Spatial distributions of Cl^- in these configurations are provided in Fig. 6d,e, which are quite similar to those of isolated $\text{Arg}^+-\text{Cl}^--\text{Arg}^+$ systems for $R \lesssim 14$ Å (Fig. 6f,g). Among the putative bridging configurations, we make an energetic distinction between true bridging and neutralizing (screening) configurations. Physically, a true bridging configuration may be defined by an overall favorable (< 0) sum of (i) unfavorable Coulomb potential between two Arg^+ and (ii) the favorable Coulomb potential between the Cl^- and one of the Arg^+ s that is farther away from the Cl^- . By the same token, a neutralizing (screening) configuration may be defined by a corresponding overall unfavorable or neutral (≥ 0) sum of these two Coulomb potentials (i.e., the farther Arg^+-Cl^- distance is larger than the $\text{Arg}^+-\text{Arg}^+$ distance). In this regard, and in more general terms, Cl^- ions in bridging and neutralizing interactions may be considered, respectively, as a “strong-attraction promoter” and a “weak-attraction suppressor” of LLPS [58, 59].

In the present analysis, we group putative bridging configurations by R in bins of 2 Å (Fig. 6c). Accordingly, we may classify Cl^- positions satisfying the above condition of favorable (< 0) sum of Coulomb potentials for all R values within the 2 Å range of the bin as in true bridging configurations (79.6%), those Cl^- positions satisfying the above condition of unfavorable (≥ 0) sum of Coulomb potentials for all R values in the 2 Å range as in neutralizing configurations (7.4%), and those that satisfy neither as “intermediate” configurations (13.0%). Even with this more stringent criterion, $\approx 80\%$ of putative bridging configurations are true bridging configurations. Because on average a Cl^- counterion known to be involved in at least one putative bridging configuration is on average participating in ~ 5 –6 such configurations, the probability that it is involved in at least one true bridging configuration is very high, at $\approx 1.0 - (0.2)^5 = 99.97\%$. Thus, even without taking into consideration bridging interactions involving lysines, we may reasonably conclude that an overwhelming majority of $\approx 87\%$ of Cl^- counterions in the coarse-grained MD system considered are engaged in condensation-driving true bridging interactions coordinating pairs of Arg^+ on different Caprin1 chains. Similar extensive Cl^- and Na^+ bridging interactions are observed in a recent all-atom molecular study of LLPS of short peptides under a variety of overall salt concentrations [72].

Explicit-ion MD rationalizes [NaCl]-dependent phase properties of arginine-lysine mutants of Caprin1

We apply our MD methodology also to four RtoK Caprin1 variants, termed 15Rto15K, 4Rto4K_N, 4Rto4K_M, and 4Rto4K_C (*SI Appendix*, Fig. S1), which involve 15 or 4 RtoK

substitutions [83]. The simulated phase diagrams in Fig. 7 exhibit reentrant phase behaviors for all three 4Rto4K variants. While these results are consistent with experiments showing LLPS of these 4Rto4K variants commencing at different nonzero [NaCl]s [83], the simulated reentrant dissolution is not observed experimentally, probably because the actual [NaCl] needed is beyond the experimentally investigated or physically possible range of salt concentration. Simulated reentrant phase behaviors are also seen for 15Rto15K; but as will be explained below, its much lower simulated UCST is consistent with no experimental LLPS for this variant [83]. Since our main focus here is on general physical principles, we do not attempt to fine-tune the MD parameters for a quantitative match between simulation and experiment. Experimentally, only WT exhibits a clear trend toward reentrant dissolution of condensed droplets (with a LLPS propensity plateau at $[NaCl] \approx 1.55\text{--}2.5 M$, Fig. 3a, blue data points), whereas the LLPS of 4Rto4K_M and 4Rto4K_C commences at $[NaCl] \approx 1.3 M$, LLPS propensity then increases with $[NaCl]$ (a trend consistent with the MD-predicted increasing LLPS propensity at low [NaCl]s in Fig. 7b,c), but no sign of reentrant dissolution is seen up to the maximum $[NaCl] = 2 M$ investigated experimentally for the RtoK variants (Fig. 9B of ref. [83]). In contrast, the MD phase diagrams in Fig. 7 show a maximum LLPS propensity (highest T_{cr}) at $[NaCl] \approx 0.5 M$. This qualitative agreement with quantitative mismatch suggests that real Caprin1 LLPS is somewhat less sensitive to small monovalent ions than that stipulated by the present MD model. This question should be tackled in future studies by considering, for example, alternate pairwise amino acid interaction energies [88, 94, 96, 116–119] and their temperature dependence [4, 23].

Limitations notwithstanding, the MD-simulated trend agree largely with experiment. Predicted LLPS propensities quantified by the T_{cr} s in Fig. 7 follow the rank order of $WT > 4Rto4K_M > 4Rto4K_N \approx 4Rto4K_C > 15Rto15K$, which is essentially identical to that measured experimentally, viz., $WT > 4Rto4K_M > 4Rto4K_C > 4Rto4K_N > 15Rto15K$ (Fig. 9B of ref. [83]). In comparing theoretical and experimental LLPS, a low theoretical T_{cr} can practically mean no experimental LLPS when the theoretical T_{cr} is below the freezing temperature of the real system [18, 121]. Fig. 7a shows that even the highest T_{cr} for 15Rto15K (at model $[NaCl] = 480 mM$) is essentially at the same level as T_{cr}^0 for WT at $[NaCl] = 0$ ($T_{cr}/T_{cr}^0 \approx 1$). This MD prediction is consistent with the combined experimental observations of no LLPS for 15Rto15K up to at least $[NaCl] = 2 M$ and no LLPS for WT Caprin1 at $[NaCl] = 0$ (Fig. 9B,C of ref. [83]).

Field-theoretic simulation (FTS) is an efficient tool for studying multiple-component phase properties

We next turn to modeling of Caprin1 or pY-Caprin1 LLPS modulated by both ATP-Mg and NaCl. Because tackling such many-component LLPS systems using rG-RPA or explicit-ion MD is numerically challenging, here we adopt the complementary FTS approach [122] outlined in *Materials and Methods* for this aspect of our investigation. FTS is based on complex Langevin dynamics [123, 124], which is related to an earlier formulation for stochastic quantization [125, 126] and has been applied extensively to polymer solutions [122, 127]. Recently, FTS has provided insights into charge-sequence-dependent LLPS of IDRs [91, 97, 98, 119, 128]. The starting point of FTS is identical to that of rG-RPA. FTS invokes no RPA and is thus advantageous over rG-RPA in this regard, though it is

still limited by the lattice size used for simulation and its restricted treatment of excluded volume [98]. Here we apply the protocol detailed in refs. [97, 98].

A simple model of ATP-Mg for FTS

Going beyond the single-bead model for $(\text{ATP-Mg})^{2-}$ in our analytical rG-RPA theory (Fig. 2), we now adopt a 6-bead polymeric representation of $(\text{ATP-Mg})^{2-}$ (Fig. 8a) in which four negative and two positive charges serve to model ATP^{4-} and Mg^{2+} respectively. Modeling $(\text{ATP-Mg})^{2-}$ as a short charged polymer enables application of existing FTS formulations for multiple charge sequences to systems with IDRs and $(\text{ATP-Mg})^{2-}$. While the model in Fig. 8a does not capture structural details, its charge distribution does correspond roughly to that of the chemical structure of $(\text{ATP-Mg})^{2-}$. In developing FTS models involving IDR, $(\text{ATP-Mg})^{2-}$, and NaCl, we first assume for simplicity that $(\text{ATP-Mg})^{2-}$ does not dissociate and consider systems consisting of any given overall concentrations of IDR and $(\text{ATP-Mg})^{2-}$ wherein all positive and negative charges on the IDR and $(\text{ATP-Mg})^{2-}$ are balanced, respectively, by Cl^- and Na^+ to maintain overall electric neutrality (Fig. 8a).

Phase behaviors can be probed by FTS density correlation functions

LLPS of FTS systems can be monitored by correlation functions [98]. Here, we compute intra-species IDR self-correlation functions $G_{pp}(r)$ (Fig. 8b,c) and inter-species cross-correlation functions $G_{pq}(r)$ between the IDR and $(\text{ATP-Mg})^{2-}$ or NaCl (Fig. 8d,e) at three different overall $[(\text{ATP-Mg})^{2-}] = 10^{-4}b^{-3}, 0.03b^{-3}$, and $0.5b^{-3}$, where b may be taken as the peptide virtual bond length $\approx 3.8\text{\AA}$ (*Materials and Methods*). The correlation functions in Fig. 8b–e are normalized by overall densities ρ_p^0 of the IDR and ρ_q^0 for $(\text{ATP-Mg})^{2-}$, Na^+ or Cl^- , wherein density is the bead density for the given molecular species in units of b^{-3} . LLPS of the IDR is signaled by $G_{pp}(r)/(\rho_p^0)^2$ in Fig. 8b,c dropping below the unity baseline (dashed) at large distance r because it implies a spatial region with depleted IDR below the overall concentration, which is possible only if the IDR is above the overall concentration in at least another spatial region. In other words, $G_{pp}(r)/(\rho_p^0)^2 < 1$ for large r indicates that IDR concentration is heterogeneous and thus the system is phase separated. For small r , $G_{pp}(r)/(\rho_p^0)^2$ is generally expected to increase because IDR chain connectivity facilitates correlation among residues local along the chain. On top of this, LLPS propensity may be quantified by $G_{pp}(r)/(\rho_p^0)^2$ for small r because a higher value indicates a higher tendency for different chains to associate and thus a higher LLPS propensity [98].

FTS rationalizes [ATP-Mg]-modulated Caprin1 reentrant phase behaviors and their colocalization in the condensed phase

$[(\text{ATP-Mg})^{2-}]$ -modulated reentrance is predicted by FTS for Caprin1 but not for pY-Caprin1: When $[(\text{ATP-Mg})^{2-}]/b^{-3}$ varies from 10^{-4} to 0.03 to 0.5, small- r values of the Caprin1 $G_{pp}(r)$ in Fig. 8b initially increase then decrease, whereas the corresponding small- r values of the pY-Caprin1 $G_{pp}(r)$ in Fig. 8c decrease monotonically, consistent with rG-RPA (Fig. 2g,h,k,l) and experiment (Fig. 3). The inter-species cross-correlations in Fig. 8d,e show further that when an IDR condensed phase is present at $[(\text{ATP-Mg})^{2-}]$

$= 0.03b^{-3}$ (as indicated by large- r behaviors of $G_{pp}(r)/(\rho_p^0)^2$ in Fig. 8b,c), $(\text{ATP-Mg})^{2-}$ is colocalized with Caprin1 or pY-Caprin1 (high value of $G_{pq}/\rho_p^0\rho_q^0$ for small r) in the IDR-condensed droplet. By comparison, the variation of $[\text{Na}^+]$ and $[\text{Cl}^-]$ is much weaker. For Caprin1, Cl^- is enhanced over Na^+ in the Caprin1 condensed phase (small- r $G_{pq}/\rho_p^0\rho_q^0$ of the former larger than the latter in Fig. 8d), but the reverse is seen for pY-Caprin1 (Fig. 8e). This FTS-predicted difference, most likely arising the positive net charge on Caprin1 and the smaller negative net charge on pY-Caprin1, is consistent with the MD results in Fig. 4e–h and *SI Appendix*, Fig. S3.

FTS rationalizes experimentally observed residue-specific binding of Caprin1 with ATP-Mg

The propensities for $(\text{ATP-Mg})^{2-}$, Na^+ , and Cl^- to associate with each residue i along the Caprin1 IDR ($i = 1, 2, \dots, 103$) in FTS are quantified by the residue-specific integrated correlation $\mathcal{G}_{pq}^{(i)}/\rho_{p,i}^0\rho_q^0$ in Fig. 8f, which is the integral of the corresponding $G_{pq}^{(i)}(r)$ from $r = 0$ to a relative short cutoff distance $r = r_{\text{contact}}$ to provide a relative contact frequency for residue i and ionic species q to be in spatial proximity (*Materials and Methods* and *SI Appendix*). Notably, the residue-position-dependent integrated correlation for $(\text{ATP-Mg})^{2-}$ varies significantly, exhibiting much larger values near the N-terminal and a little before the C-terminal but weaker correlation elsewhere (Fig. 8f, red symbols). The two regions of high integrated correlation (i.e., favorable association) coincide with regions with high sequence concentration of positively charged residues. This FTS prediction is remarkably similar to the experimental NMR finding that binding between $(\text{ATP-Mg})^{2-}$ and Caprin1 occurs strongly at the arginine-rich N- and C-terminal regions, as indicated by the volume ratio V/V_0 data in Fig. 1C of ref. [84] that quantifies the ratio of peaks in NMR spectra in the presence and absence of trace amounts of ATP-Mn. For comparison with the FTS results, this set of experimental data is replotted as $1 - V/V_0$ in Fig. 8f (grey symbols, right vertical axis) to illustrate the similarity in experimental and theoretical trends because $1 - V/V_0$ is expected to trend with contact frequency. Corresponding FTS results for Na^+ and Cl^- in Fig. 8f exhibit much less residue-position-dependent variation, with Cl^- displaying only slightly enhanced association in the same arginine-rich regions, and Na^+ showing even less variation, presumably because the positive charges on Caprin1 are already essentially neutralized by the locally associated $(\text{ATP-Mg})^{2-}$ or Cl^- ions. The theory-experiment agreement in Fig. 8f regarding ATP-Caprin1 interactions indicates once again that electrostatics is an important driving force underlying many aspects of experimentally observed Caprin1– $(\text{ATP-Mg})^{2-}$ association.

FTS snapshots of [ATP-Mg]-modulated reentrant phase behaviors and Caprin1-ATP-Mg colocalization

The above FTS-predicted trends are further illustrated in Fig. 9 by field snapshots. Such FTS snapshots are generally useful for visualization and heuristic understanding [91, 98, 119], including insights into subtler aspects of spatial arrangements exemplified by recent studies of subcompartmentalization entailing either co-mixing or demixing in multiple-component LLPS that are verifiable by explicit-chain MD [98, 119]. Now, trends deduced from the correlation functions in Fig. 8 are buttressed by the representative

snapshots in Fig. 9: As the bead density of $(\text{ATP-Mg})^{2-}$ is increased from $10^{-4}b^{-3}$ to $0.03b^{-3}$ to $0.5b^{-3}$, the spatial distribution of Caprin1 evolves from an initially dispersed state to a concentrated droplet to a (reentrant) dispersed state again (Fig. 9a), whereas the initial dense pY-Caprin1 droplet becomes increasingly dispersed monotonically (Fig. 9b). Colocalization of $(\text{ATP-Mg})^{2-}$ with both the Caprin1 (Fig. 9c) and pY-Caprin1 (Fig. 9d) droplets is clearly visible at $[(\text{ATP-Mg})^{2-}] = 0.03b^{-3}$, though the degree of colocalization is appreciably higher for Caprin1 than for pY-Caprin1. This is likely because the positive net charge of Caprin1 is more attractive to $(\text{ATP-Mg})^{2-}$. By comparison, variations in Na^+ and Cl^- distribution between Caprin1/pY-Caprin1 dilute and condensed phases are not so discernible in Fig. 9e–h, consistent with the small differences in the corresponding FTS correlation functions (Fig. 8d,e).

Robustness of general trends predicted by FTS

We have also assessed the generality of the results in Figs. 8 and 9 by considering three variations in the molecular species treated by FTS: (i) Caprin1 or pY-Caprin1 with only Na^+ and Cl^- but no $(\text{ATP-Mg})^{2-}$ (*SI Appendix*, Fig. S4), (ii) Caprin1 with $(\text{ATP-Mg})^{2-}$ and either Na^+ or Cl^- (but not both) to maintain overall charge neutrality or pY-Caprin1 with $(\text{ATP-Mg})^{2-}$ and Na^+ as counterion but no Cl^- (*SI Appendix*, Fig. S5), and (iii) Caprin1 or pY-Caprin1 with ATP^{4-} , Mg^{2+} , Na^+ and Cl^- (*SI Appendix*, Fig. S6). Despite these variations in FTS models, *SI Appendix* Figs. S4–S6 consistently show reentrant behavior for Caprin1 but not pY-Caprin1 and Figs. S5 and S6 both exhibit colocalization of ATP with condensed Caprin1, suggesting that these features are robust consequences of the basic electrostatics at play in Caprin1/pY-Caprin1 + ATP-Mg + NaCl systems.

Discussion

It is reassuring that, in agreement with experiment, all of our electrostatics-based theoretical approaches consistently predict salt-dependent reentrant phase behaviors for Caprin1, whereas pY-Caprin1 LLPS propensity decreases monotonically with increasing salt (Figs. 2, 4, 8, and 9). This effect applies to small monovalent salts exemplified by Na^+ and Cl^- as well as to our electrostatics-based single- and multiple-bead models of $(\text{ATP-Mg})^{2-}$ or ATP^{4-} , with ATP exhibiting a significant colocalization with the Caprin1 condensed phase (Figs. 2g,h,k,l and 9c) attributable to the higher valency of $(\text{ATP-Mg})^{2-}$ and ATP^{4-} than that of monovalent ions. As mentioned above, the difference in salt-dependent LLPS of Caprin1 and pY-Caprin1 originates largely from the polyelectrolytic nature of Caprin1 and the polyampholytic nature of pY-Caprin1 [71] corresponding, respectively, to the “high net charge” and “screening” classes of IDPs in a more recent analysis [72].

Related studies of electrostatic effects on biomolecular condensates

Our theoretical predictions are also largely in agreement with recent computational studies on salt concentrations in the dilute versus condensed phases [120] and salt-dependent reentrant behaviors [50] of other biomolecular condensates, including explicit-water, explicit-ion atomic simulations with preformed condensates of the N-terminal RGG domain of LAF-1 [120] and of the highly positive proline-arginine 25-repeat dipeptide PR₂₅ [129].

A recent study examines salt-dependent reentrant LLPSs of full-length FUS (WT and G156E mutant), TDP-43, bromodomain-containing protein 4 (Brd4), sex-determining region Y-box 2 (Sox2), and annexin A11 [50]. Unlike the requirement of a nonzero monovalent salt concentration for Caprin1 LLPS, LLPS is observed for all these six proteins with KCl, NaCl or other salts at concentrations as low as 50 mM. Also unlike Caprin1, their protein condensates dissolve at intermediate salt then re-appear at higher salt, a phenomenon the authors rationalize by a tradeoff between decreasing favorability of cation-anion interactions and increasing favorability of cation-cation, cation- π , hydrophobic, and other interactions with increasing monovalent salt [50].

Two reasons may account for this difference. First, Caprin1 does not phase separate at low salt because it is a relatively strong polyelectrolyte ($NCPR = +13/103 = +0.126$). By comparison, five of the six proteins in ref. [50] are much weaker polyelectrolytes or not at all, with $NCPR = +14/526 = +0.0266$, $+13/526 = +0.0247$, $-7/80 = -0.0875$, 0, and $+3/326 = +0.00920$, respectively, for FUS (WT, mutant), TDP-43, Brd4, and A11. Apparently, their weak electrostatic repulsions can be overcome by favorable nonelectrostatic interactions alone to enable LLPS.

Second, compared to Caprin1, the proteins in ref. [50] are either significantly larger (WT and mutant FUS) or significantly more hydrophobic and aromatic (the other four proteins), both properties are conducive to LLPS. For instance, although Sox2's $NCPR = +14/88 = +0.159$ is higher than that of Caprin1, among Sox2's amino acid residues, $21/88 = 23.9\%$ are large hydrophobic or aromatic residues leucine (L), isoleucine (I), valine (V), methionine (M), phenylalanine (F), or tryptophan (W), and $17/88 = 19.3\%$ are large aliphatic residues L, I, V, or M. This amino acid composition suggests that hydrophobic or π -related interactions in Sox2 can be sufficient to overcome electrostatic repulsion to effectuate LLPS at zero salt. In contrast, the Caprin1 IDR contains merely one L; only $10/103 = 9.7\%$ of the residues of Caprin1 are in the L, I, V, M, F, W hydrophobic/aromatic category and only $6/103 = 5.8\%$ are in the L, I, V, M aliphatic category. The corresponding aliphatic fractions of TDP-43, Brd4 and A11, at $21/80 = 26.3\%$, $33/132 = 25\%$, and $90/326 = 27.6\%$, respectively, are also significantly higher than that of Caprin1.

Effects of salt on biomolecular LLPS

Effects of salts on LLPS, including partition of salt into polymer-rich phases, are of long-standing interest in polymer physics [130]. In the biomolecular condensate context, the versatile functional roles of salts are highlighted by the interplay between electrostatic and cation- π interactions [131, 132], salts' modulating effects on heat-induced LLPSs of RNAs [133], their regulation of condensate liquidity [134], and even their potential impact in extremely high-salt exobiological environments [135]. While some of these recent studies focus primarily on salts' electrostatic screening effects without changing the signs of the effective polymer charge-charge interaction [131], effective attractions between like charges bridged by salt or other oppositely-charged ions [104] as illustrated by Caprin1 (Fig. 5f, Fig. 6) and a recent study of A1-LCD [72] are likely needed to account for phenomena such as salt-induced dimerization of highly charged, medically relevant arginine-rich cell-penetrating short peptides [136, 137].

Tielines in protein-salt phase diagrams

In view of Caprin1's polyelectrolytic nature, the mildly negative tieline slopes in Fig. 2a,b are consistent with rG-RPA predictions for a fully charged polyelectrolyte (Fig. 10a of ref. [71]). This depletion of monovalent salt in the condensed phase is similar to that observed in the complex coacervation of oppositely charged polyelectrolytes [138–140]. By comparison, the positive rG-RPA tieline slopes for polyampholytic pY-Caprin1 (Fig. 2c,d), confirmed by MD in Fig. 4f,h, are appreciably steeper than that predicted for fully charged (± 1) diblock polyampholytes by rG-RPA and the essentially flat tielines predicted by FTS (Fig. 10b of ref. [71] and Fig. 7 of ref. [92]). Whether this difference originates from the presence of divalent charged (-2) phosphorylated sites in pY-Caprin1 remains to be elucidated. In any event, tieline analysis is generally instrumental for revealing details, such as stoichiometry, of the interactions driving multiple-component biomolecular LLPSs [11, 141], rG-RPA should be broadly useful as a computationally efficient tool for this purpose [71].

Counterion valency

Our rG-RPA prediction that the maximum condensed-phase [Caprin1] at low $[\text{Na}^+]$ is substantially higher with divalent than with monovalent counterions is in line with early findings that higher-valency counterions are more effective in bridging polyelectrolyte interactions to favor LLPS [142] and recent observations that salt ions with higher valencies enhance biomolecular LLPS [143, 144]. The possibility that this counterion/salt effect on LLPS may be exploited more generally for biological functions and/or biomedical applications remains to be further explored. In this regard, while recognizing that ATP can engage in π -related interactions [65–67], our electrostatics-based perspective of ATP-dependent reentrant phase behaviors is consistent with recent observations on polylysine LLPS modulated by enzymatically catalyzed ATP turnovers [140, 145].

Prospective extensions of the present theoretical methodology

Beyond the above comparisons, further experimental testing of other aspects of our theoretical predictions should be pursued, especially those pertaining to pY-Caprin1. Future theoretical efforts should address a broader range of scenarios by independent variations of $[\text{ATP}^{4-}]$, $[\text{Mg}^{2+}]$, $[\text{Na}^+]$, $[\text{Cl}^-]$ and to account for nonelectrostatic aspects of ATP-Mg dissociation [146] with predictions such as tieline slopes analyzed in detail to delineate effects of configurational entropy of salt ions [147] and solvent quality [148]. In addition to our basic modeling constructs, the impact of excluded volume and solvent/cosolute-mediated temperature-dependent effective interactions should be incorporated. Excluded volume is known to affect LLPS [92], demixing of IDP species in condensates [98], and partition of salt ions in polymer LLPS [139]. Moreover, LCST can be driven not only by hydrophobicity [4, 7, 23] but also by electrostatics, as suggested by experiment on complex coacervates of oppositely charged polyelectrolytes [149]. Bringing together these features into a comprehensive formulation will afford a more accurate physical picture.

Summary

To recapitulate, we have employed three complementary theoretical and computational

approaches to account for the interplay between sequence pattern, phosphorylation, counterion, and salt in the phase behaviors of IDPs. Application to the Caprin1 IDR and its phosphorylated variant pY-Caprin1 provides physical rationalization for a variety of trends observed in experiments, including reentrance behaviors and very substantial ATP colocalization. These findings support a significant—albeit not exclusive—role of electrostatics in these biophysical phenomena, providing physical insights into effects of sequence-specific charge-charge interactions on ATP-modulated physiological functions of biomolecular condensates such as regulation of ion concentrations. The approach developed here should be of general utility as a computationally efficient tool for hypothesis generation, design of new experiments, exploration and testing of biophysical scenarios, as well as a starting point for more sophisticated theoretical/computational modeling.

Materials and Methods

Further details of the experimental and theoretical/computational methodologies outlined below are provided in *SI Appendix*.

Experimental sample preparation

The low complexity 607–709 domain of Caprin1 was expressed and purified as before [33, 84]. WT Caprin1 was used in all experiments except those on [NaCl] dependence reported in Table 1 and Fig. 3a, for which a double mutant was used because residue pairs N623-G624 and N630-G631 in WT Caprin1 form isoaspartate (IsoAsp) glycine linkages over time which alters the charge distribution of the IDR [83].

Phosphorylation of the Caprin1 IDR

Phosphorylation of the WT Caprin1 IDR was performed as described in our prior study [33] by using the kinase domain of mouse Eph4A (587-896) [150] with an N-terminal His-SUMO tag.

Determination of phase diagrams

We established phase diagrams for Caprin1 and pY-Caprin1 by measuring the protein concentrations in dilute and condensed phases across a range of [NaCl]s (Fig. 1c,d). Initially homogenizing the two phases of the demixed samples into a milky dispersion through vortexing, $\sim 200 \mu\text{L}$ aliquots were then incubated in a PCR thermocycler with a heated lid at 90°C, in triplicate, for a minimum of one hour. During incubation, the condensed phase settled and formed a clear phase at the bottom. For concentration measurements, the samples were diluted in 6 M GdmCl and 20 mM NaPi (pH 6.5). The dilute phase (top layer) was analyzed through a tenfold dilution of 10 μL samples, and the condensed phase (bottom layer) was analyzed through 250- to 500-fold dilution of 2 or 10 μL samples.

Concentrations of salt and ATP-Mg in dilute and condensed phases

Inductively coupled plasma optical emission spectroscopy (ICP-OES) measurements of $[\text{Na}^+]$ were performed using a Thermo Scientific iCAP Pro ICP-OES instrument in axial mode. ICP-OES was also used to determine [ATP] and $[\text{Mg}^{2+}]$ (Table 2). The detection

of phosphorus and magnesium served as proxies for quantifying ATP and Mg^{2+} levels, respectively. Standard curves were prepared using solutions with known [ATP] and $[Mg^{2+}]$, ranging from 0 to 90 ppm for ATP and 0 to 25 ppm for Mg^{2+} .

Caprin1 phase separation propensity at high salt concentrations

A 6 mM solution of double-mutant Caprin1 IDR (see above) in buffer (25 mM sodium phosphate, pH 7.4) was prepared by exchanging (3 times) the purified protein after size exclusion chromatography using centrifugal concentrators (3 kDa, EMD Millipore). Caprin samples for turbidity measurements were prepared by taking 0.5 μ L of the above solution and diluting it into buffer (25 mM sodium phosphate, pH 7.4) containing varying $[NaCl]$ s ranging from 0 to 4.63 M, in a sample volume of 9 μ L, so as to achieve [Caprin1] of 300 μ M. After rigorous mixing, 5 μ L samples were loaded into a μ Cuvette G1.0 (Eppendorf). OD600 measurements (Fig. 3a) were recorded three times using a BioPhotometer D30 (Eppendorf).

[ATP-Mg]-dependent Caprin1 phase behaviors

Turbidity assays were conducted using the method we described previously [83].

Sequence-specific theory of heteropolymer phase separation

As detailed in refs. [97, 119], an example of the sequence-specific polymer theories [18, 71] is that for a solution with a single species of charged heteropolymers in n_p copies, n_c counterions (same type), and n_s salt ions (same type, but different from the counterions). Each polymer chain has N monomers (residues) with charge sequence $|\sigma\rangle = [\sigma_1, \sigma_2, \dots, \sigma_N]^T$ in vector notation, where $\sigma_i \in \{0, \pm 1, -2\}$ is the charge of the i th residue. The counterions and salt ions are monomers carrying z_c and z_s charges, respectively. The particle-based partition function is given by

$$\mathcal{Z} = \frac{1}{n_p! n_c! n_s! n_w!} \int \prod_{\alpha=1}^{n_p} \prod_{i=1}^N d\mathbf{R}_{\alpha,i} \prod_{a=1}^{n_s+n_c} d\mathbf{r}_a e^{-\mathcal{T}[\mathbf{R}] - \mathcal{U}[\mathbf{R}, \mathbf{r}]}, \quad (2)$$

where n_w denotes the number of water (solvent) molecules, $\mathbf{R}_{\alpha,i}$ is the position vector of the i th residue of the α th polymer, \mathbf{r}_a is the position vector of the a th small ion. \mathcal{T} accounts for polymer chain connectivity modeled by a Gaussian elasticity potential with Kuhn length l . \mathcal{U} describes the interactions among all molecular components of the system, here consisting only of Coulomb electrostatics (el) and excluded-volume (ex) for simplicity, viz., $\mathcal{U} = \mathcal{U}_{el} + \mathcal{U}_{ex}$. Their interaction strengths are governed by the Bjerrum length l_B and the two-body excluded volume parameter v_2 . By introducing conjugate fields $\psi(\mathbf{r})$, $w(\mathbf{r})$ and applying the Hubbard-Stratonovich transformation, the system defined by the particle-based partition function in Eq. (2) is recast as a field theory of ψ, w in which their interactions with polymer, salt, and counterion are described, respectively, by single-molecule partition functions \mathcal{Q}_p , \mathcal{Q}_s , and \mathcal{Q}_c . For instance,

$$\mathcal{Q}_p[\psi, w] = \int \prod_{i=1}^N d\mathbf{R}_i \exp \left(-\mathcal{H}_p[\mathbf{R}; \psi, w] \right) \quad (3)$$

where \mathcal{H}_p is the single-polymer Hamiltonian and the chain label α is dropped.

Renormalized-Gaussian random-phase-approximation (rG-RPA)

Following refs. [43, 71], \mathcal{H}_p can be separated into a Gaussian-chain Hamiltonian with an effective (renormalized) Kuhn length $l_1 = xl$ and a remaining term, $\mathcal{H}_p = \mathcal{H}_p^0 + \mathcal{H}_p^1$, where

$$\mathcal{H}_p^0 = \frac{3}{2l^2x} \sum_{i=1}^{N-1} (\mathbf{R}_{i+1} - \mathbf{R}_i)^2 , \quad (4a)$$

$$\mathcal{H}_p^1 = \frac{3}{2l^2} \left(1 - \frac{1}{x} \right) \sum_{i=1}^{N-1} (\mathbf{R}_{i+1} - \mathbf{R}_i)^2 - i \sum_{i=1}^N [\sigma_i \psi(\mathbf{R}_i) + w(\mathbf{R}_i)] , \quad (4b)$$

with $i^2 = -1$. By requiring the observable polymer square end-to-end distance be properly quantified by \mathcal{H}_p^0 , x can be approximated by variational theory [43]. RPA can then be applied to the renormalized Gaussian (rG) chain system with $l \rightarrow xl$ and a corresponding scaling of the contour length to arrive at an improved theory, rG-RPA, for sequence-specific LLPS.

Explicit-ion coarse-grained molecular dynamics (MD)

The MD model in this work augments a class of implicit-water coarse-grained models [88, 94] that utilize a “slab” approach for efficient equilibration [114] by incorporating explicit small ions. As before [94], the total MD potential energy U_T is the sum of long-spatial-range electrostatic (el) and short-spatial-range (sr) interactions of the Lennard-Jones (LJ) type as well as bond interactions, i.e., $U_T = U_{el} + U_{sr} + U_{bond}$. With small ions, the electrostatic component is given by a sum of polymer-polymer (pp), polymer-ion (pi), and ion-ion (ii) contributions: $U_{el} = U_{el,pp} + U_{el,pi} + U_{el,ii}$. Details of these terms are provided in *SI Appendix*.

Field-theoretic simulation (FTS)

FTS is useful for sequence-specific multiple-component LLPSs encountered in biomolecular settings. The new applications developed here are based on recent advances (see, e.g., refs. [91, 92, 97, 98, 122, 127]). Consider the field theoretic Hamiltonian

$$H[w, \psi] = \int d\mathbf{r} \left(\frac{[\nabla \psi(\mathbf{r})]^2}{8\pi l_B} + \frac{w(\mathbf{r})^2}{2v_2} \right) - \sum_m n_m \ln \mathcal{Q}_m[\check{w}, \check{\psi}] , \quad (5)$$

where \mathcal{Q}_m is single-molecule partition function [here m labels the components in the system, cf. Eq. (3)] and the breves denote convolution with Γ , i.e., for a generic field ϕ , $\check{\phi}(\mathbf{r}) = \Gamma \star \phi(\mathbf{r}) \equiv \int d\mathbf{r}' \Gamma(\mathbf{r} - \mathbf{r}') \phi(\mathbf{r}')$; here $\phi = w, \psi$, and Γ is a Gaussian smearing function [97]. FTS utilizes the Complex-Langevin (CL) method [123, 124] by introducing an artificial CL time variable (t), viz., $w(\mathbf{r}) \rightarrow w(\mathbf{r}, t)$, $\psi(\mathbf{r}) \rightarrow \psi(\mathbf{r}, t)$ and letting the system evolve in CL time in accordance with a collection of Langevin equations

$$\frac{\partial \phi(\mathbf{r}, t)}{\partial t} = -\frac{\delta H}{\delta \phi(\mathbf{r}, t)} + \eta_\phi(\mathbf{r}, t), \quad \phi = w, \psi , \quad (6)$$

where the Gaussian noise $\eta_\phi(\mathbf{r}, t)$ satisfies $\langle \eta_\phi(\mathbf{r}, t) \eta_{\phi'}(\mathbf{r}', t') \rangle = 2\delta_{\phi,\phi'}\delta(\mathbf{r} - \mathbf{r}')\delta(t - t')$. Thermal averages of thermodynamic observables are then computed as asymptotic CL time averages of the corresponding field operators. Spatial information about condensation and proximity of various components is readily gleaned from density-density correlation functions [97, 98],

$$G_{m,n}(|\mathbf{r} - \mathbf{r}'|) = \langle \hat{\rho}_m(\mathbf{r}) \hat{\rho}_n(\mathbf{r}') \rangle, \quad (7)$$

where m, n are labels for the components in the model system. For instance, m may represent all polymer beads (denoted “p”) irrespective of the sequence positions of the beads [$\hat{\rho}_p(\mathbf{r}) = \sum_{i=1}^{n_p} \sum_{\alpha=1}^N \Gamma(\mathbf{r} - \mathbf{R}_{\alpha,i})$], and n may represent all six beads in our ATP-Mg model (Fig. 8a). One may also define

$$G_{pq}^{(i)}(|\mathbf{r} - \mathbf{r}'|) \equiv \langle \hat{\rho}_{p,i}(\mathbf{r}) \hat{\rho}_q(\mathbf{r}') \rangle, \quad (8)$$

where (i) represents the i th residue along a protein chain [$\hat{\rho}_{p,i}(\mathbf{r}) \equiv \sum_{\alpha=1}^N \Gamma(\mathbf{r} - \mathbf{R}_{\alpha,i})$ is the density of the i th residue among all the protein chains], and $q = (\text{ATP-Mg})^{2-}$, Na^+ , or Cl^- . With this definition, residue-specific relative contact frequencies are estimated by integrating Eq. (8) over a spherical volume within a small inter-component distance r_{contact} :

$$\mathcal{G}_{pq}^{(i)} \equiv 4\pi \int_0^{r_{\text{contact}}} dr r^2 G_{pq}^{(i)}(r). \quad (9)$$

For the normalized $\mathcal{G}_{pq}^{(i)} / \rho_{p,i}^0 \rho_q^0$ plotted in Fig. 8f, $\rho_{p,i}^0$ and ρ_q^0 are bulk (overall) densities, respectively, of the i th protein residue and of $(\text{ATP-Mg})^{2-}$ or small ions, and $r_{\text{contact}} \approx 1.5b$ is used to characterize contacts. Further details are provided in *SI Appendix*.

Acknowledgements

This work was supported by Canadian Institutes of Health Research (CIHR) grant NJT-155930 and Natural Sciences and Engineering Research Council of Canada (NSERC) grant RGPIN-2018-04351 to H.S.C., CIHR grant FDN-148375, NSERC grant RGPIN-2016-06718, and Canada Research Chairs Program to J.D.F.-K. as well as CIHR grant FDN-503573 to L.E.K. A.K.R. was supported by a CIHR postdoctoral fellowship. We are grateful for the computational resources provided generously by Compute/Calcul Canada and the Digital Research Alliance of Canada.

Table 1. Sodium ions are depleted in the Caprin1-condensed phase relative to the Caprin1-dilute phase. Consistent with theory, $[Na^+]$ is consistently lower in the Caprin1-condensed phase for two temperatures at which the measurements were performed.

Bulk $[Na^+]$ (mM)	T (°C)	Caprin1-Dilute $[Na^+]$ (mM)	Caprin1-Condensed $[Na^+]$ (mM)
300	25	341.3 ± 45.5	140.7 ± 6.0
300	35	289.5 ± 21.9	149.0 ± 2.5

uncertainty (\pm) is standard deviation of triplicate measurements.

Table 2. Colocalization of ATP-Mg in the Caprin1-condensed phase. For three overall ATP-Mg concentrations at room temperature, the concentrations of ATP^{4-} and Mg^{2+} are all significantly higher in the Caprin1-condensed than in the Caprin1-dilute phase.

[ATP-Mg] (mM)	Caprin1-Dilute			Caprin1-Condensed		
	[Caprin1] (μ M)	$[Mg^{2+}]$ (mM)	$[ATP^{4-}]$ (mM)	[Caprin1] (mM)	$[Mg^{2+}]$ (mM)	$[ATP^{4-}]$ (mM)
3	67.7 ± 5.0	2.85 ± 0.05	2.76 ± 0.07	29.9 ± 3.8	70.7 ± 6.0	143 ± 30
10	26.4 ± 1.2	8.57 ± 0.14	8.53 ± 0.97	35.3 ± 3.5	137 ± 12	197 ± 11
30	117 ± 3	28.2 ± 0.3	27.6 ± 0.8	28.0 ± 2.0	134 ± 7	174 ± 22

Figures (Main Text)

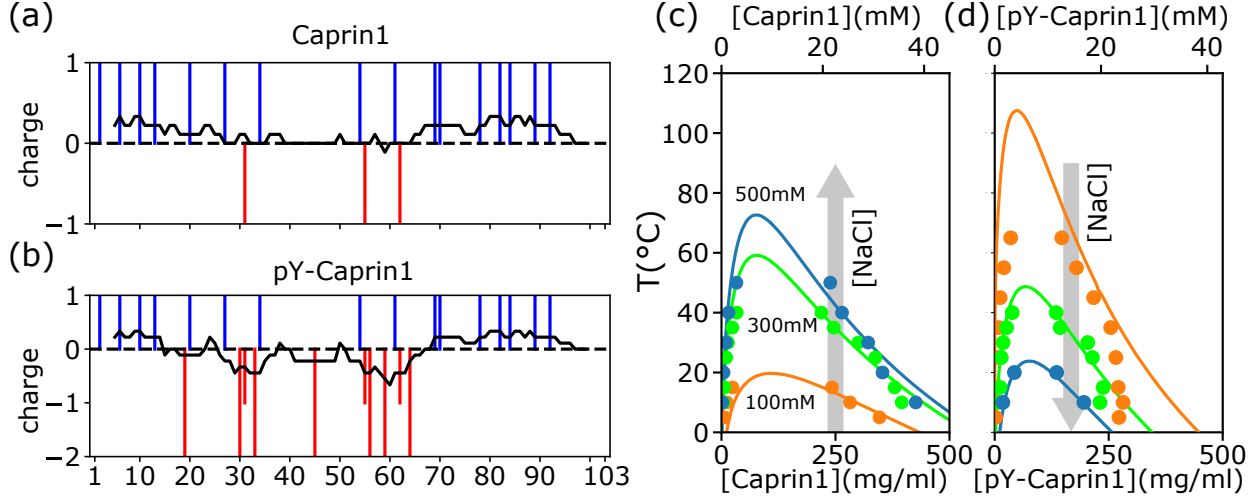


Figure 1: rG-RPA+FH theory predictions rationalize different salt dependence of Caprin1 and pY-Caprin1 LLPS. (a,b) Vertical lines indicate the sequence positions (horizontal variable) of positively charged residues (blue) and negatively charged residues or phosphorylated tyrosines (red) for (a) Caprin1 and (b) pY-Caprin1. (c,d) rG-RPA+FH coexistence curves (phase diagrams, continuous curves color-coded for the NaCl concentrations indicated) agree reasonably well with experiment (dots, same color code). The grey arrows in (c,d) highlight that when [NaCl] increases, LLPS propensity increases for (c) Caprin1 but decreases for (d) pY-Caprin1. As described in our prior RPA+FH and rG-RPA+FH formulations [18, 71], the theoretical coexistence curves shown in (c,d) are determined by fitting an effective relative permittivity ϵ_r as well as the enthalpic and entropic parts of a FH parameter $\chi(T) = \epsilon_h/T^* + \epsilon_s$ to experimental data. For the present Caprin1 and pY-Caprin1 systems, the fitted $\epsilon_r = 80.5$, which is remarkably close to that of bulk water ($\epsilon_r \approx 78.5$). The fitted (ϵ_h, ϵ_s) is $(1.0, 0.0)$ for Caprin1 and $(1.0, -1.5)$ for pY-Caprin1. These fitted energetic parameters are equivalent [18] to $\Delta H \approx -1.1 \text{ kcal mol}^{-1}$ and $\Delta S = 0.0$ for forming a residue-residue contact in the Caprin1 system (c) (i.e., it is enthalpically favorable), and $\Delta H \approx -1.1 \text{ kcal mol}^{-1}$ and $\Delta S \approx -3.0 \text{ cal mol}^{-1} \text{ K}^{-1}$ for forming a residue-residue contact in the pY-Caprin1 system (d) (i.e., it is enthalpically favorable and entropically unfavorable).

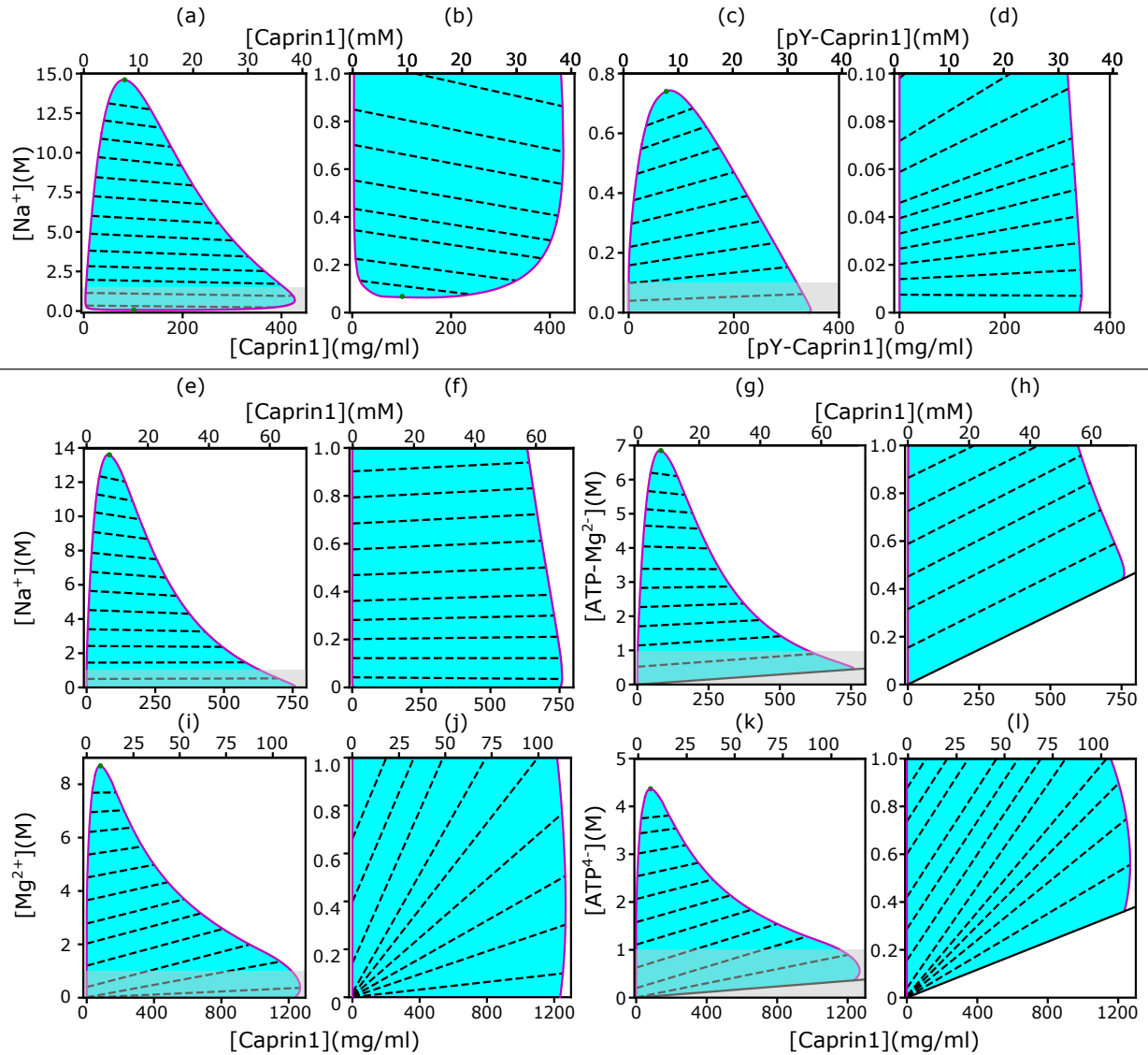


Figure 2: rG-RPA+FH theory rationalizes $[\text{NaCl}]$ -modulated reentrant phase behavior of Caprin1. In each salt-protein phase diagram ($T = 300 \text{ K}$), tielines (dashed) connect coexisting phases on the boundary (magenta curve) of the cyan-shaded coexistence region. For clarity, zoomed-in views of the grey-shaded part in (a, c, e, g, i, k) are provided by the plots to the right, i.e., (b, d, f, h, j, l), respectively. The solid inclined lines in (g, h, k, l) mark the minimum counterion concentrations required for overall electric neutrality. Results are shown for monovalent cation and anion with Caprin1 (a, b) or pY-Caprin1 (c, d); or monovalent cation and divalent anion with Caprin1 (e–h); or divalent cation and tetravalent anion with Caprin1 (i–l). Cation-modulated reentrant phase behaviors is seen for a wide concentration range for Caprin1 in (a, b) but only a very narrow range of high Caprin1 concentrations in (e, f, i, j). The (ϵ_h, ϵ_s) values for computing the phase diagrams here for Caprin1 and pY-Caprin1, respectively, are the same as those used for Fig. 1c and Fig. 1d.

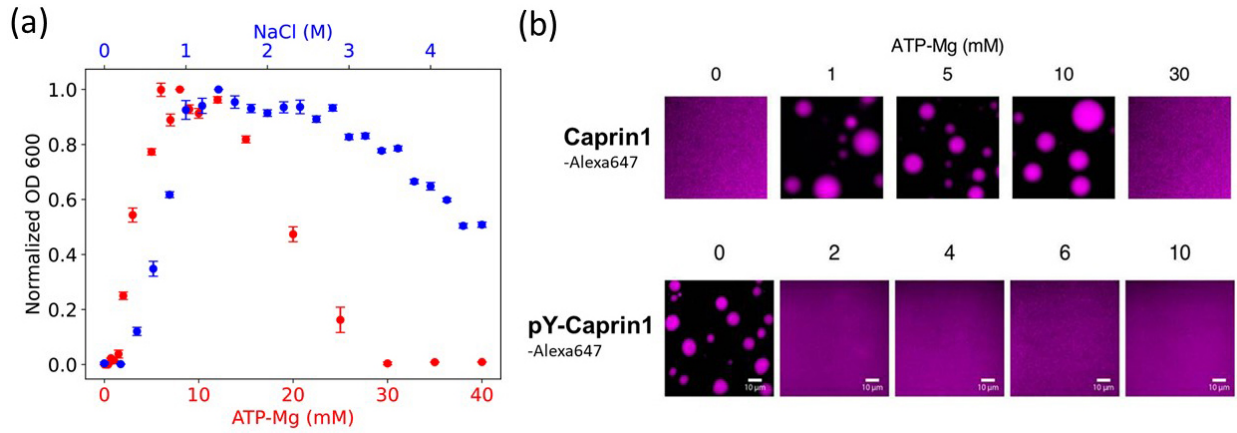


Figure 3: Experimental demonstration of [ATP-Mg]- and [NaCl]-modulated reentrant phase behavior for Caprin1. (a) Turbidity quantified by optical density at 600 nm (OD600, normalized by peak value) to assess Caprin1 LLPS propensity at [Caprin1] = 200 μ M [for ATP-Mg dependence (red), bottom scale] or [Caprin1] = 300 μ M [for NaCl dependence (blue), top scale], measured at room temperature ($\sim 23^\circ\text{C}$). Error bars are one standard deviations of triplicate measurements, which in most cases was smaller than the plotting symbols. The ATP-Mg dependence seen here for 200 μ M Caprin1 is similar to the results for 400 μ M Caprin1 (Fig. 6C of ref. [84]). (b) Microscopic images of Caprin1 and pY-Caprin1 at varying [ATP-Mg] at room temperature, showing reentrant behavior for Caprin1 but not for pY-Caprin1. Each sample contains 200 μ M of either Caprin1 or pY-Caprin1, with 1% of either Caprin1-Cy5 or pY-Caprin1-Cy5 (labeled with Cyanine 5 fluorescent dye) added for visualization, in a 25 mM HEPES buffer at pH 7.4. Scale bars represent 10 μ m.

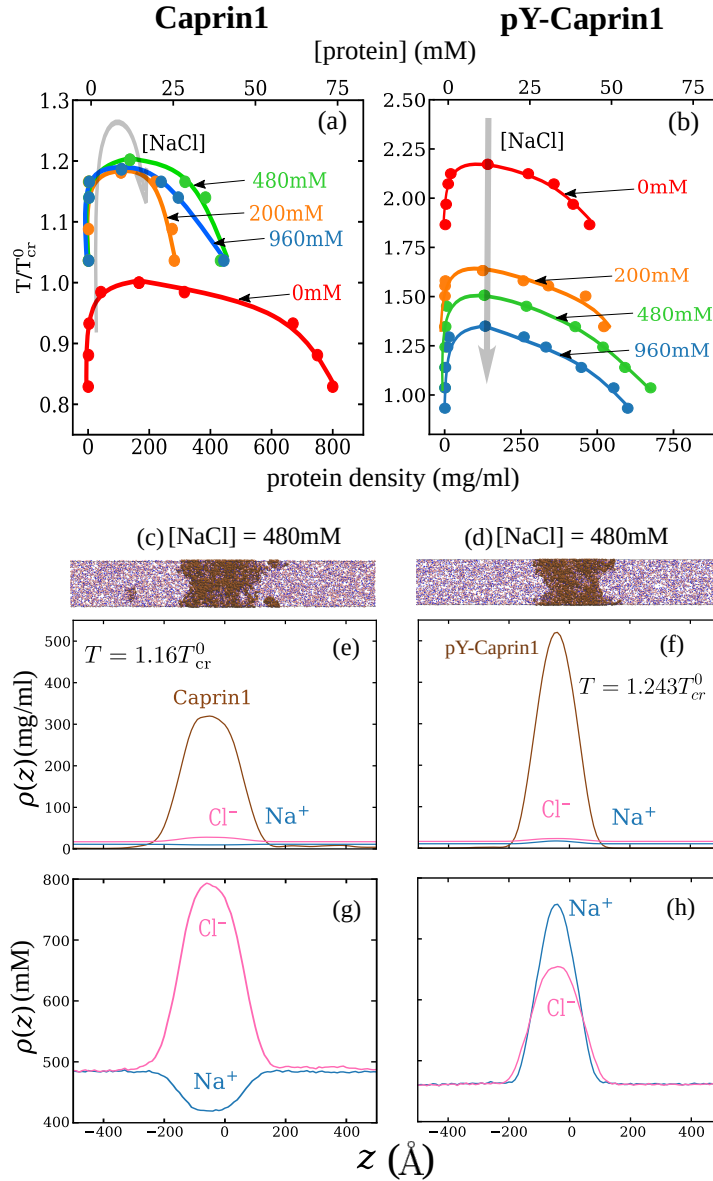


Figure 4: Explicit-ion coarse-grained MD rationalizes [NaCl]-modulated reentrant behavior for Caprin1 and lack thereof for pY-Caprin1. (a) Simulated phase diagrams (binodal curves) of Caprin1 at different temperatures plotted in units of T_{cr}^0 (see text). Symbols are simulated data points. Continuous curves are guides for the eye. Grey arrow indicates variation in [NaCl]. (b) Same as (a) but for pY-Caprin1. (c) A snapshot showing phase equilibrium between dilute and condensed phases of Caprin1 (brown chains) immersed in Na^+ (blue) and Cl^- (red) ions simulated at $[\text{NaCl}] = 480$ mM. (d) A similar snapshot for pY-Caprin1. (e, f) Mass density profiles, $\rho(z)$ (in units of mg/ml), of Na^+ , Cl^- , and (e) Caprin1 or (f) pY-Caprin1 along the elongated dimension z of the simulation box showing variations of Na^+ and Cl^- concentrations between the protein-dilute phase (low ρ for protein) and protein-condensed phase (high ρ for protein) at the simulation temperatures indicated. (g, h) Corresponding zoomed-in concentration profiles $\rho(z)$ in units of mM for Na^+ and Cl^- . Additional mass density profiles for $[\text{NaCl}] = 200$ mM and 400 mM are provided in Fig. S3.

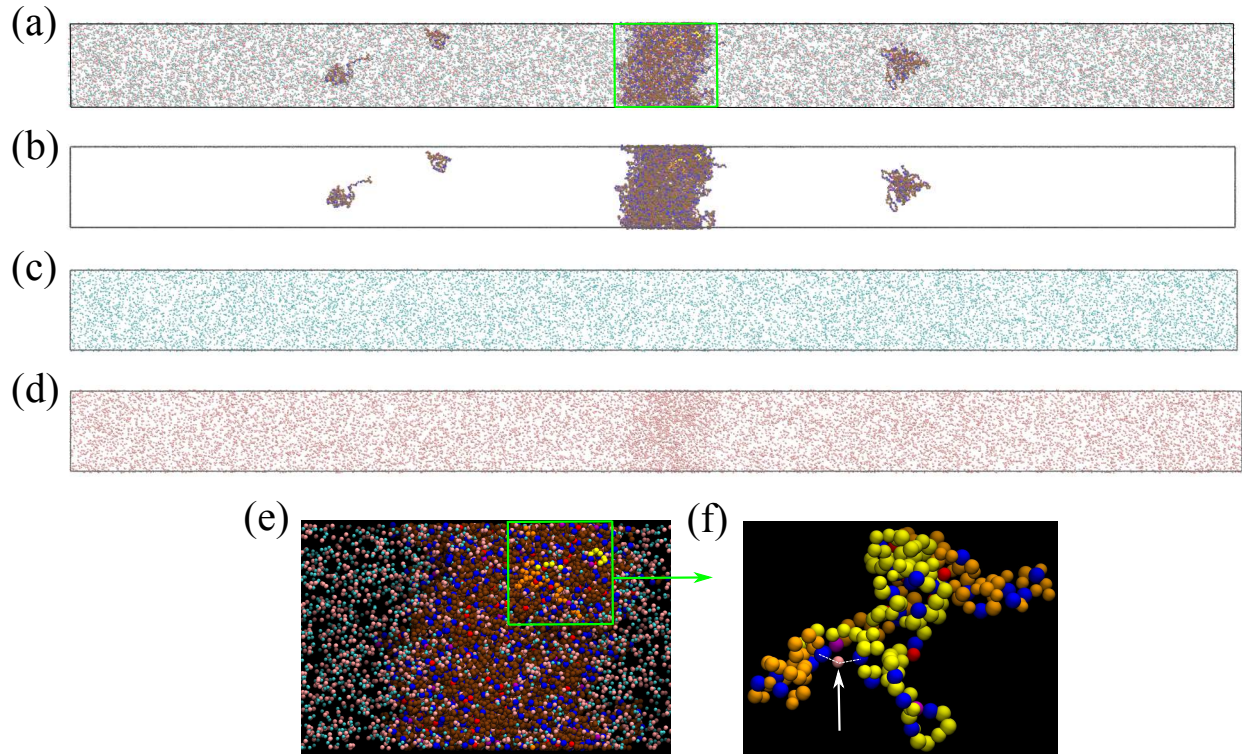


Figure 5: Counterions can stabilize Caprin1 condensed phase by favorable bridging interactions. (a) Snapshot from explicit-ion coarse-grained MD under LLPS conditions for Caprin1, showing the spatial distributions of Caprin1, Na⁺, and Cl⁻ (as in Fig. 4c). The three components of the same snapshot are also shown separately in (b) Caprin1, (c) Na⁺, and (d) Cl⁻. (e) A zoomed-in view of the condensed droplet [corresponding to the green box in (a)], now with a black background and a different color scheme. (f) A further zoomed-in view of the part enclosed by the green box in (e) focusing on two interacting Caprin1 chains. A Cl⁻ ion (pink bead indicated by the arrow) is seen interacting favorably with two arginines residues (blue beads) on the two Caprin1 chains (whose uncharged residues are colored differently by yellow or orange, lysine and aspartic acids in both chains are depicted, respectively, in magenta and red).

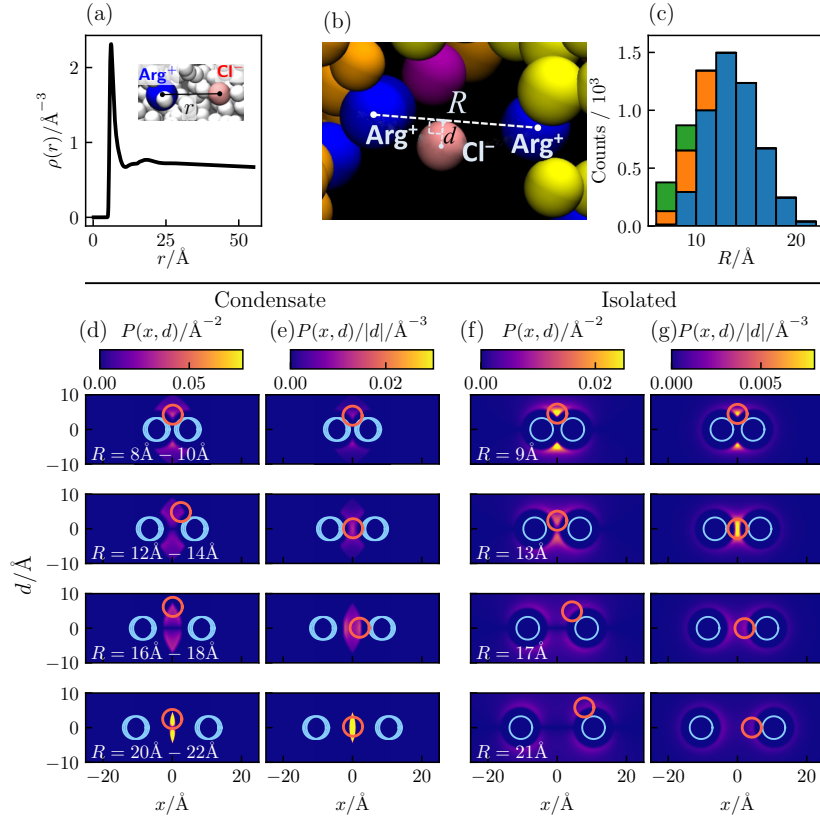


Figure 6: Counterion interactions in polyelectrolytic Caprin1. Shown distributions are averaged from 4,000 equilibrated coarse-grained MD snapshots of 100 Caprin1 chains and 1,300 Cl⁻ counterions under phase-separation conditions ($T/T_{\text{cr}}^0 = 160/193 = 0.829$) in a $115 \times 115 \times 1610 \text{ \AA}^3$ simulation box in which essentially all Caprin1 chains are in a condensed droplet. (a) Radial distribution function of Cl⁻ around a positively charged arginine residue (Arg⁺). (b) A zoomed-in view of Fig. 5f showcasing a putative bridging configuration with a Cl⁻ interacting favorably with a pair of Arg⁺s on two different Caprin1 chains. Configurational geometry is characterized by Arg⁺-Arg⁺ distance R and the distance d of the Cl⁻ from the line connecting the two Arg⁺s. (c) Distribution of putative bridging interaction configurations with respect to R . Numbers of true bridging, neutralizing, and intermediate are, respectively, in blue, green and orange. (d, e) Heat maps of two-dimensional projections of spatial distributions of Cl⁻ around two Arg⁺s satisfying the putative bridging interaction conditions among the MD snapshots. (f, g) Corresponding projected distributions of isolated Arg⁺-Cl⁻-Arg⁺ Boltzmann-averaged systems at model temperature T . Here, $P(x, d)$ is the total density of Cl⁻ on a circle of radius $|d|$ perpendicular to the heat map at horizontal position x (d, f); thus the average Cl⁻ density at a given point (x, d) is $P(x, d)/2\pi|d|$, the patterns of which are exhibited by $P(x, d)/|d|$ heat maps in (e, g). $P(x, d)$ is symmetric with respect to $d \leftrightarrow -d$ by construction, i.e., $P(x, d) = P(x, -d)$. In each heat map, the size and (ranges of) positions of model Arg⁺s are indicated by blue circles; the size and the position or one of two positions (at $\pm d$) of maximum Cl⁻ density is indicated by a magenta circle. The MD-simulated distributions of the condensed system (d, e) are quite similar to the theory-computed isolated system (f, g) for $R \lesssim 14 \text{ \AA}$, indicating that individual bridging interactions in the crowded Caprin1 condensates may be understood approximately by the electrostatics of an isolated, three-bead Arg⁺-Cl⁻-Arg⁺ system. For larger R , the heat maps in (f, g) and (d, e) are not as similar because some of the configurations in the isolated system (f, g) are precluded by the requirement that Arg⁺-Cl⁻ distance $< 11 \text{ \AA}$ for putative bridging interactions in (d, e).

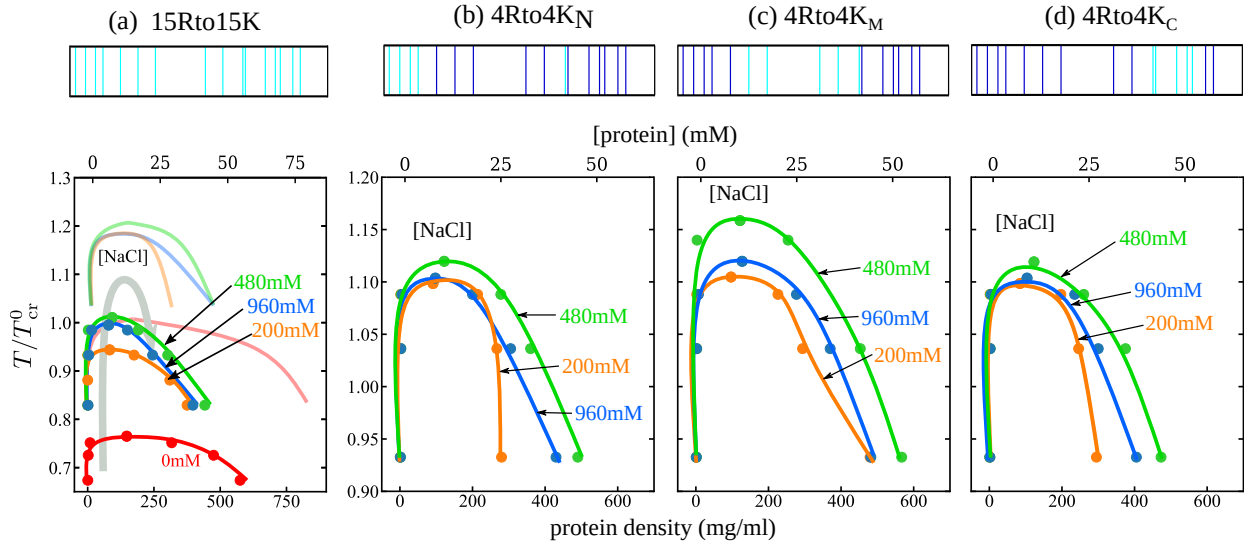


Figure 7: Explicit-ion coarse-grained MD rationalizes [NaCl]-modulated phase behavior for RtoK variants of Caprin1. Four variants studied experimentally [83] are simulated: (a) 15Rto15K, in which 15 R's in the WT Caprin1 IDR are substituted by K, (b) 4RtoK_N, (c) 4RtoK_M, and (d) 4RtoK_C, in which 4 R's are substituted by K in the (b) N-terminal, (c) middle, and (d) C-terminal regions, respectively. Top panels show positions of the R (dark blue) and K (cyan) along the Caprin1 IDR sequence. Lower panels are phase diagrams in the same style as Fig. 4. The phase diagrams for WT Caprin1 from Fig. 4a are included as continuous curves with no data points in (a) for comparison.

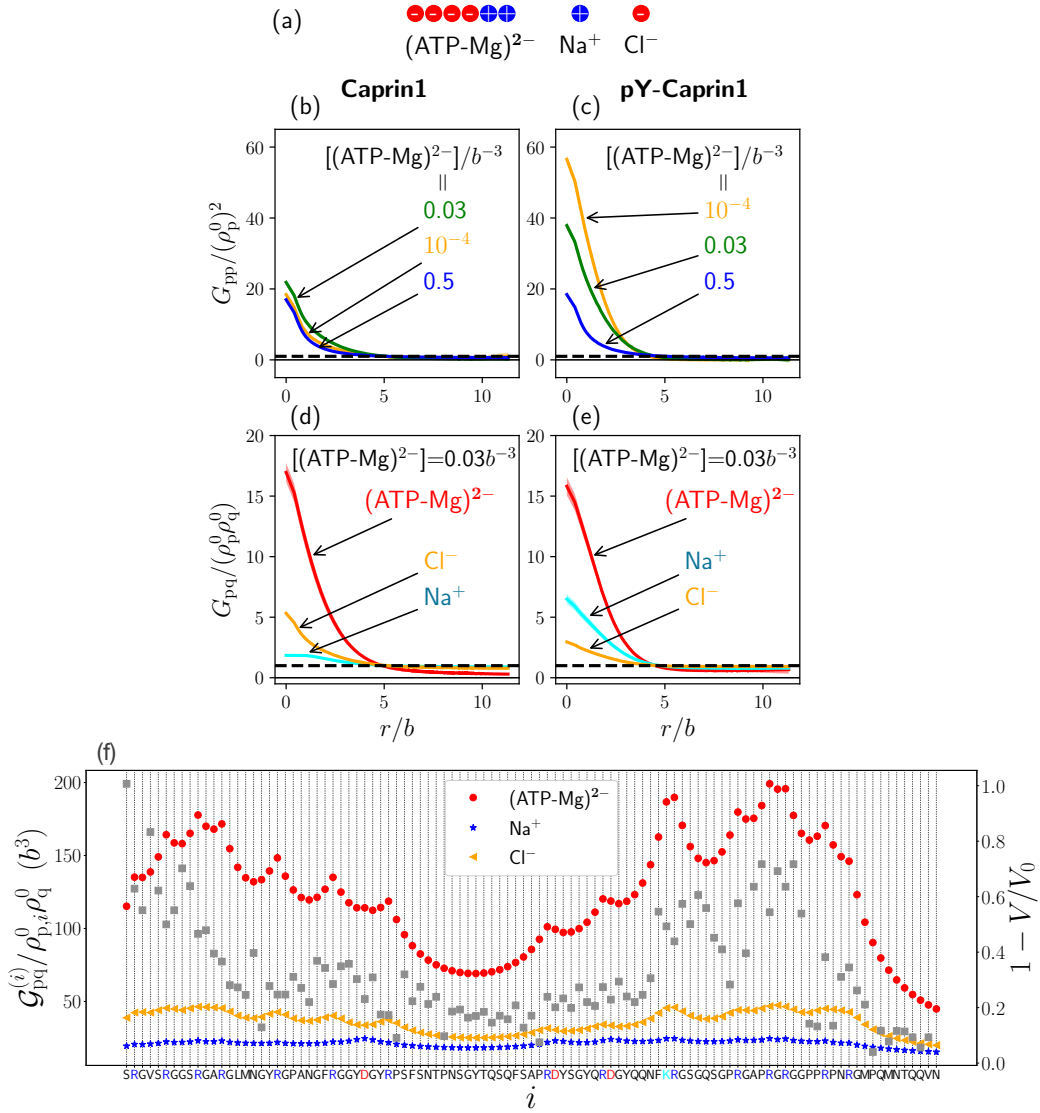


Figure 8: FTS rationalizes experimental observation of Caprin1-ATP interactions. (a) The 6-bead model for $(\text{ATP-Mg})^{2-}$ and the single-bead models for monovalent salt ions used in the present FTS. (b–e) Normalized protein-protein correlation functions at three $[(\text{ATP-Mg})^{2-}]/b^{-3}$ values (b, c) and protein-ion correlation functions [Eq. (7)] at $[(\text{ATP-Mg})^{2-}]/b^{-3} = 0.03$ (d, e) for Caprin1 (b, d) and pY-Caprin1 (c, e), computed for Bjerrum length $l_B = 7b$. Horizontal dashed lines are unity baselines (see text). (f) Values of position-specific integrated correlation $\mathcal{G}_{pq}^{(i)}/\rho_{p,i}^0 \rho_q^0$ (left vertical axis) correspond to the relative contact frequencies between individual residues (i) along the Caprin1 IDR sequence with $q = (\text{ATP-Mg})^{2-}$, Na^+ , or Cl^- under the same conditions as (d) [Eq. (S45)] (color symbols). Included for comparison are experimental NMR volume ratios V/V_0 data on site-specific Caprin1-ATP association [84]. V/V_0 decreases with increased contact probability, although a precise relationship is yet to be determined. Thus, the plotted $1 - V/V_0$ (grey data points, right vertical scale) is expected to correlate with contact frequency.

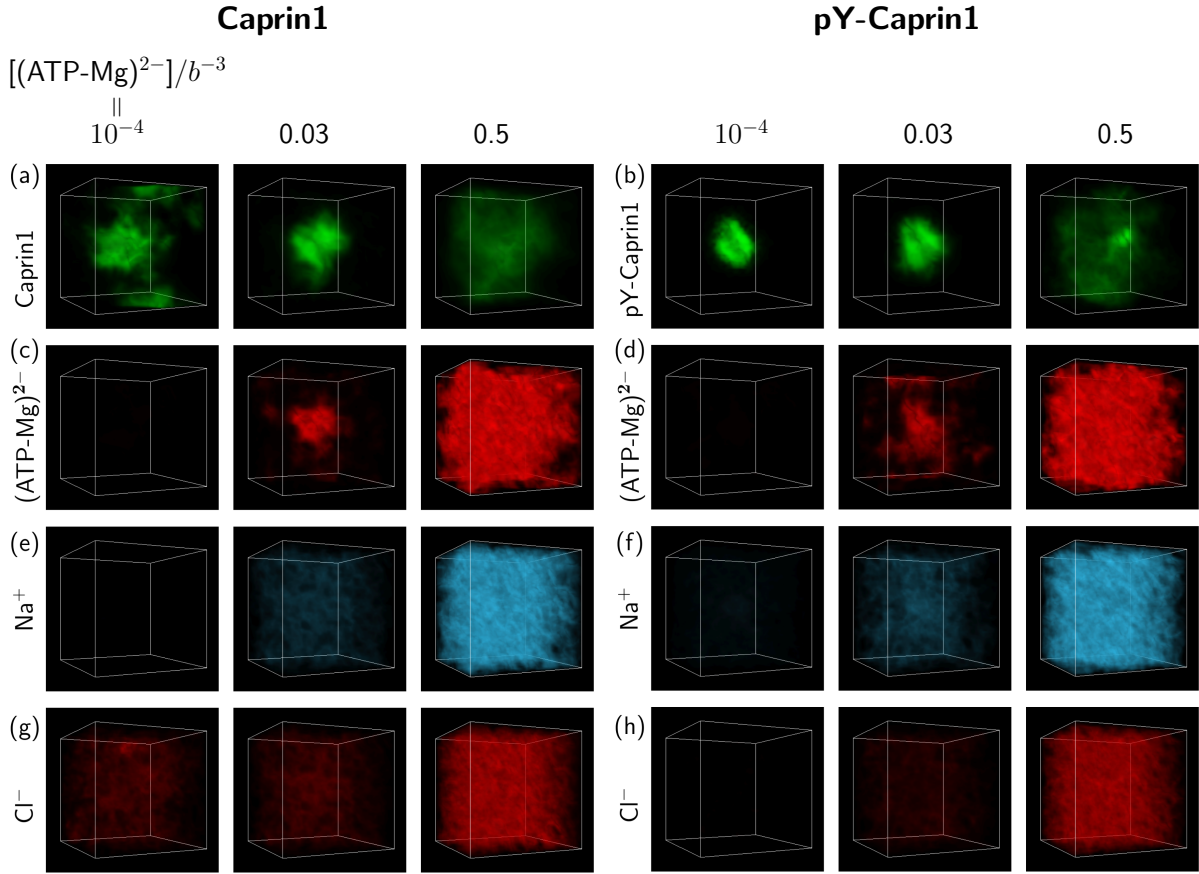


Figure 9: FTS rationalizes colocalization of ATP-Mg with the Caprin1 condensate. FTS snapshots are from simulations at $l_B = 7b$ (same as that for Fig. 8). Spatial distributions of real positive parts of the density fields for the protein (a, b), $(\text{ATP-Mg})^{2-}$ (c, d), Na^+ (e, f), and Cl^- (g, h) components are shown by three snapshots each for Caprin1 (left panels) and pY-Caprin1 (right panels) at different $[(\text{ATP-Mg})^{2-}]/b^{-3}$ values as indicated. Colocalization of $(\text{ATP-Mg})^{2-}$ with the Caprin1 condensed droplet is clearly seen in the $[(\text{ATP-Mg})^{2-}]/b^{-3} = 0.03$ panel of (c).

November 12, 2024

Supporting Information

(*SI Appendix*)

for

Electrostatics of Salt-Dependent Reentrant Phase Behaviors Highlights Diverse Roles of ATP in Biomolecular Condensates

Yi-Hsuan LIN,^{1,2,†,§} **Tae Hun KIM**,^{1,2,3,4,‡,§} **Suman DAS**,^{1,5,§} **Tanmoy PAL**,¹
Jonas WESSÉN,¹ **Atul Kaushik RANGADURAI**,^{1,2,3,4} **Lewis E. KAY**,^{1,2,3,4}
Julie D. FORMAN-KAY^{2,1} and **Hue Sun CHAN**^{1,*}

¹Department of Biochemistry, University of Toronto, Toronto, Ontario M5S 1A8, Canada

²Molecular Medicine, Hospital for Sick Children, Toronto, Ontario M5G 0A4, Canada

³Department of Molecular Genetics, University of Toronto,
 Toronto, Ontario M5S 1A8, Canada

⁴Department of Chemistry, University of Toronto, Toronto, Ontario M5S 3H6, Canada

⁵Department of Chemistry, Gandhi Institute of Technology and Management,
 Visakhapatnam, Andhra Pradesh 530045, India

[†]Present address: HTuO Biosciences, 1001 West Broadway, Suite 300, Vancouver, British Columbia V6H 4B1, Canada.

[‡]Present address: Department of Biochemistry, School of Medicine,
 Case Western Reserve University, Cleveland, Ohio 44106, U.S.A.

[§]Contributed equally.

*Correspondence information:

Hue Sun CHAN. E-mail: huesun.chan@utoronto.ca

Tel: (416)978-2697; Fax: (416)978-8548

Department of Biochemistry, University of Toronto, Medical Sciences Building – 5th Fl.,
 1 King's College Circle, Toronto, Ontario M5S 1A8, Canada.

Supporting Materials and Methods

Experimental information additional to that in the maintext

Sample preparation – Wildtype (WT) Caprin1. As stated in the maintext, WT Caprin1 was used in all reported experiments except those on [NaCl] dependence presented in maintext Table 1 and Fig. 3a. The amino acid sequence of WT Caprin1 is given in Fig. S1 (all supporting figures with figure numbers prefixed by “S” are provided in this *SI Appendix*). The preparation of sample WT Caprin1 is now briefly described as follows: Caprin1 with an N-terminal His-SUMO tag was produced in BL21 (DE3)-RIPL Codon Plus *E. coli* cells. These cells were cultured until an optical density at 600 nm (OD600) of 0.6 at 37°C and then induced with 0.5 mM IPTG for overnight expression at 23°C. The harvested cells were suspended in a lysis buffer containing 6 M guanidine hydrochloride (GuHCl), 25 mM Tris, 500 mM NaCl, 20 mM imidazole, 2 mM β -mercaptoethanol (BME), at pH 8.0, and lysed via sonication. The supernatant, post-sonication, was applied to Ni-NTA (Cytiva) and washed with lysis, wash (25 mM Tris, 500 mM NaCl, 20 mM imidazole, 2 mM BME, at pH 8.0), and elution (25 mM Tris, 500 mM NaCl, 300 mM imidazole, 2 mM BME, at pH 8.0) buffers. Post-elution, the sample was treated with ULP1 during dialysis against a dialysis buffer (25 mM Tris, 250 mM NaCl, and 2 mM BME at pH 8.0). This step was followed by His-SUMO tag removal through Ni-NTA column chromatography. Final purification of Caprin1 was performed using FPLC with a Superdex 75 16/60 column, equilibrated with a gel filtration buffer (3 M GuHCl, 25 mM Tris, 500 mM NaCl, 2 mM BME, pH 8.0). The protein fractions were then dialyzed twice to remove GuHCl before use in experiments.

Sample preparation – Double-mutant (N623T, N630T) variant of Caprin1. Our sample preparation for the double-mutant variant used in [NaCl] dependence studies reported in maintext Table 1 and Fig. 3a proceeded as follows. To abolish IsoAsp formation for the salt concentration measurements (Table 1) and the [NaCl]-dependent turbidity measurements in Fig. 3a, we used a double mutant of the Caprin1 IDR (N623T,N630T) in which the two asparagine residues are mutated to threonine. This double mutant has been shown to exhibit a similar propensity to phase separate as the WT Caprin1 IDR [85] purified as described previously [83, 85].

Purified Caprin1 was first exchanged into buffer (25mM sodium phosphate, pH 7.4) via dialysis and was concentrated to \sim 6 mM using 3 kDa centrifugal Amicon concentrators (EMD Millipore). The pH of the concentrated protein was adjusted to 7.4 using concentrated hydrochloric acid. Phase separated samples of Caprin1 were prepared by addition of a concentrated stock solution of NaCl (25mM sodium phosphate, pH 7.4, 4M NaCl) to achieve a bulk (overall) salt concentration of 300 mM NaCl. Condensed and dilute phases of Caprin1 were transferred all together into an Eppendorf tube using a syringe. After rigorous vortexing, the phase separated samples were incubated at the desired temperatures using a thermocycler with a heated lid (95°C). At least one hour was required to allow droplets to form a large condensed phase droplet at the bottom of the tube.

2 μ L of condensed and dilute phases were pipetted into 48 μ L of a 2.8 M urea solution

(U4883, Sigma) in MilliQ water in a 15 mL falcon tube, using a positive and an air displacement pipette, respectively. The outside of the tips were wiped with a KimWipe to remove excess protein, prior to transferring into the urea solutions. Following transfer, the samples were digested for inductively coupled plasma optical emission spectroscopy (ICP-OES) measurements by the addition of 630 μ L of concentrated nitric acid (67%, NX0407, Sigma) and 630 μ L hydrogen peroxide (95321, Sigma), and incubated in an oven at 60°C for 54 hours. Post digestion, the sample tubes were cooled at room temperature and centrifuged. 40 μ L of hydrogen peroxide was then added to the samples. No bubbles were observed, indicating the completion of the digestion process. The samples were then brought up to 12 mL using MilliQ water, to achieve a final nitric acid concentration of 3.5%. Blank samples for the condensed and dilute phases were prepared by pipetting 2 μ L of MilliQ water using a positive and an air displacement pipette, respectively, and subsequently following the digestion protocol described above. Sodium standards (0.1, 0.2, 0.5, 1, 2, 4, 8 and 10 ppm) in 3.5% nitric acid for ICP-OES measurements were prepared by dilution of sodium standard solution (00462, Sigma) with MilliQ water and concentrated nitric acid (67%, NX0407, Sigma). All samples were filtered using 0.22 μ m syringe filters prior to ICP-OES. Condensed and dilute phases were drawn in triplicate at each temperature.

Phosphorylation of the Caprin1 IDR. The purified protein was initially concentrated to 25-50 μ M in a reaction buffer comprising 25 mM Tris pH 7.4, 50 mM KCl, 10 mM MgCl₂, 3 mM ATP and 2 mM DTT. This mixture was then placed into a dialysis tubing with a 3 kDa cut-off. To the protein sample, purified His-SUMO-Eph4A was added to 5–10 μ M, and the reaction mixture was subsequently dialyzed against 4 liters of the same reaction buffer, either at room temperature or at 4°C overnight. Mass spectrometry indicates that the resulting sample consists mainly of a mixture of Caprin1 IDRs with six or seven phosphorylations and a very small fraction of IDRs with five phosphorylations (Fig. S2).

Determination of phase diagrams. The initial homogenization described in the maintext ensures that the condensed phase in small droplets can rapidly equilibrate with the dilute phase. Absorbance at 280 nm was measured and converted to concentration using the Beer-Lambert law, with an extinction coefficient (ϵ) of 10,430 M⁻¹cm⁻¹, based on the molecular masses of 11,108 Da for Caprin1 and 11,668 Da for pY-Caprin1. The reported concentration values and uncertainties, calculated as means and standard deviations, were derived from triplicate measurements.

Concentrations of salt and ATP-Mg in dilute and condensed phases. ICP-OES measurements were performed in triplicate for each sample. Mean value and uncertainty for the salt concentration were obtained by taking the average and standard deviation over the triplicate samples at the given temperature (maintext Table 1). Specific details of sample preparation for the set of ATP-Mg-dependent experiments are provided above in this *SI Appendix*. As for salt-dependent experiments, these measurements were performed in triplicate and standard deviations were calculated to assess experimental uncertainties

(maintext Table 2).

Caprin1 phase separation propensity at high salt concentrations. Averages and standard deviations over the three OD600 measurements were reported by the blue symbols in maintext Fig. 3a.

[ATP-Mg]-dependent Caprin1 phase behaviors. A brief summary of the turbidity assays in ref. [83] that we utilized is as follows: The WT Caprin1 IDR was diluted to a 200 μ M concentration using a buffer composed of 25 mM HEPES and 2 mM DTT at pH 7.4, with varying levels of ATP-Mg. Samples were prepared with ATP-Mg concentrations ranging from 0 to 40 mM. Following thorough mixing, 5 μ L of each sample was placed into a μ Cuvette G1.0 (Eppendorf), and OD600 was measured using a BioPhotometer D30 (Eppendorf). This procedure was performed three times for analysis of experimental uncertainties (red symbols in maintext Fig. 3a).

Sequence-specific theory of heteropolymer phase separation – Summary of key steps in the field-theoretic formulation

The following is a more extensive summary to supplement the brief outline in *Materials and Methods* of the maintext provided under the heading “sequence-specific theory of heteropolymer phase separation”. In general, sequence-specific polymer field theories [18, 71] are constructed to model systems of polymers with various salt and counterions. Further details are available from our recent publications (e.g., refs. [97, 119] and references therein).

Using the same notation for the partition function \mathcal{Z} in Eq. (2), with $\mathcal{T} + \mathcal{U}$ being the Hamiltonian in units of the product $k_B T$ of Boltzmann’s constant k_B and absolute temperature T , the connectivity term \mathcal{T} is given by

$$\mathcal{T}[\mathbf{R}] = \frac{3}{2l^2} \sum_{\alpha=1}^{n_p} \sum_{i=1}^{N-1} (\mathbf{R}_{\alpha,i+1} - \mathbf{R}_{\alpha,i})^2 \quad (\text{S1})$$

with $[\mathbf{R}]$ being shorthand for $[\{\mathbf{R}_{\alpha,i}\}]$. Considering the case when the total potential energy \mathcal{U} is taking one of its simplest forms, in that it serves only to model the two-body (pairwise) interactions among polymer residues, salt ions, and counterions, we further confine the interaction types in our formulation to Coulomb electrostatics (el) and excluded-volume (ex). As stated in the maintext, their interaction strengths are governed by the Bjerrum length l_B ($l_B = e^2/4\pi\epsilon_0\epsilon_r k_B T$, where e is protonic charge, ϵ_0 is vacuum permittivity, and ϵ_r is relative permittivity), and the two-body excluded volume parameter v_2 . We now provide the precise field-theoretic forms for the Coulomb electrostatic potential \mathcal{U}_{el} and two-body excluded volume interaction \mathcal{U}_{ex} terms in $\mathcal{U} = \mathcal{U}_{\text{el}} + \mathcal{U}_{\text{ex}}$ by introducing the number density

operators

$$\hat{\rho}_p(\mathbf{r}) = \sum_{\alpha=1}^{n_p} \sum_{i=1}^N \delta(\mathbf{r} - \mathbf{R}_{\alpha,i}) , \quad (\text{S2a})$$

$$\hat{\rho}_s(\mathbf{r}) = \sum_{a=1}^{n_s} \delta(\mathbf{r} - \mathbf{r}_a) , \quad (\text{S2b})$$

$$\hat{\rho}_c(\mathbf{r}) = \sum_{a=n_s+1}^{n_s+n_c} \delta(\mathbf{r} - \mathbf{r}_a) , \quad (\text{S2c})$$

for the monomers (residues or beads) of the polymer (p), salt (s), and counterion (c), respectively, where δ represents the Dirac δ distribution. Solvent (water) degrees of freedom [n_w in Eq. (2) for \mathcal{Z} in the maintext] are not included in Eq. (S2) above because they are only used for the incompressibility constraint in our rG-RPA formulation as an approximate treatment of excluded volume, and solvents are not treated explicitly at all in the present field-theoretic simulation (FTS), i.e., the n_w factor is dropped for FTS. The corresponding charge density operators for the number density operators in Eq. (S2) are

$$\hat{c}_p(\mathbf{r}) = \sum_{\alpha=1}^{n_p} \sum_{i=1}^N \sigma_i \delta(\mathbf{r} - \mathbf{R}_{\alpha,i}) , \quad (\text{S3a})$$

$$\hat{c}_s(\mathbf{r}) = z_s \sum_{a=1}^{n_s} \delta(\mathbf{r} - \mathbf{r}_a) = z_s \hat{\rho}_c , \quad (\text{S3b})$$

$$\hat{c}_c(\mathbf{r}) = z_c \sum_{a=n_s+1}^{n_s+n_c} \delta(\mathbf{r} - \mathbf{r}_a) = z_c \hat{\rho}_s . \quad (\text{S3c})$$

For \hat{c}_p , $\sigma_i = +1$ for arginine and lysine, $\sigma_i = -1$ for aspartic and glutamic acids, $\sigma_i = -2$ for phosphorylated tyrosine, and $\sigma_i = 0$ for all other amino acid residues in the Caprin1/pY-Caprin1 sequences studied (as stated in the maintext). \mathcal{U}_{el} and \mathcal{U}_{ex} are now given by

$$\mathcal{U}_{\text{el}} = \frac{l_B}{2} \int d\mathbf{r} d\mathbf{r}' \left[\hat{c}_p(\mathbf{r}) + \hat{c}_s(\mathbf{r}) + \hat{c}_c(\mathbf{r}) \right] \frac{1}{|\mathbf{r} - \mathbf{r}'|} \left[\hat{c}_p(\mathbf{r}') + \hat{c}_s(\mathbf{r}') + \hat{c}_c(\mathbf{r}') \right] , \quad (\text{S4a})$$

$$\mathcal{U}_{\text{ex}} = \frac{v_2}{2} \int d\mathbf{r} \left[\hat{\rho}_p(\mathbf{r}) + \hat{\rho}_s(\mathbf{r}) + \hat{\rho}_c(\mathbf{r}) \right]^2 . \quad (\text{S4b})$$

As mentioned in the maintext, two conjugates fields, $\psi(\mathbf{r})$ for Coulomb interaction and $w(\mathbf{r})$ for excluded volume, are then introduced to linearize the density operators that are quadratic in \mathcal{U}_{el} and \mathcal{U}_{ex} by applying the Hubbard-Stratonovich transformation [151, 152], resulting in a reformulated partition function $\mathcal{Z}' \equiv (n_p! n_s! n_c! n_w!) \mathcal{Z}$ [with \mathcal{Z} given by Eq. (2)

of maintext] expressed as a functional integral over the fields ψ and w :

$$\mathcal{Z}' = \int \mathcal{D}\psi \mathcal{D}w \exp \left[- \int d\mathbf{r} \left(\frac{[\nabla\psi(\mathbf{r})]^2}{8\pi l_B} + \frac{w(\mathbf{r})^2}{2v_2} \right) + n_p \ln \mathcal{Q}_p + n_s \ln \mathcal{Q}_s + n_c \ln \mathcal{Q}_c \right], \quad (\text{S5})$$

where \mathcal{Q}_p , \mathcal{Q}_s , and \mathcal{Q}_c are single-molecule partition functions of polymer, salt ion, and counterion, respectively, which are all functionals of ψ and w :

$$\begin{aligned} \mathcal{Q}_p[\psi, w] &= \int \prod_{\tau=1}^N d\mathbf{R}_\tau \exp \left(-\mathcal{H}_p[\mathbf{R}; \psi, w] \right) \\ &= \int \prod_{\tau=1}^N d\mathbf{R}_\tau \exp \left[-\frac{3}{2l^2} \sum_{i=1}^{N-1} (\mathbf{R}_{i+1} - \mathbf{R}_i)^2 - i \sum_{i=1}^N (\sigma_i \psi(\mathbf{R}_i) + w(\mathbf{R}_i)) \right], \end{aligned} \quad (\text{S6a})$$

$$\mathcal{Q}_{s,c}[\psi, w] = \int d\mathbf{r} \exp \left[-i(z_{s,c}\psi(\mathbf{r}) + w(\mathbf{r})) \right], \quad (\text{S6b})$$

wherein i is the imaginary unit, i.e., $i^2 = -1$.

The \mathcal{Z}' in Eq. (S5) can be analyzed via various field theoretic approaches. Two approaches are utilized in the present work: (i) one-loop perturbation expansion is employed to derive analytical theories based upon random-phase-approximation (RPA), and (ii) field-theoretic simulation (FTS) is conducted to compute observables numerically.

Renormalized-Gaussian random-phase-approximation (rG-RPA)

As mentioned in the maintext, sequence-specific random phase approximation (RPA) has been applied successfully to model electrostatic effects on the LLPSs of various polyampholytic IDRs [7, 18, 44, 94, 101] to obtain behavioral trends consistent with experiments and explicit-chain simulations; but RPA is less appropriate for polyelectrolytes with large net charge per residue (NCPR) [102–104] because of RPA’s treatment of polymers as ideal Gaussian chains [105]. This approximation is reasonable for polyampholytes but not for polyelectrolytes. While overall intrachain electrostatic effects in polyampholytes can be mild because of the polymers’ nearly zero net charge and thus entail only a minor perturbation on conformational statistics, repulsive electrostatics in polyelectrolytes with significant net charge is strong, leading to more rod-like conformations with statistics deviating significantly from that of Gaussian chains. Consequently, treating polyelectrolytes as Gaussian chains can lead to large errors in theoretical intrachain and interchain residue-residue (monomer-monomer) correlations, resulting in drastically overestimated LLPS propensities [105].

The rG-RPA theory was put forth by some of the present authors [71]. For a broad overview, we briefly summarize here the major methodological steps and key results of the theory. Interested readers are referred to ref. [71] for further details. As rG-RPA has been designed and verified to tackle polyelectrolyte conformations appropriately [71], we apply it here to the polyelectrolytic Caprin1 IDR. Because rG-RPA allows for a smooth crossover between polyelectrolytic and polyampholytic systems, Caprin1 and pY-Caprin1 can now be analyzed in a universal theoretical formulation without invocation of ad hoc treatments for

their different conformational statistics.

In our formulation of rG-RPA theory, simplifying assumptions are made to the effect that excluded volume is taken into account only between pairs of different polymer chains (no consideration of intrachain excluded volume) and small ions are treated as point charges. Denoting the input “bare” Kuhn length as l , and the total free energy and volume of the system as F and Ω respectively, the system free energy in units of $k_B T$ per volume l^3 is given by

$$f = \frac{Fl^3}{k_B T \Omega} = -s + f_{\text{ion}} + f_0 + f_p. \quad (\text{S7})$$

Here s is translational entropy

$$-s = \frac{\phi_p}{N} \ln \phi_p + \phi_s \ln \phi_s + \phi_c \ln \phi_c + \phi_w \ln \phi_w, \quad (\text{S8})$$

where ϕ_p , ϕ_s , ϕ_c , and $\phi_w = 1 - \phi_p - \phi_s - \phi_c$ are, respectively, volume fractions of polymers, salt ions, counterions, and solvent, with the last equality following from the incompressibility condition that we have stipulated. The f_{ion} term in Eq. (S7) accounts for the free energy of the small ions via the form

$$f_{\text{ion}} = -\frac{1}{4\pi} \left[\ln(1 + \kappa_D l) - \kappa l + \frac{1}{2} (\kappa_D l)^2 \right], \quad (\text{S9})$$

where $1/\kappa_D = 1/\sqrt{4\pi l_B (z_s^2 \rho_s + z_c^2 \rho_c)}$ is the Debye screening length. The term f_0 in Eq. (S7) is the zeroth-order excluded volume effect given by

$$f_0 = \frac{l^3}{2} v_2 \rho_m^2, \quad (\text{S10})$$

where $\rho_m = n_p N / \Omega$ is the average monomer (residue or bead) density of the polymers in the system and the expression $f_p = -(l^3 / \Omega) \ln \mathcal{Z}_p$ for the last term in Eq. (S7) is derived from the polymer partition function

$$\mathcal{Z}_p = \int \mathcal{D}\psi \mathcal{D}w \exp \left[- \int d\mathbf{r} \left(\frac{\psi(\mathbf{r}) (-\nabla^2 + \kappa^2)^2 \psi(\mathbf{r})}{8\pi l_B} + \frac{w(\mathbf{r})^2}{2v_2} \right) + n_p \ln \mathcal{Q}_p \right]. \quad (\text{S11})$$

An analytical perturbative field theory may now be derived from \mathcal{Z}_p by considering the Taylor expansion of $\ln \mathcal{Q}_p$ up to the second order of ψ and w while omitting terms that do not affect the relative energies of the configurations, viz.,

$$\ln \mathcal{Q}_p \approx -\frac{1}{2} \left[\langle (\hat{c}_p - \bar{c}_p)^2 \rangle \psi^2 + \langle (\hat{\rho}_p - \bar{\rho}_p)^2 \rangle w^2 + 2 \langle (\hat{c}_p - \bar{c}_p) (\hat{\rho}_p - \bar{\rho}_p) \rangle \psi w \right], \quad (\text{S12})$$

where \bar{c}_p and $\bar{\rho}_p$ are the overall average charge and number densities, respectively, of the polymer [cf. Eqs. (S2) and (S3) above and Eq. (A37) of ref. [71]]. It follows that \mathcal{Z}_p can

then be approximated as a Gaussian integral in the Fourier-transformed \mathbf{k} -space,

$$\mathcal{Z}_p \approx \int \prod_{\mathbf{k} \neq \mathbf{0}} \sqrt{\frac{\nu_k}{v_2}} \frac{d\psi_{\mathbf{k}} dw_{\mathbf{k}}}{2\pi\Omega} \exp \left[-\frac{1}{2\Omega} \sum_{\mathbf{k} \neq \mathbf{0}} \langle \psi_{-\mathbf{k}} w_{-\mathbf{k}} | \begin{pmatrix} \nu_k + \rho_m g_{\mathbf{k}}^{cc} & \rho_m g_{\mathbf{k}}^{mc} \\ \rho_m g_{\mathbf{k}}^{mc} & v_2^{-1} + \rho_m g_{\mathbf{k}}^{mm} \end{pmatrix} | \psi_{\mathbf{k}} \rangle \right], \quad (S13)$$

where $g_{\mathbf{k}}^{cc}$, $g_{\mathbf{k}}^{mm}$, and $g_{\mathbf{k}}^{mc}$ are charge-charge, mass-mass (i.e., matter-matter), and mass-charge (matter-charge) correlation functions in \mathbf{k} -space, and $\nu_k = k^2/(4\pi l_B) + (z_s^2 \rho_s + z_c^2 \rho_c)$. The free energy f_p is then given by

$$f_p = \frac{l^3}{2} \int \frac{d^3 k}{(2\pi)^3} \ln \left[1 + \rho_m \left(\frac{g_{\mathbf{k}}^{cc}}{\nu_k} + v_2 g_{\mathbf{k}}^{mm} \right) + \frac{v_2}{\nu_k} \rho_m^2 (g_{\mathbf{k}}^{cc} g_{\mathbf{k}}^{mm} - (g_{\mathbf{k}}^{mc})^2) \right]. \quad (S14)$$

The correlation functions in Eq. (S14) may be estimated by various field-theory approximations. In rG-RPA, they are evaluated using a variational approach to the single-polymer partition function \mathcal{Q}_p by first expressing the Hamiltonian \mathcal{H}_p in Eq. (3) of the maintext as the sum of an approximate Gaussian-chain Hamiltonian with an effective (renormalized) Kuhn length xl (recall l is the original “bare” Kuhn length) plus the remaining term:

$$\mathcal{H}_p = \mathcal{H}_p^0 + \mathcal{H}_p^1, \quad (S15)$$

where

$$\mathcal{H}_p^0 = \frac{3}{2l^2 x} \sum_{i=1}^{N-1} (\mathbf{R}_{i+1} - \mathbf{R}_i)^2, \quad (S16a)$$

$$\mathcal{H}_p^1 = \frac{3}{2l^2} \left(1 - \frac{1}{x} \right) \sum_{i=1}^{N-1} (\mathbf{R}_{i+1} - \mathbf{R}_i)^2 - \frac{1}{x} \sum_{i=1}^N [\sigma_i \psi(\mathbf{R}_i) + w(\mathbf{R}_i)] \quad (S16b)$$

are the same equations as Eqs. (4a) and (4b) in the maintext and adopt essentially the same form as the unrenormalized Eq. (S6a). To make progress, we take the polymer square end-to-end distance \mathbf{R}_{EE}^2 as a key physical observable and require its thermodynamic average to be produced by \mathcal{H}_p^0 in good approximation. Based on this premise, a variational theory as described in ref. [43] is applied to calculate the x parameter in the above Eq. (S16). Details of the derivation are given in the Appendices of ref. [71]. Here we show only the variational equation for solving x :

$$1 - \frac{1}{x} - \frac{Nl^3}{18(N-1)} \int \frac{d^3 k}{(2\pi)^3} \frac{k^2 \Xi_k^x}{\det \Delta_k^x} = 0, \quad (S17)$$

where Δ_k^x is the 2×2 matrix in Eq. (S13) with $l \rightarrow xl$ (renormalized Kuhn length), $|i-j| \rightarrow |i-j|/x$ (renormalized contour length) and thus $l^2|i-j| \rightarrow l^2x|i-j|$ such that

the correlation functions in Δ_k^x become [71]

$$g_{\mathbf{k}}^{cc} \rightarrow g_{k,x}^{cc} = \frac{1}{N} \sum_{i,j=1}^N \sigma_i \sigma_j e^{-\frac{1}{6}(kl)^2 x|i-j|}, \quad (\text{S18a})$$

$$g_{\mathbf{k}}^{mm} \rightarrow g_{k,x}^{mm} = \frac{1}{N} \sum_{i,j=1}^N e^{-\frac{1}{6}(kl)^2 x|i-j|}, \quad (\text{S18b})$$

$$g_{\mathbf{k}}^{mc} \rightarrow g_{k,x}^{mc} = \frac{1}{N} \sum_{i,j=1}^N \sigma_i e^{-\frac{1}{6}(kl)^2 x|i-j|}, \quad (\text{S18c})$$

and the Ξ_k^x in the integrand on the right hand side of Eq. (S17) is now given by

$$\Xi_k^x = \frac{\bar{\zeta}_k^x}{v_2} + \nu_k \bar{g}_k^x + \rho_m (\bar{\zeta}_k^x g_{k,x}^{mm} + \bar{g}_k^x g_{k,x}^{cc} - 2\bar{\zeta}_k^x g_{k,x}^{mc}) \quad (\text{S19})$$

where

$$\bar{\zeta}_k^x = \frac{1}{N} \sum_{i,j=1}^N |i-j|^2 \sigma_i \sigma_j e^{-\frac{1}{6}(kl)^2 x|i-j|}, \quad (\text{S20a})$$

$$\bar{g}_k^x = \frac{1}{N} \sum_{i,j=1}^N |i-j|^2 e^{-\frac{1}{6}(kl)^2 x|i-j|}, \quad (\text{S20b})$$

$$\bar{\zeta}_k^x = \frac{1}{N} \sum_{i,j=1}^N |i-j|^2 \sigma_i e^{-\frac{1}{6}(kl)^2 x|i-j|}. \quad (\text{S20c})$$

The rG-RPA+FH formulation. Because the above field theory is formulated to focus only on sequence-specific electrostatics and excluded volume, in the form presented above it does not account for short-range attractions such as those arising from π -related and hydrophobic effects; but we need to take these effects into consideration to arrive at a more direct comparison between rG-RPA predictions and experiments, e.g., as those provided in Fig. 1c,d of the maintext. To account for these interactions approximately in Caprin1, particularly the interactions involving π -electrons [84], we introduce, as before [18], a temperature-dependent Flory-Huggins (FH) interaction to augmented the free energy f in Eq. (S7) [71, 94], resulting in an overall total free energy

$$f = -s + f_{\text{ion}} + f_0 + f_{\text{p}} - (\epsilon_h/T^* + \epsilon_s) \rho_{\text{m}}^2, \quad (\text{S21})$$

where ϵ_h and ϵ_s are the enthalpic and entropic components, respectively, of the mean-field Flory-Huggins interaction for favorable non-electrostatic attraction, and $T^* = l/l_{\text{B}}$ is the reduced temperature. With this augmented rG-RPA+FH system free energy f in hand, we solve the solute and solvent concentrations in dilute and condensed phases by balancing the chemical potentials of each solute components and the osmotic pressures in the two phases. When the salt concentration is assumed for simplicity to be uniform throughout the system

(Fig. 1c,d of the maintext), the system only has ρ_m as a variable and the binodal phase separation concentrations are readily obtained by solving the standard common tangent conditions [97, 153]. The Flory-Huggins parameters ϵ_h and ϵ_s fitted to the experimental data are $\epsilon_h = 1.0$, $\epsilon_s = 0.0$ for the Caprin1 phase diagrams in Fig. 1c and $\epsilon_h = 1.0$, $\epsilon_s = -1.5$ for the pY-Caprin1 phase diagrams in Fig. 1d. When the uniform salt concentration restriction is removed to allow for fully varying salt and polymer concentrations (Fig. 2 of the maintext), the final concentrations in the two phases depend on their initial bulk (overall) concentrations. The corresponding two-dimensional, polymer-salt phase diagram (at a given temperature T) is obtained by similar balancing conditions [154]. As stated in the maintext, the two-dimensional rG-RPA+FH phase diagrams in Fig. 2 are for $T = 300$ K.

rG-RPA-predicted effects of counterion valency on Caprin1 LLPS. As discussed in the maintext, with monovalent salt (Na^+), rG-RPA predicts that Caprin1 does not undergo LLPS at $[\text{Na}^+] = 0$ when the counterion (Cl^-) is monovalent (maintext Fig. 2a,b), but Caprin1 LLPS is possible at $[\text{Na}^+] = 0$ when the counterion is divalent (maintext Fig. 2e,f). As mentioned in the maintext, a likely physical reason for this effect is the difference in configurational entropy loss of monovalent vs divalent counterions in the Caprin1-condensed phase. Apparently, when $[\text{Cl}^-]$ is just sufficient to balance the net positive charge of Caprin1 (i.e., when $[\text{Na}^+] = 0$), the entropic cost of concentrating Cl^- in a Caprin1-condensed phase cannot be overcome for Caprin1 LLPS to occur. The entropic cost will be lessened (and thus more favorable to Caprin1 LLPS) when there are more Cl^- ions beyond what is necessary to balance the net positive charge of Caprin1, corresponding to a situation with nonzero $[\text{Na}^+]$ from the added NaCl to supply the additional Cl^- ions. In comparison, when the counterion is divalent [$(\text{ATP-Mg})^{2-}$ in our case], the number of counterions needed for balancing the positive net charge of Caprin1 is half of that when the counterion is monovalent. It follows that the entropic cost of concentrating the divalent counterion in the Caprin1-condensed phase is less and consequently, at least in the present situation, no added salt is needed for Caprin1 LLPS.

Explicit-ion coarse-grained explicit-chain molecular dynamics (MD) simulation

Coarse-grained MD simulations are performed with the GPU version of HOOMD-Blue software [155, 156] using the slab method that has been developed recently to allow for simulations of relatively large number of polymers [114] and applied to liquid-liquid phase separation (LLPS) of intrinsically disordered proteins (IDPs) [88]. This general MD protocol has been utilized extensively [96, 157], including by our group [94, 158].

Within the methodological framework of this coarse-grained simulation protocol, we introduce explicit small ions into our present simulations because they are necessary to account for subtle experimental observations that are not readily reproduced by using implicit-ion electrostatic screening. Simulations in the present study are performed with 100 chains of the Caprin1 IDR (wildtype or variants) at four salt ($[\text{NaCl}]$) concentrations: (i) at $[\text{NaCl}] = 0$ where the system is neutralized by adding appropriate number (1,300) of chloride (Cl^-) ions, (ii) neutralized and at $[\text{NaCl}] = 200$ mM by adding 15,000 pairs of

explicit Na^+ and Cl^- ions, (iii) neutralized and at $[\text{NaCl}] = 480 \text{ mM}$ by adding the same number of 15,000 pairs of explicit Na^+ and Cl^- ions, and (iv) neutralized and at $[\text{NaCl}] = 960 \text{ mM}$ again with 15,000 pairs of explicit Na^+ and Cl^- ions. As will be described below, specific small-ion concentrations in (ii), (iii), and (iv) are implemented by varying the size of the final simulation box. A similar procedure is used for simulation of pY-Caprin1 IDR phase behaviors under these four $[\text{NaCl}]$ values. Because each pY-Caprin1 IDR has a net -1 charge, the only difference with the Caprin1 IDR simulation is that neutralization of the pY-Caprin1 chain requires 100 Na^+ ions instead of 1,300 Cl^- ions. The amino acid sequences simulated using coarse-grained MD in the present study are provided in Fig. S1. Note that the experimental pY-Caprin1 sample is highly phosphorylated, consisting mainly of a mixture of Caprin1 IDRs with six or seven phosphorlations, with only a very small fraction of IDRs with five phosphorylations, and essentially no population with fewer than five phosphorylations (Fig. S2). As stated in the maintext, for the sake of simplicity in our theoretical/computational models, we use only the Caprin1 IDR with all seven tyrosines phosphorylated (referred to simply as pY-Caprin1 in Fig. S1) to model the behaviors of this experimental sample, partly to avoid the combinatoric complexity of sequences with five or six phosphorlations, which would entail 21 and 7 possible different sequences, respectively, with currently unknown population fractions.

Coarse-grained MD interaction potentials. Following prior works [88, 94], each amino acid residue is modeled by a single bead. Beads representing different amino acid residues have different masses, sizes, and engage in pairwise interactions with different strengths [88, 94]. Following the notations of our earlier simulation works [90, 94, 158], we consider n_p number of polymers labeled as $\mu, \nu = 1, 2, \dots, n_p$, with each polymer consisting of N beads labeled by $i, j = 1, 2, \dots, N$, and n_c counterions to neutralize the charged polymers. Coarse-grained MD is readily applicable to studying variations in LLPS properties among RtoK variants [94] considered here for Caprin1 (Fig. S1). In contrast, since RtoK substitutions do not change the sequence charge pattern of any given sequence, rG-RPA theory as formulated above does not account for their effects on LLPS, though polymer field theory can be extended to incorporate such effects in more sophisticated formulations [119].

For salt-dependent LLPS ($n_s \neq 0$), we consider n_+ small cations and n_- small anions. These small cations and anions are classified as salt ions or counterions depending on the net charge of the polymer (see maintext as well as discussion below in this *SI Appendix*). The small ions are labeled, respectively, by $\gamma = 1, 2, \dots, n_+$ and $\beta = 1, 2, \dots, n_-$, and they correspond to Na^+ and Cl^- in the present coarse-grained MD simulations. As stated in the maintext, our total MD potential energy is the sum of electrostatic (el), short-spatial-range (sr) Lennard-Jones (LJ)-type, and bonding (bond) interactions:

$$U_T = U_{\text{el}} + U_{\text{sr}} + U_{\text{bond}} . \quad (\text{S22})$$

For our systems of interest, the electrostatic part is a sum of polymer-polymer (pp),

polymer–small-ion (pi), and small-ion–small-ion (ii) contributions:

$$U_{\text{el}} = U_{\text{el,pp}} + U_{\text{el,pi}} + U_{\text{el,ii}}. \quad (\text{S23})$$

As before [119], the polymer-polymer potential energy is given by

$$U_{\text{el,pp}} = \frac{e^2}{8\pi\epsilon_0\epsilon_r} \sum_{\mu,\nu=1}^{n_p} \sum_{i,j=1}^N \left(1 - \delta_{\mu\nu}\delta_{ij}\right) \frac{\sigma_i\sigma_j}{r_{\mu i,\nu j}}, \quad (\text{S24})$$

where, as in the above field-theoretic formulation, e is protonic charge, ϵ_0 is vacuum permittivity, and ϵ_r is relative permittivity (dielectric constant). Here, $r_{\mu i,\nu j}$ is the spatial distance between the i th residue of the μ th polymer and the j th residue of the ν th polymer. The Kronecker symbol δ signals exclusion of the self-interacting $\mu = \nu$, $i = j$ terms in the summations (irrespective of the values of these terms) because $1 - \delta_{xy} = 0$ if $x = y$ and $1 - \delta_{xy} = 1$ otherwise. In units of the protonic charge e , σ_i of unphosphorylated amino acid residue beads are taken from ref. [88]. Except lysine and arginine ($\sigma_i = +1$), glutamic and aspartic acid ($\sigma_i = -1$), histidine ($\sigma_i = +0.5$)—but note that there is no histidine in the Caprin1/pY-Caprin1 sequences simulated here, and phosphorylated tyrosine ($\sigma_i = -2$), all other amino acid residues are assigned zero charge. Similarly, the interaction between polymers and small ions is given by

$$U_{\text{el,pi}} = \frac{e^2}{4\pi\epsilon_0\epsilon_r} \sum_{\mu=1}^{n_p} \sum_{i=1}^N \left\{ \sum_{k=+,-} \left[\sum_{\gamma(k)=1}^{n_{\gamma}(k)} \frac{\sigma_i\sigma_k}{r_{\mu i,\gamma(k)}} \right] \right\} = \frac{e^2}{4\pi\epsilon_0\epsilon_r} \sum_{\mu=1}^{n_p} \sum_{i=1}^N \left[\sum_{\gamma=1}^{n_+} \frac{\sigma_i\sigma_+}{r_{\mu i,\gamma}} + \sum_{\beta=1}^{n_-} \frac{\sigma_i\sigma_-}{r_{\mu i,\beta}} \right], \quad (\text{S25})$$

where, in the term after the first equality, the summation \sum_k (enclosed in curly brackets) is over small ion types, summation indices $\gamma(+)$ and $\gamma(-)$ label, respectively, the positively and negatively charged small ions, $n_{\gamma}(+)$ and $n_{\gamma}(-)$ are the total numbers of these ions, and $r_{\mu i,\gamma(k)}$ is the spatial distance between the i th residue of the μ th polymer chain and the small ion labeled by $\gamma(k)$. After the second equality, the two terms in \sum_k are written explicitly, now with $r_{\mu i,\gamma/\beta}$ being the spatial distance between the i th residue of the μ th polymer chain and the γ/β (γ or β)-labeled positive/negative small ion as well as σ_+ and σ_- being the charges of the small positive and negative small ions, respectively. Following ref. [159], we take $\sigma_+ = +1$ for Na^+ and $\sigma_- = -1$ for Cl^- . Depending on the net charge of the polymer, counterions can be included in either the n_+ or n_- count. For instance, for the positive charged Caprin1 IDR, the total number n_- of negatively charged small ions (Cl^-) includes the numbers n_c counted as counterions and n_s counted as salt ions.

The interaction between the small ions is given by

$$U_{\text{el,ii}} = \frac{e^2}{8\pi\epsilon_0\epsilon_r} \sum_{k,k'=+,-} \left[\sum_{\gamma(k)=1}^{n_{\gamma}(k)} \sum_{\gamma'(k')=1}^{n'_{\gamma}(k')} \left(1 - \delta_{kk'}\delta_{\gamma(k)\gamma'(k')}\right) \frac{\sigma_k\sigma_{k'}}{r_{\gamma(k),\gamma'(k')}} \right], \quad (\text{S26})$$

where $r_{\gamma(k),\gamma'(k')}$ is the spatial distance between two small ions. For the MD simulations in this work, the positively and negatively charged small ions correspond to Na^+ and Cl^-

respectively. Eq. (S26) is equivalent to

$$U_{\text{el,ii}} = \frac{e^2}{4\pi\epsilon_0\epsilon_r} \left[\sum_{\gamma=1}^{n_+-1} \sum_{\gamma'=\gamma+1}^{n_+} \frac{\sigma_+^2}{r_{\gamma\gamma'}} + \sum_{\beta=1}^{n_--1} \sum_{\beta'=\beta+1}^{n_-} \frac{\sigma_-^2}{r_{\beta\beta'}} + \sum_{\gamma=1}^{n_+} \sum_{\beta=1}^{n_-} \frac{\sigma_+\sigma_-}{r_{\gamma\beta}} \right], \quad (\text{S27})$$

where r_{xy} is the spatial distance between a pair of small ions labeled by x and y . As rationalized previously [94] in the context of experimental measurements of dielectric properties of biological systems [160], we use $\epsilon_r = 40$, a value lower than the ~ 80 dielectric constant of bulk water, for all simulations reported in the present work.

Short-spatial-range non-bonded LJ interactions are similarly constituted by three components, viz., those for polymer-polymer ($U_{\text{sr,pp}}$), polymer-small-ion ($U_{\text{sr,pi}}$), and small-ion-small-ion ($U_{\text{sr,ii}}$) interactions:

$$U_{\text{sr}} = U_{\text{sr,pp}} + U_{\text{sr,pi}} + U_{\text{sr,ii}}. \quad (\text{S28})$$

Here we adopt the Kim-Hummer (KH) [161] interaction scheme for $U_{\text{sr,pp}}$. KH is based on the Miyazawa-Jernigan (MJ) statistical potential [162] derived from folded globular protein structures in the Protein Data Bank (PDB) and is therefore expected to reflect the energetics of polypeptides, especially the driving forces pertinent to protein folding, its limitations [94] notwithstanding. Our previous work shows that the KH potential is adequate for rationalizing the rank ordering of LLPS propensities of the N-terminal IDR of DEAD-box RNA helicase Ddx4 and its charge scrambled and arginine-to-lysine (RtoK) variants. KH also rationalizes the rank ordering of LLPS propensities of WT and an RtoK variant of LAF-1 [94]. We therefore stipulate that the KH interaction scheme is appropriate, at least as a first approximation, to address the LLPS propensities of Caprin1 and its RtoK variants. The degree to which the differences in simulated LLPS propensity among these Caprin1 variants are affected by how interactions involving K and R are treated differently by the model potential function [94, 96, 118] should be further explored in the future. As before, $U_{\text{sr,pp}}$ takes the following form [88, 94]:

$$U_{\text{sr,pp}} = \frac{1}{2} \sum_{\mu,\nu=1}^{n_p} \sum_{i,j=1}^N \left(1 - \delta_{\mu\nu} \delta_{ij}\right) (U_{\text{KH}})_{\mu i, \nu j}, \quad (\text{S29})$$

$$(U_{\text{KH}})_{\mu i, \nu j} = U_{\text{LJ}} + (1 - \lambda_{ij}^{\text{KH}}) \epsilon_{ij} \quad \text{if } r \leq 2^{1/6} a_{ij}$$

$$= \lambda_{ij}^{\text{KH}} U_{\text{LJ}} \quad \text{otherwise}$$

in which

$$(U_{\text{LJ}})_{\mu i, \nu j} = U_{\text{LJ}}(\epsilon_{\mu i, \nu j}, a_{\mu i, \nu j}, r_{\mu i, \nu j}) = 4\epsilon_{\mu i, \nu j} \left[\left(\frac{a_{\mu i, \nu j}}{r_{\mu i, \nu j}} \right)^{12} - \left(\frac{a_{\mu i, \nu j}}{r_{\mu i, \nu j}} \right)^6 \right] \quad (\text{S30})$$

and $a_{\mu i, \nu j} = a_{ij} = (a_i + a_j)/2$, where the van der Waals diameters a_i and a_j , depend only, respectively, on the amino acid residue type (one of twenty) for residue i and residue j (Table S1 of ref. [88]). In contrast, the parameters λ_{ij}^{KH} and $\epsilon_{\mu i, \nu j} = \epsilon_{ij}$ depend on both the

residue types of residues i and j . Values for ϵ_{ij} are provided in Table S3 of ref. [88]. The formula for $\lambda_{ij}^{\text{KH}} = \pm 1$ is given by Eq. (5) of ref. [88] as well as Eqs. (S10) and (S11) of ref. [94].

For the LJ interactions between polymers and small ions, we recognize that while the coarse-grained KH parameters are based on statistical analysis of known folded protein structures, LJ interaction parameters for small ions are typically scaled to match certain physical and chemical properties [159]. Thus it is not straightforward to postulate an interaction scheme based upon first principles. To make progress and to maintain simplicity of our model, we adopt the LJ form [U_{LJ} in Eq. (S30)] for $U_{\text{sr,pi}}$ with a uniform $\epsilon_{\mu i, \nu j} = \epsilon_{ij} = 0.142$ (denoted $\epsilon_{p\pm} \equiv 0.142$) for all residue-small ion pairs. This $\epsilon_{ij} = \epsilon_{p\pm}$ value is equal to that for a pair of alanine residues in the KH potential and is neither too strong nor too weak among ϵ_{ij} values for pairwise interactions between amino acid residues. Accordingly,

$$U_{\text{sr,pi}} = \sum_{\mu=1}^{n_p} \sum_{i=1}^N \left[\sum_{\gamma=1}^{n_+} U_{\text{LJ}}(\epsilon_{p\pm}, a_{i+}, r_{\mu i, \gamma}) + \sum_{\beta=1}^{n_-} U_{\text{LJ}}(\epsilon_{p\pm}, a_{i-}, r_{\mu i, \beta}) \right], \quad (\text{S31})$$

where $a_{i+} = (a_i + a_+)/2$, $a_{i-} = (a_i + a_-)/2$, with a_+ and a_- being, respectively, the van der Waals diameters of the positively and negatively charged small ions. For the present MD simulations, $a_+ = a_{\text{Na}^+}$, $a_- = a_{\text{Cl}^-}$, and their values are adopted from ref. [159]. Similarly, for small-ion-small-ion LJ interactions,

$$U_{\text{el,ii}} = \left[\sum_{\gamma=1}^{n_+-1} \sum_{\gamma'=\gamma+1}^{n_+} U_{\text{LJ}}(\epsilon_+, a_+, r_{\gamma, \gamma'}) + \sum_{\beta=1}^{n_--1} \sum_{\beta'=\beta+1}^{n_-} U_{\text{LJ}}(\epsilon_-, a_-, r_{\beta, \beta'}) \right. \\ \left. + \sum_{\gamma=1}^{n_+} \sum_{\beta=1}^{n_-} U_{\text{LJ}}(\epsilon_{+-}, a_{+-}, r_{\gamma, \beta}) \right], \quad (\text{S32})$$

where ϵ_+ and ϵ_- are, respectively, the LJ interaction energy parameter for the positively and negatively charged small ions, $\epsilon_{+-} = (\epsilon_+ \epsilon_-)^{1/2}$, and $a_{+-} = (a_+ + a_-)/2$. For the present MD simulations, the $\epsilon_+ = \epsilon_{\text{Na}^+}$ and $\epsilon_- = \epsilon_{\text{Cl}^-}$ values are also adopted from ref. [159].

As before, the bond-length energy term U_{bond} in Eq. (S22) for chain connectivity is modeled by a harmonic potential,

$$U_{\text{bond}} = \frac{K_{\text{bond}}}{2} \sum_{\mu=1}^{n_p} \sum_{i=1}^{N-1} (r_{\mu i, \nu i+1} - l)^2. \quad (\text{S33})$$

Following previous studies [88, 94], Kuhn length $l = 3.8 \text{ \AA}$ is taken as the $\text{C}_\alpha\text{--C}_\alpha$ virtual bond length for *trans* polypeptides and $K_{\text{bond}} = 10 \text{ kJmol}^{-1}\text{\AA}^{-2}$.

Simulation protocol. In each of our coarse-grained MD simulations, the IDR chains and ions are initially placed randomly in a sufficiently large cubic box of dimensions $300 \times 300 \times 300 \text{ \AA}^3$. Energy minimization is then performed using the FIRE algorithm (available in the HOOMD-Blue package) which includes removal of steric clashes among

the initially placed amino acid beads. Next, the system is compressed at a low temperature of 100 K at 1 atm pressure for a period of 50 ns using the Martyna-Tobias-Klein (MTK) thermostat and barostat [163, 164] with a coupling constant of 1 ps. The equations of motion are integrated using velocity-Verlet algorithm with a timestep of 20 fs. Periodic boundary conditions are applied in all three directions. The electrostatic interaction is computed using the PPPM algorithm [165] available in the package. We use a cut-off distance of 15 Å for the short-spatial-range non-bonded interactions. After this initial *NPT* step, we compress the simulation box again along the three dimensions for a period of 50 ns until it reaches a sufficiently high density, using Langevin dynamics for an *NVT* ensemble with a friction coefficient of 1 ps⁻¹. At the end of this compression step, the dimensions of the simulation box for Caprin1 and its four RtoK variants are 115 × 115 × 115 Å³ for [NaCl] = 0 (no small ions beside counterions) and 155 × 155 × 155 Å³ for [NaCl] = 200 mM, 480 mM, and 960 mM. For pY-Caprin1, the corresponding dimensions are 115 × 115 × 115 Å³ for [NaCl] = 0 (no small ions beside counterions) and 150 × 150 × 150 Å³ for [NaCl] = 200 mM, 480 mM, and 960 mM. Next, the system is expanded along one of the spatial dimensions (taken as the *z*-axis) using isotropic linear scaling for 10 ns while keeping the temperature constant at 100 K. For Caprin1 and its four RtoK variants, the simulation box length in the *z*-direction is expanded 14 times for [NaCl] = 0, 33.6 times for [NaCl] = 200 mM, 14 times for [NaCl] = 480 mM, and 7 times for [NaCl] = 960 mM. For pY-Caprin1, the expansion factors along the *z*-direction are 10 times for [NaCl] = 0, 37.07 times for [NaCl] = 200 mM, 15.47 times for [NaCl] = 480 mM, and 7.73 times for [NaCl] = 960 mM. Note that the simulation box volumes for Caprin1, its RtoK variants, and pY-Caprin1 after this last expansion are identical for the same [NaCl] because the same numbers of polymer chains and small ions are used. The practical reason for keeping the number of Na⁺ and Cl⁻ ions constant for the higher salt concentration is to minimize computational cost. In other words, the three salt concentrations (200 mM, 480 mM and 960 mM) are achieved here by using different box dimensions. After the last box expansion, *NVT* equilibration using the Langevin thermostat with a friction coefficient of 1 ps⁻¹ is performed for 2 μs at various temperatures. Final production run is then carried out for another 4 μs with the same Langevin thermostat using a much lower friction coefficient of 0.01 ps⁻¹ for sampling efficiency. The snapshots are saved every 1 ns for further analysis. Detailed descriptions of how to construct a phase diagram from simulation trajectories are provided in ref. [88] and our previous works [94, 97]. This simulation protocol and the above-described coarse-grained MD model are used to produce the phase diagrams, distributions, and snapshots in Figs. 4–7 of the maintext and Fig. S3.

Comparison with atomic simulations with a preformed condensate. As mentioned in the maintext, explicit-water, explicit-ion atomic simulations in the presence of a preformed condensate of the N-terminal RGG domain of LAF-1 with a net charge of +4 produce enhanced Cl⁻ and depleted Na⁺ in the IDR-condensed phase [120]. This trend is consistent with our implicit-water, explicit-ion MD result for Caprin1 with net charge +13 (maintext Fig. 4c). By comparison, corresponding atomic simulations in the presence of a preformed condensate of the low complexity domain of FUS with a net charge of -2 produce a significant depletion of Cl⁻ and a minor depletion of Na⁺ in the

IDR-condensed phase [120], which is opposite to the trend seen here for pY-Caprin1 with net charge -1 in maintext Fig. 4d and Fig. S3. Whether this difference is caused by the multiple phosphorylated sites with a -2 charge in pY-Caprin1 remains to be elucidated.

Field-theoretic simulation (FTS) for multiple-component LLPS

Biomolecular condensates *in vivo* can contain hundreds of protein and nucleic acid species. Therefore, to address their biophysical properties and biochemical functions, theories—starting with rudimentary constructions—are needed for multiple-component LLPS. As a first approximation and a tool for conceptualization, we find it valuable to utilize FTS—especially recently developed FTS approaches for biomolecular LLPS [91, 98, 122, 127] and their extensions—to gain insights into the energetic basis of sequence-specific spatial distributions of various biomolecular components in and out of phase-separated condensates.

FTS enjoys the fundamental advantage that it is not limited by some of the approximations in analytical theories such as RPA and rG-RPA because FTS accounts fully for all field fluctuations in principle. FTS is thus a valuable alternative to analytical theories, though it is computationally more costly in practice and can be impeded by lattice-related artifacts and limitations arising from the small FTS simulation box sizes necessitated by numerical tractability. We view analytical theories and FTS as complementary.

The starting point of FTS is a statistical field theory [e.g., Eq. (S5), which is equivalent to maintext Eq. (5)]. To avoid numerical instabilities, we treat polymer beads and ions as (smeared) Gaussian distributions [166] instead of the point particles stipulated by the Dirac δ -functions in Eqs. (S2) and (S3). For simplicity, this regularization is implemented using a common component-independent width \bar{a} irrespective of chemical species by making the general replacements $\delta(\mathbf{r} - \mathbf{r}_a) \rightarrow \Gamma(\mathbf{r} - \mathbf{r}_a)$ and $\delta(\mathbf{r} - \mathbf{R}_{\alpha,i}) \rightarrow \Gamma(\mathbf{r} - \mathbf{R}_{\alpha,i})$, in Eqs. (S2) and (S3) where $\Gamma(\mathbf{r}) = e^{-r^2/2\bar{a}^2}/(2\pi\bar{a}^2)^{3/2}$, $r^2 = |\mathbf{r}|^2$.

A general field-theoretic Hamiltonian applicable to a system comprising of one or more charged polymer species including Caprin1, pY-Caprin1, $(\text{ATP-Mg})^{2-}$ (maintext Fig. 8a), ATP^{4-} and small ions such as Na^+ , Cl^- , and Mg^{2+} is given by

$$H[w, \psi] = \int d\mathbf{r} \left(\frac{(\nabla\psi(\mathbf{r}))^2}{8\pi l_B} + \frac{w(\mathbf{r})^2}{2v_2} \right) - \sum_m n_m \ln \mathcal{Q}_m[\check{w}, \check{\psi}] , \quad (\text{S34})$$

where the \mathcal{Q}_m functionals (m labels system components) are in general complex when evaluated beyond quadratic order in the fields. Equation (S34) above is identical to Eq. (5) of maintext and formally equivalent to the Hamiltonian in Eq. (S5). Because of the above-described Gaussian smearing, the fields in the arguments of \mathcal{Q}_m are now convoluted with Γ , i.e. $\phi(\mathbf{r}) \rightarrow \check{\phi}(\mathbf{r}) = \Gamma \star \phi(\mathbf{r}) \equiv \int d\mathbf{r}' \Gamma(\mathbf{r} - \mathbf{r}') \phi(\mathbf{r}')$, where the generic $\phi = w, \psi$.

Complex Langevin evolution in fictitious time. A simulation approach developed in the 1980s to handle the complex nature of $H[w, \psi]$ and obtain statistical (Boltzmann) averages is the Complex Langevin (CL) method [123, 124], which analytically continues the fields w and ψ into their respective complex planes and introduces an fictitious (artifi-

cial, unphysical) time-coordinate t on which $w(\mathbf{r}, t)$ and $\psi(\mathbf{r}, t)$ now depend. The CL time evolution is governed by stochastic Langevin differential equations [maintext Eq. (6)], as follows:

$$\frac{\partial \phi(\mathbf{r}, t)}{\partial t} = -\frac{\delta H}{\delta \phi(\mathbf{r}, t)} + \eta_\phi(\mathbf{r}, t) , \quad \phi = w, \psi , \quad (\text{S35})$$

where $\eta_\phi(\mathbf{r}, t)$ is real-valued Gaussian noise with zero mean:

$$\langle \eta_\phi(\mathbf{r}, t) \eta_{\phi'}(\mathbf{r}', t') \rangle = 2\delta_{\phi, \phi'} \delta(\mathbf{r} - \mathbf{r}') \delta(t - t') . \quad (\text{S36})$$

Thermal averages of any thermodynamic observable $\hat{\mathcal{O}}[\mathbf{R}, \mathbf{r}]$ can then be computed in the field picture (indicated by “ $\langle \dots \rangle_F$ ” with subscript “F”) using a corresponding field operator $\tilde{\mathcal{O}}[w, \psi]$ through averages over all possible equilibrium field configurations, which in turn translate into asymptotic CL time averages with no final dependence on the fictitious time variable t , i.e.,

$$\langle \tilde{\mathcal{O}}[w, \psi] \rangle_F \equiv \frac{\int \mathcal{D}w \int \mathcal{D}\psi \tilde{\mathcal{O}}[w, \psi] e^{-H[w, \psi]}}{\int \mathcal{D}w \int \mathcal{D}\psi e^{-H[w, \psi]}} = \lim_{t_{\max} \rightarrow \infty} \frac{1}{t_{\max}} \int_0^{t_{\max}} dt \tilde{\mathcal{O}}[w(\mathbf{r}, t), \psi(\mathbf{r}, t)] . \quad (\text{S37})$$

The Langevin Eq. (S35) involves functional derivatives of the Hamiltonian with respect to the complex fields, which are formally evaluated as

$$\frac{\delta H}{\delta w(\mathbf{r})} = \sum_m \tilde{\rho}_m(\mathbf{r}) + \frac{1}{v_2} w(\mathbf{r}) , \quad (\text{S38a})$$

$$\frac{\delta H}{\delta \psi(\mathbf{r})} = \sum_m \tilde{c}_m(\mathbf{r}) - \frac{1}{4\pi l_B} \nabla^2 \psi(\mathbf{r}) , \quad (\text{S38b})$$

where

$$\tilde{\rho}_m(\mathbf{r}) = m_m \frac{\delta \ln \mathcal{Q}_m[\check{w}, \check{\psi}]}{\delta w(\mathbf{r})} , \quad (\text{S39a})$$

$$\tilde{c}_m(\mathbf{r}) = m_m \frac{\delta \ln \mathcal{Q}_m[\check{w}, \check{\psi}]}{\delta \psi(\mathbf{r})} \quad (\text{S39b})$$

are field operators corresponding, respectively, to number- and charge density of chemical component m .

Number density correlation functions. Information about the polymer-polymer, polymer-ion, ion-ion association and ion partitioning into the condensate can be gleaned from number density-number density correlation functions [maintext Eq. (7)]

$$G_{m,n}(|\mathbf{r} - \mathbf{r}'|) = \langle \hat{\rho}_m(\mathbf{r}) \hat{\rho}_n(\mathbf{r}') \rangle , \quad (\text{S40})$$

which can be computed in field theory [98] as

$$G_{m,n \neq m}(|\mathbf{r} - \mathbf{r}'|) = \langle \tilde{\rho}_m(\mathbf{r}) \tilde{\rho}_n(\mathbf{r}') \rangle_F, \quad (\text{S41a})$$

$$G_{m,m}(|\mathbf{r} - \mathbf{r}'|) = \frac{1}{v_2} \langle \tilde{\rho}_m(\mathbf{r}) w(\mathbf{r}') \rangle_F - \sum_{n \neq m} \langle \tilde{\rho}_m(\mathbf{r}) \tilde{\rho}_n(\mathbf{r}') \rangle_F. \quad (\text{S41b})$$

The $G_{m,n}$ functions are useful for assessing Caprin1 and pY-Caprin1 phase separation and the colocalization of ATP-Mg with the polymer condensed droplet (maintext Fig. 8b–e). Information with higher spatial resolution can also be provided by $G_{m,n}$ if we identify component m with individual polymer bead (labeled by i) along a chain sequence.

In some situations, the physical implications of density-density correlation functions $G_{m,n}(r)$ are more apparent when normalized by the component bulk (overall) densities ρ_m^0 and ρ_n^0 , as discussed in the maintext in connection with the correlation functions shown in Fig. 8.

For small ions that are each represented by a single Gaussian distribution, the density operator is given by

$$\tilde{\rho}_m(\mathbf{r}) = \frac{n_m}{\Omega \mathcal{Q}_k} \Gamma \star e^{-i[\check{w}(\mathbf{r}) + z_m \check{\psi}(\mathbf{r})]}, \quad (\text{S42})$$

and the charge density operator is $\tilde{c}_m(\mathbf{r}) = z_m \tilde{\rho}_m(\mathbf{r})$, where z_m is the charge of ion species m and, as defined above, Ω is the system volume. For polymers (denoted “p”), the density and charge-density operators are calculated using forward (subscript “F”) and backward (subscript “B”) chain propagators $q_F(\mathbf{r}, i)$ and $q_B(\mathbf{r}, i)$ as follows, with i being the label for the beads/monomers along the polymer chain:

$$\mathcal{Q}_p = \frac{1}{\Omega} \int d\mathbf{r} q_F(\mathbf{r}, N), \quad (\text{S43a})$$

$$\tilde{\rho}_p(\mathbf{r}) = \frac{n_p}{\Omega \mathcal{Q}_p} \Gamma \star \sum_{i=1}^N q_F(\mathbf{r}, i) q_B(\mathbf{r}, i) e^{i[\check{w}(\mathbf{r}) + \sigma_i \check{\psi}(\mathbf{r})]}, \quad (\text{S43b})$$

$$\tilde{c}(\mathbf{r}) = \frac{n_p}{\Omega \mathcal{Q}_p} \Gamma \star \sum_{i=1}^N q_F(\mathbf{r}, i) q_B(\mathbf{r}, i) e^{i[\check{w}(\mathbf{r}) + \sigma_i \check{\psi}(\mathbf{r})]} \sigma_i, \quad (\text{S43c})$$

and the chain propagators are constructed iteratively as

$$q_F(\mathbf{r}, i+1) = e^{-i[\check{w}(\mathbf{r}) + \sigma_{i+1} \check{\psi}(\mathbf{r})]} \left(\frac{3}{2\pi b^2} \right)^{3/2} \int d\mathbf{r}' e^{-3(\mathbf{r}-\mathbf{r}')^2/2b^2} q_F(\mathbf{r}', i), \quad (\text{S44a})$$

$$q_B(\mathbf{r}, i-1) = e^{-i[\check{w}(\mathbf{r}) + \sigma_{i-1} \check{\psi}(\mathbf{r})]} \left(\frac{3}{2\pi b^2} \right)^{3/2} \int d\mathbf{r}' e^{-3(\mathbf{r}-\mathbf{r}')^2/2b^2} q_B(\mathbf{r}', i) \quad (\text{S44b})$$

with the starting $q_F(\mathbf{r}, 1) = e^{-i[\check{w}(\mathbf{r}) + \sigma_1 \check{\psi}(\mathbf{r})]}$, $q_B(\mathbf{r}, N) = e^{-i[\check{w}(\mathbf{r}) + \sigma_N \check{\psi}(\mathbf{r})]}$, and we use b for Kuhn length ($b = l$) in the present FTS formulation to conform to the notation in our published FTS studies [97, 98, 119]. In the present work, the correlation functions in maintext Fig. 8 and Figs. S4–S6 are computed by integrating pertinent CL fictitious-time evolution equations defined in Eq. (S35) using the first order semi-implicit method of

ref. [167].

Residue-specific Caprin1–(ATP-Mg) association. As outlined in *Materials and Methods* of the maintext, residue-specific properties of the polymers in our FTS systems can be gleaned from the $G_{m,n}$ function in Eq. (S40) by identifying m as individual polymer beads (indexed by i) along the polymer chain sequence, viz., define $G_{pq}^{(i)}(|\mathbf{r} - \mathbf{r}'|) \equiv \langle \hat{\rho}_{p,i}(\mathbf{r}) \hat{\rho}_q(\mathbf{r}') \rangle$ where $\hat{\rho}_{p,i}(\mathbf{r}) \equiv \sum_{\alpha=1}^N \Gamma(\mathbf{r} - \mathbf{R}_{\alpha,i})$, the corresponding operator $\hat{\rho}_{p,i}(\mathbf{r})$ being equal to the i th term in the summation in Eq. (S43b), and q is another component in the FTS system. Accordingly [maintext Eq. (9)],

$$\mathcal{G}_{pq}^{(i)} \equiv 4\pi \int_0^{r_{\text{contact}}} dr r^2 G_{pq}^{(i)}(r) \quad (\text{S45})$$

with a reasonably small residue- q distance r_{contact} (spatial separation between residue i and the positions of particles belonging to component q) can be used to represent residue-specific relative residue- q contact frequencies. A normalized version of this quantity is defined by

$$\frac{\mathcal{G}_{pq}^{(i)}}{\rho_{p,i}^0 \rho_q^0} = 4\pi \int_0^{r_{\text{contact}}} dr r^2 g_{pq}^{(i)}(r), \quad g_{pq}^{(i)}(r) \equiv \frac{G_{pq}^{(i)}(r)}{\rho_{p,i}^0 \rho_q^0}, \quad (\text{S46})$$

where ρ_q^0 and $\rho_{p,i}^0$ are the bulk (overall) densities, respectively, of the q -component and the i th residue along the given polymer species. Values of $\mathcal{G}_{pq}^{(i)} / \rho_{p,i}^0 \rho_q^0$ in the above Eq. (S46) for $p = \text{Caprin1}$ and $q = (\text{ATP-Mg})^{2-}$, Na^+ , or Cl^- under the simulation conditions we considered are provided in maintext Fig. 8f. The variation in $\mathcal{G}_{pq}^{(i)} / \rho_{p,i}^0 \rho_q^0$ for $(\text{ATP-Mg})^{2-}$ with residue position i is largely consistent with the experimental trend of NMR-measured volume ratios on Caprin1-ATP association in ref. [84].

In all the FTS simulations in this study except for a part of the model with no $(\text{ATP-Mg})^{2-}$ described immediately below, we use a cubic simulation box of length $L = N_L \Delta x$ where $N_L = 32$ (i.e., a $32 \times 32 \times 32$ lattice) and $\Delta x = b/\sqrt{6}$ is the lattice resolution. In view of the periodic boundary conditions implemented for all three spatial dimensions, the maximum possible physical distance between two volume elements is $\sqrt{3}L/2$. All possible physical distances $r = r_{i,j,k}$ on this cubic simulation box satisfy the relation $r_{i,j,k}^2 = [\min\{i, N_L - i\}^2 + \min\{j, N_L - j\}^2 + \min\{k, N_L - k\}^2] \Delta x^2$, for some $i, j, k = 0, 1, 2, \dots, 31$. There is thus a finite number of discretized distances between 0 and $\sqrt{3}L/2$. One of these discretized distances, $r = 1.47b \approx 1.50b$ is used for the $\int_0^{r_{\text{contact}}} dr$ integrations in maintext Eq. (9) and Eqs. (S45) and (S46) above.

Further details of the main FTS model utilized for the results in maintext Figs. 8 and 9 as well as alternate FTS models discussed under the heading “Robustness of general trends predicted by field-theoretic simulation” in the maintext are provided below in ascending order of number of components treated by the model:

FTS models of Caprin1/pY-Caprin1 with Na^+ and Cl^- but no ATP-Mg. FTS is conducted for Caprin1 and pY-Caprin1 at various concentrations of explicit Na^+ and Cl^- ions. For all systems, polymer bead concentration is fixed at $n_p N / \Omega = 0.4b^{-3}$. The salt

concentrations, here referring to the concentration of the small ion species with same sign charge as the net charge of the polymer, are set to $[\text{NaCl}] b^3 = 0, 10^{-6}, 10^{-5}, \dots 10^{-1}, 10^0$. Additional small ions of charge opposite to the polymer net charge are added to achieve overall electric neutrality of the system. For the results in Fig. S4e–h, simulations are performed in an elongated simulation box on a $24 \times 24 \times 80$ lattice with lattice spacing set to the Gaussian smearing length, $\Delta x = \bar{a} = b/\sqrt{6}$. The Complex-Langevin (CL) evolution equations [Eq. (S35)] are integrated using a time-step $\Delta t = 10^{-3}b^3$ for 6×10^4 steps and the system is sampled every 50th step. An equilibration period of 3×10^4 CL steps, determined by monitoring the equilibration of the chemical potentials for each molecular species, is discarded from each trajectory. Eight independent simulations are run for each combination of salt concentration and Caprin1 or pY-Caprin1. All simulations are performed at $l_B = 7b$ and $v_2 = 0.0068b^3$. The density profiles shown in Fig. S4e,f are obtained by averaging the real part of the field theoretic polymer bead density operator over the x - and y dimensions (i.e. the dimensions corresponding to the short sides of the simulation box). The resulting one-dimensional density snapshots were then individually centred around their center-of-mass z -coordinate $z_{\text{c.o.m.}}$ before taking the trajectory average to give the profiles in Fig. S4e,f. The shaded uncertainty bands in these plots indicate the root-mean-squared difference among the eight independent runs. The density profiles are then used to estimate the coexisting condensed and dilute phases shown in Fig. S4g,h. Here, the condensed-phase concentration is obtained as the average density at $z_{\text{c.o.m.}}$, whereas the dilute-phase concentrations are estimated as the average density among the 10 and 60 z -coordinates (for Caprin1 and pY-Caprin1, respectively) furthest from $z_{\text{c.o.m.}}$. Consistent with rG-RPA and explicit-MD, these FTS models show reentrant behavior—albeit subtle—for Caprin1 at low [protein]s (an LLPS region is seen in Fig. S4g at intermediate $[\text{NaCl}]$ s but not at higher or lower $[\text{NaCl}]$ s) but not for pY-Caprin1 (no such feature in Fig. S4h).

FTS models for Caprin1/pY-Caprin1 with $(\text{ATP-Mg})^{2-}$ and either Na^+ or Cl^- . Simulations are performed at $l_B = 5b$ on a periodic $32 \times 32 \times 32$ grid (see above) with CL time step $\Delta t = 0.002$. All ATP^{4-}s and Mg^{2+}s are assumed to be in the complex $(\text{ATP-Mg})^{2-}$ form with charge sequence (-1 -1 -1 -1 +1 +1) as depicted in maintext Fig. 8a. Bulk Caprin1 and pY-Caprin1 bead densities in the their respective simulation systems are both set at $0.1b^{-3}$. For Caprin1, depending on the concentration of $(\text{ATP-Mg})^{2-}$, counterions Na^+ or Cl^- (but not both) are added to maintain overall electric neutrality of the FTS system. For pY-Caprin1, Na^+ is added as counterions to maintain overall electric neutrality. Results from this set of models are provided in Fig. S5. The bands representing sampling uncertainties in the correlation function plots in maintext Fig. 8b–e and Fig. S5 (top) and Fig. S6a,b are standard deviations across eight independent simulations. If we take the model Kuhn length b in FTS as the $\text{C}_\alpha\text{-C}_\alpha$ virtual bond length $\approx 3.8 \text{ \AA}$ of polypeptides, a unit bead concentration of b^{-3} is equivalent to $\approx 30 \text{ M}$. Because $(\text{ATP-Mg})^{2-}$ is modeled by six beads (Fig. 8a of maintext), a model bead concentration of $(\text{ATP-Mg})^{2-}$ (denoted as $[(\text{ATP-Mg})^{2-}]$ in our FTS results) which is equal to b^{-3} reported for the present FTS results is equivalent to a molar concentration of $\approx 5 \text{ M}$ of $(\text{ATP-Mg})^{2-}$. As mentioned above, since excluded volume is often significantly underestimated in FTS

[98], we do not directly compare FTS model $(\text{ATP-Mg})^{2-}$ concentrations with experimental $(\text{ATP-Mg})^{2-}$ concentrations, which tend to be substantially lower. Instead, physical insights are gleaned from the trend of variation of model concentrations.

FTS models for Caprin1/pY-Caprin1 with $(\text{ATP-Mg})^{2-}$, Na^+ and Cl^- . We use this set of models for the results in maintext Figs. 8 and 9. Simulations are performed at $l_B = 7b$ on a periodic $32 \times 32 \times 32$ grid (see above) with CL time step $\Delta t = 0.005$. Again, all ATP^{4-} s and Mg^{2+} s are assumed to be in the complex $(\text{ATP-Mg})^{2-}$ form with charge sequence (-1 -1 -1 -1 +1 +1) as depicted in maintext Fig. 8a. Bulk Caprin1 and pY-Caprin1 bead densities in the their respective simulation systems are both set at $0.1b^{-3}$. Three concentrations of $(\text{ATP-Mg})^{2-}$ are studied: $[(\text{ATP-Mg})^{2-}] = 0.0001b^{-3}$, $0.03b^{-3}$, and $0.5b^{-3}$. With overall electric neutrality of the simulation system in mind, for Caprin1 (WT), the bulk (overall) densities for Na^+ and Cl^- are $[\text{Na}^+] = 4[(\text{ATP-Mg})^{2-}]/6$ and $[\text{Cl}^-] = 2[(\text{ATP-Mg})^{2-}]/6 + 13[\text{Caprin1}]/103$. For pY-Caprin1, $[\text{Na}^+] = 4[(\text{ATP-Mg})^{2-}]/6 + [\text{pY-Caprin1}]/103$ and $[\text{Cl}^-] = 2[(\text{ATP-Mg})^{2-}]/6$.

FTS models for Caprin1/pY-Caprin1 with ATP^{4-} , Mg^{2+} , Na^+ and Cl^- . In contrast to the above models, here we consider ATP^{4-} and Mg^{2+} as independent components. That is, they can freely dissociate if the favorable electric interaction between them is insufficiently strong. In this set of models, ATP^{4-} is taken as a four-bead charge sequence (-1 -1 -1 -1) whereas Mg^{2+} is modeled by a single bead with charge 2+ [instead of the two -1 beads in the $(\text{ATP-Mg})^{2-}$ model in maintext Fig. 8a]. As before, bulk (overall) Caprin1 and pY-Caprin1 bead densities in the their respective simulation systems are both set at $0.1b^{-3}$, and the same three $[(\text{ATP-Mg})^{2-}] = 0.0001b^{-3}$, $0.03b^{-3}$, and $0.5b^{-3}$ are studied. For Caprin1 (WT), the bulk (overall) densities for Mg^{2+} , ATP^{4-} , Na^+ and Cl^- are given by $[\text{Mg}^{2+}] = [\text{ATP}^{4-}]/4$, $[\text{Na}^+] = [\text{ATP}^{4-}]$, and $[\text{Cl}^-] = 2[\text{Mg}^{2+}] + 13[\text{Caprin1}]/103$. For pY-Caprin1, $[\text{Mg}^{2+}] = [\text{ATP}^{4-}]/4$, $[\text{Na}^+] = [\text{ATP}^{4-}] + [\text{pY-Caprin1}]/103$, and $[\text{Cl}^-] = 2[\text{Mg}^{2+}]$. Results from this set of FTS models are provided in Fig. S6.

Supporting Figures

WT:

SRGVSRGGSRGARGLMNGYRGPANGFRGGYDGYRPSFSNTPNSGYTQSQFSAPRDYSGYQRD
GYQQNFKRGSGQSGPRGAPRGRGGPPRPNRGMPQMNTQQVN

4Rto4K_N:

SKGVSKGGSKGAKGLMNGYRGPANGFRGGYDGYRPSFSNTPNSGYTQSQFSAPRDYSGYQR
DGYQQNFKRGSGQSGPRGAPRGRGGPPRPNRGMPQMNTQQVN

4Rto4K_M:

SRGVSRGGSRGARGLMNGYRGPANGFKGGYDGYKPSFSNTPNSGYTQSQFSAPKDYSGYQK
DGYQQNFKRGSGQSGPRGAPRGRGGPPRPNRGMPQMNTQQVN

4Rto4K_C:

SRGVSRGGSRGARGLMNGYRGPANGFRGGYDGYKPSFSNTPNSGYTQSQFSAPRDYSGYQRD
GYQQNFKKGSGQSGPKGAPKGKGPPRPNRGMPQMNTQQVN

15Rto15K:

SKGVSKGGSKGAKGLMNGYKGPANGFKGGYDGYKPSFSNTPNSGYTQSQFSAPKDYSGYQK
DGYQQNFKKGSGQSGPKGAPKGKGPPKPNKGMPQMNTQQVN

pY Caprin1:

SRGVSRGGSRGARGLMNGpYRGPANGFRGGpYDGpYRPSFSNTPNSGpYTQSQFSAPRDpYSG
pYQRDGpYQQNFKRGSGQSGPRGAPRGRGGPPRPNRGMPQMNTQQVN

Fig. S1: Sequences of wildtype (WT) and variant Caprin1 IDR studied in this work. Positively charged arginine (R) and lysine (K) residues are shown, respectively, in dark and light blue, negatively charged aspartic acid (D) residues and phosphorylated tyrosines (pY) are shown in red. Other residues are in black.

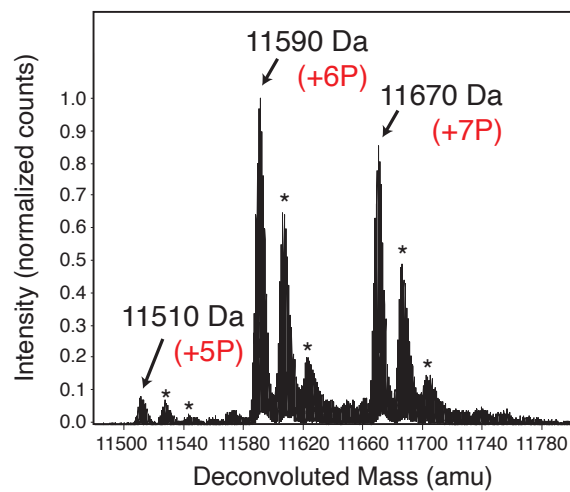


Fig. S2: Mass spectrometry analysis of pY-Caprin1. The graph plots deconvoluted mass (in atomic mass units, amu) on the horizontal axis against intensity (normalized counts) on the vertical axis. Peaks are observed at 11510 Da (+5 phosphate groups, +5P), 11590 Da (+6P), and 11670 Da (+7P). Asterisks mark the peaks of pY-Caprin1 with oxidized methionine residues.

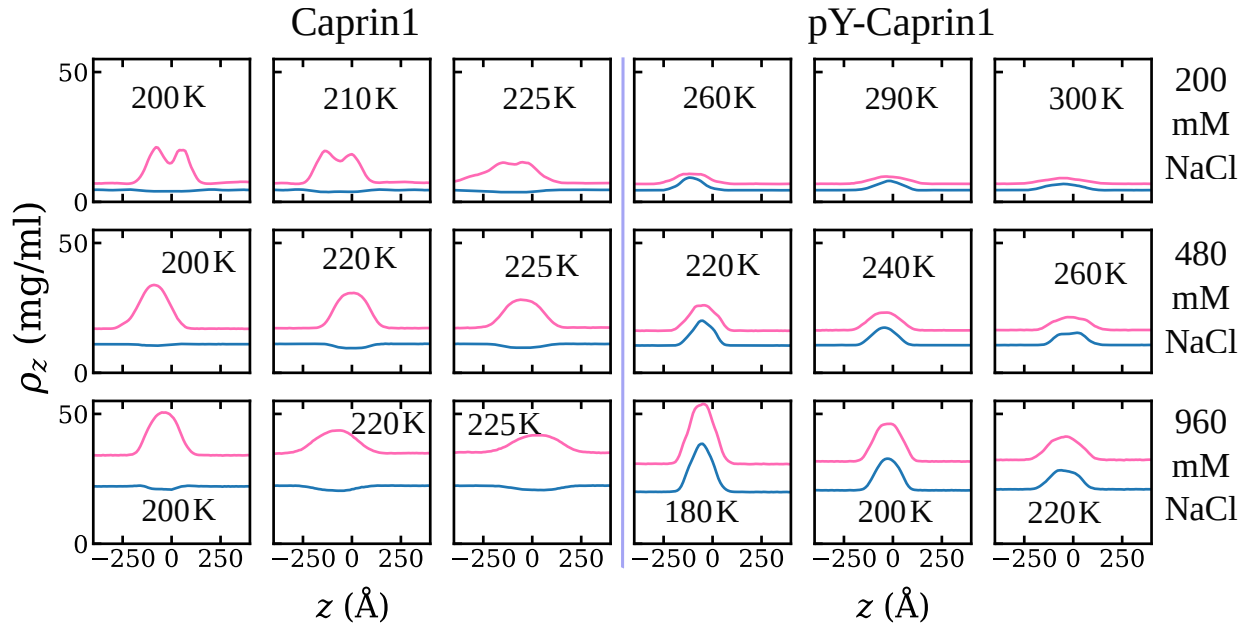


Fig. S3: Explicit-ion coarse-grained molecular dynamics simulation of salt and counterion mass density profiles in protein-dilute and protein-condensed phases of Caprin1 and pY-Caprin1. Mass density profile ρ_z for Na^+ (blue) and Cl^- (red) in units of mg/ml for the Caprin1 (three left columns) and pY-Caprin1 (three right columns) systems are shown as in Fig. 4e,f of the maintext. Regions with elevated $[\text{Cl}^-]$ here coincide with positions of the condensed protein droplets. Overall $[\text{NaCl}]$ values used for the simulations are provided on the right.

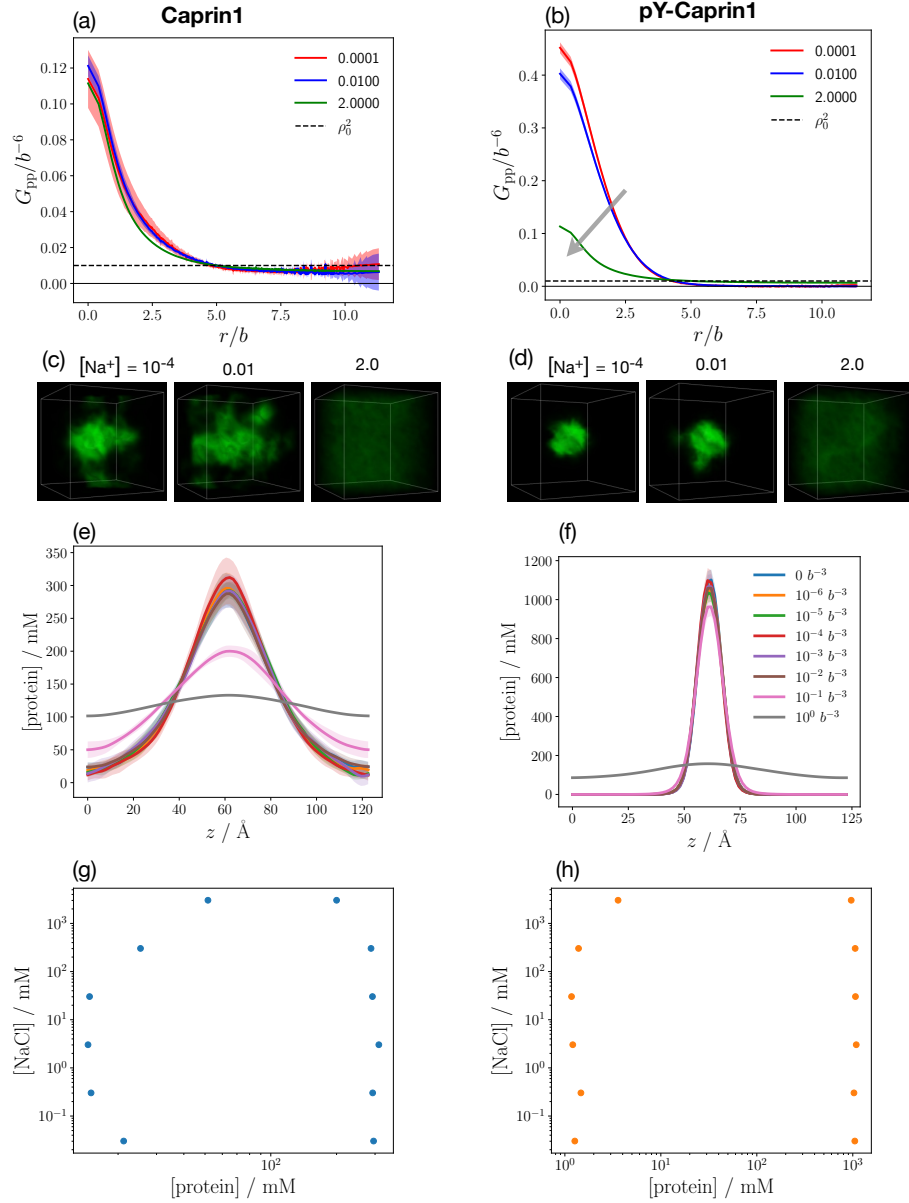


Fig. S4: FTS models for Caprin1 and pY-Caprin1 with only Na^+ and Cl^- but no ATP-Mg. (a,b) Protein-protein correlation functions [maintext Eq. (7)] for Caprin1 (a) and pY-Caprin1 (b) at three different $[\text{Na}^+]$ s, color coded in units of b^{-3} as provided. In each figure, the baseline value of protein-protein correlation function $(\rho_p^0)^2$ (where ρ_p^0 is overall protein concentration) is marked by the horizontal dashed line. Phase separation is indicated by large- r correlation function values falling below this baseline. The grey arrow in (b) marks the direction of increasing $[\text{Na}^+]$. (c,d) Field snapshots for the Caprin1 (c) and pY-Caprin1 (d) systems at different $[\text{Na}^+]$ s. The above results are obtained at Bjerrum length $l_B = 7b$. (e-h) Results from an alternate FTS model using an elongated simulation box similar to that utilized for our explicit-ion coarse-grained MD. (e,f) Protein concentration profiles computed at different NaCl concentrations for Caprin1 (e) and pY-Caprin1 (f) [color code for density profiles provided in (f)]. (g,h) salt-protein phase diagrams obtained from the concentration profiles in (e,f) for Caprin1 (g) and pY-Caprin1 (h).

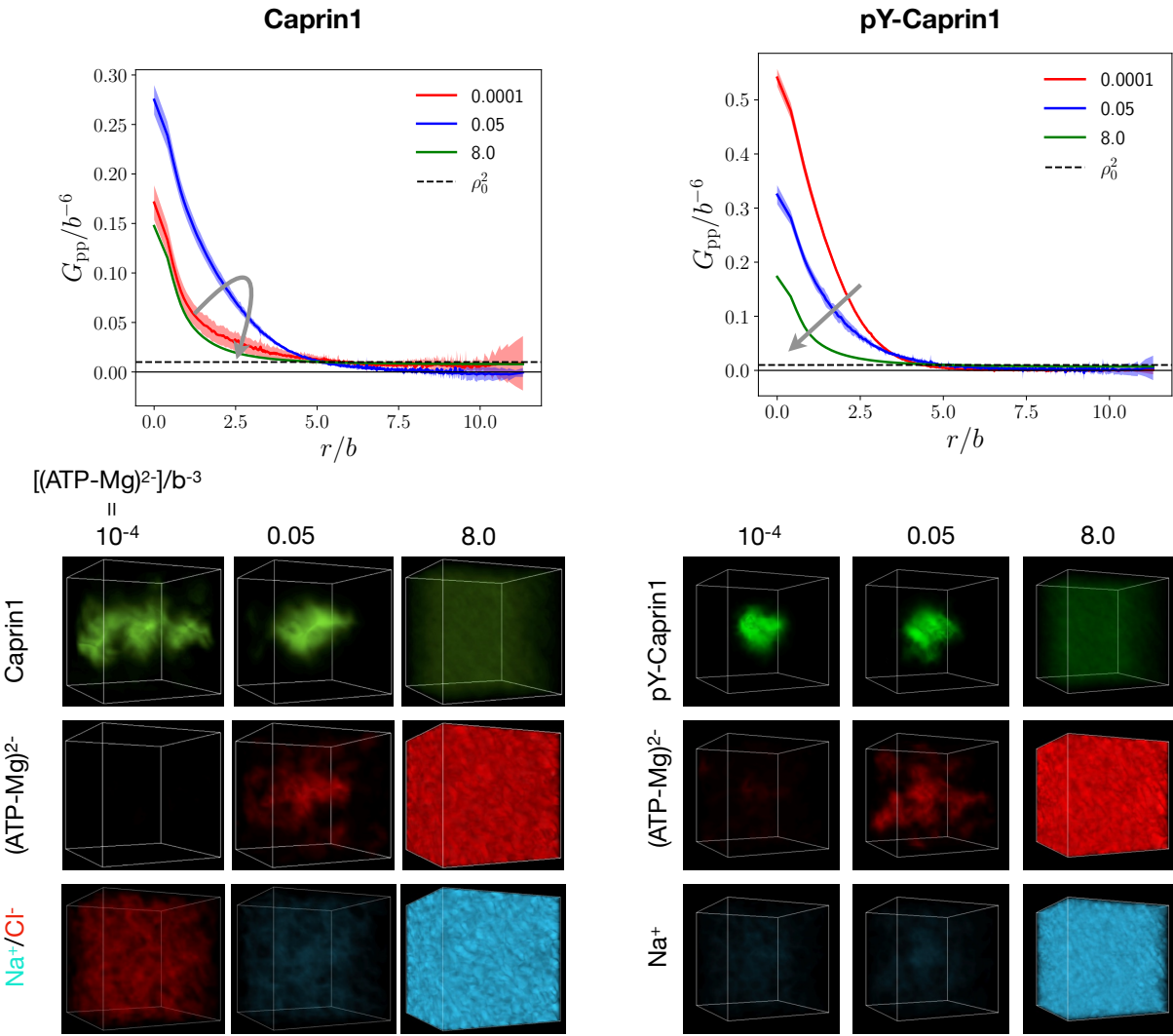


Fig. S5: Alternate FTS models for Caprin1 and pY-Caprin1 with $(ATP-Mg)^{2-}$ and either Na^+ or Cl^- (but not both) to maintain overall electric neutrality. For Caprin1, which has a net positive charge, $(ATP-Mg)^{2-}$ is the counterion. Depending on $[(ATP-Mg)^{2-}]$, either Cl^- is included as an additional counterion (when $[(ATP-Mg)^{2-}]$ is insufficient to balance the positive charges on Caprin1), or Na^+ is included as salt ion (when $[(ATP-Mg)^{2-}]$ overcompensates the positive charges on Caprin1). Na^+ and Cl^- are not included together in this simplified formulation. For pY-Caprin1, which has a net negative charge, Na^+ is used as counterion, and its concentration depends on $[(ATP-Mg)^{2-}]$ in such a way that electric neutrality of the entire system is maintained. Top panels: protein-protein correlation functions at different concentrations of $(ATP-Mg)^{2-}$ (color coded in units of b^{-3} as provided). Horizontal dashed lines are $(\rho_p^0)^2$ baselines as in Fig. S4a,b. Grey arrows indicate increasing $[(ATP-Mg)^{2-}]$. Bottom panels: Field snapshots for system components at different $[(ATP-Mg)^{2-}]$ (as indicated) for the Caprin1 (left panels) and pY-Caprin1 (right panels) systems. Results here are obtained at $l_B = 7b$.

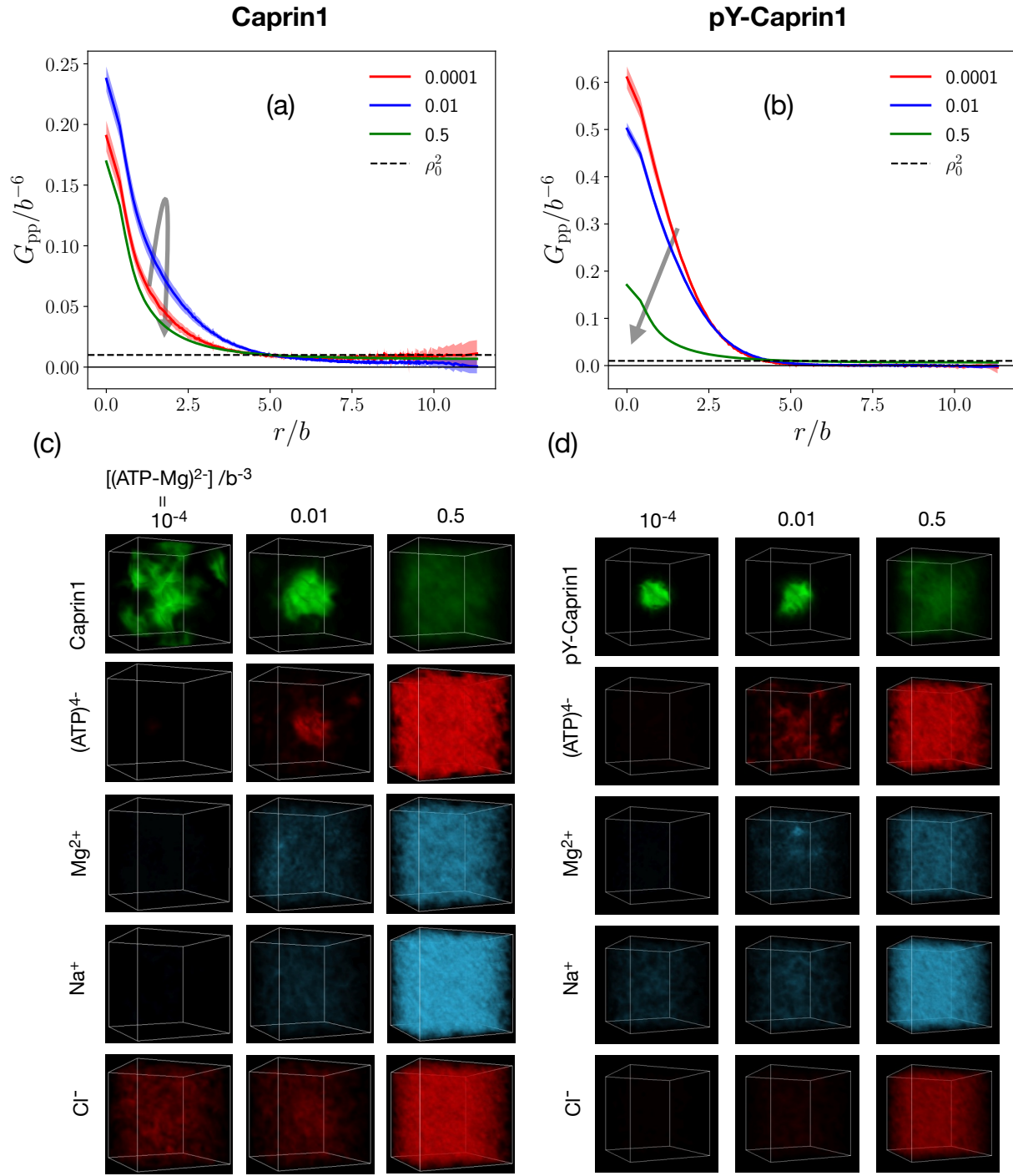


Fig. S6: Alternate FTS models for Caprin1 or pY-Caprin1 with ATP^{4-} , Mg^{2+} , Na^+ and Cl^- , wherein $(ATP-Mg)^{2-}$ is assumed to be fully dissociable. Results are obtained for $l_B = 7b$ and presented in the same style as that in Fig. 8b,c and Fig. 9 of the maintext as well as Fig. S5.

- [1] Shin, Y. & Brangwynne, C. P. Liquid phase condensation in cell physiology and disease. *Science* **357**, eaaf4382 (2017).
- [2] Tsang, B., Pritišanac, I., Scherer, S. W., Moses, A. M. & Forman-Kay, J. D. Phase separation as a missing mechanism for interpretation of disease mutations. *Cell* **183**, 1742–1756 (2020).
- [3] Lyon, A. S., Peebles, W. B. & Rosen, M. K. A framework for understanding the functions of biomolecular condensates across scales. *Nat. Rev. Mol. Cell Biol.* **22**, 215–235 (2021).
- [4] Cinar, H. et al., Temperature, hydrostatic pressure, and osmolyte effects on liquid-liquid phase separation in protein condensates: Physical chemistry and biological implications. *Chem. Eur. J.* **25**, 13049–13069 (2019).
- [5] Bremer, A. et al., Deciphering how naturally occurring sequence features impact the phase behaviours of disordered prion-like domains. *Nat. Chem.* **14**, 196–207 (2022).
- [6] Harmon, T. S., Holehouse, A. S., Rosen, M. K. & Pappu, R. V. Intrinsically disordered linkers determine the interplay between phase separation and gelation in multivalent proteins. *eLife* **6**, e30294 (2017).
- [7] Lin, Y.-H., Forman-Kay, J. D. & Chan, H. S. Theories for sequence-dependent phase behaviours of biomolecular condensates. *Biochemistry* **57**, 2499–2508 (2018).
- [8] Kato, M. & McKnight, S. L. A solid-state conceptualization of information transfer from gene to message to protein. *Annu. Rev. Biochem.* **87**, 351–390 (2018).
- [9] Wurtz, J. D. & Lee, C. F. Stress granule formation via ATP depletion-triggered phase separation. *New J. Phys.* **20**, 045008 (2018).
- [10] McSwiggen, D. T., Mir, M., Darzacq, X. & Tjian, R. Evaluating phase separation in live cells: Diagnosis, caveats, and functional consequences. *Genes Dev.* **33**, 1619–1634 (2019).
- [11] Lin, Y.-H., Wu, H., Jia, B., Zhang, M. & Chan, H. S. Assembly of model postsynaptic densities involves interactions auxiliary to stoichiometric binding. *Biophys. J.* **121**, 157–171 (2022).
- [12] Mittag, T. & Pappu, R. V. A conceptual framework for understanding phase separation and addressing open questions and challenges. *Mol. Cell* **82**, 2201–2214 (2022).
- [13] Shen, Z. et al., Biological condensates form percolated networks with molecular motion properties distinctly different from dilute solutions. *eLife* **12**, 81907 (2023).
- [14] Pappu, R. V., Cohen, S. R., Dar, F., Farag, M. & Kar, M. Phase transitions of associative biomacromolecules. *Chem Rev.* **123**, 8945–8987 (2023).
- [15] Honig, B. & Nicholls, A. Classical electrostatics in biology and chemistry *Science* **268**, 1144–1149 (1995).
- [16] Zhou, H.-X. & Pang, X. Electrostatic interactions in protein structure, folding, binding, and condensation. *Chem. Rev.* **118**, 1691–1741 (2018).
- [17] Nott, T. J. et al., Phase transition of a disordered nuage protein generates environmentally responsive membraneless organelles. *Mol. Cell* **57**, 936–947 (2015).
- [18] Lin, Y.-H., Forman-Kay, J. D. & Chan, H. S. Sequence-specific polyampholyte phase separation in membraneless organelles. *Phys. Rev. Lett.* **117**, 178101 (2016).
- [19] Wang, J. et al., A molecular grammar governing the driving forces for phase separation of

prion-like RNA binding proteins. *Cell* **174**, 688–699 (2018).

[20] Vernon, R. M. et al., Pi-Pi contacts are an overlooked protein feature relevant to phase separation. *eLife* **7**, e31486 (2018).

[21] Murthy, A. C. et al., Molecular interactions underlying liquid-liquid phase separation of the FUS low-complexity domain. *Nat. Struct. Mol. Biol.* **26**, 637–648 (2019).

[22] Cai, H., Vernon, R. M. & Forman-Kay, J. D. An interpretable machine-learning algorithm to predict disordered protein phase separation based on biophysical interactions. *Biomolecules* **12**, 1131 (2022).

[23] Dignon, G. L., Zheng, W., Kim, Y. C. & Mittal, J. Temperature-controlled liquid-liquid phase separation of disordered proteins. *ACS Cent. Sci.* **5**, 821–830 (2019).

[24] Cinar, H. et al., Pressure sensitivity of SynGAP/PSD-95 condensates as a model for postsynaptic densities and its biophysical and neurological ramifications. *Chem. Eur. J.* **26**, 11024–11031 (2020).

[25] Maharana, S. et al., RNA buffers the phase separation behavior of prion-like RNA binding proteins. *Science* **360**, 918–921 (2018).

[26] Tsang, B. et al., Phosphoregulated FMRP phase separation models activity-dependent translation through bidirectional control of mRNA granule formation. *Proc. Natl. Acad. Sci. U.S.A.* **116**, 4218–4227 (2019).

[27] Dutagaci, B. et al., Charge-driven condensation of RNA and proteins suggests broad role of phase separation in cytoplasmic environments. *eLife* **10**, e64004 (2021).

[28] Laghmach, R. et al., RNA chain length and stoichiometry govern surface tension and stability of protein-RNA condensates. *iScience* **25**, 104105 (2022).

[29] Wang, Y., Lomakin, A., Kanai, S., Alex, R. & Benedek, G. B. Liquid–Liquid Phase Separation in Oligomeric Peptide Solutions. *Langmuir* **33**, 7715–7721 (2017).

[30] André, A. A. M. & Spruijt, E. Liquid–liquid phase separation in crowded environments. *Int. J. Mol. Sci.* **21**, 5908 (2020).

[31] Patel, C. K., Singh S., Saini, B. & Mukherjee, T. K. Macromolecular crowding-induced unusual liquid–liquid phase separation of human serum albumin via soft protein–protein interactions. *J. Phys. Chem. Lett.* **13**, 3636–3644 (2022).

[32] Kumari, K., Singh, A. K., Mandal, P. & Rakshit, S. Crowder chain length variability and excluded volume effect on the phase separation behavior of Mucin. *J. Phys. Chem. Lett.* **15**, 10505–10513 (2024).

[33] Kim, T. H. et al., Phospho-dependent phase separation of FMRP and CAPRIN1 recapitulates regulation of translation and deadenylation. *Science* **365**, 825–829 (2019).

[34] Owen, I. & Shewmaker, F. The role of post-translational modifications in the phase transitions of intrinsically disordered proteins. *Int. J. Mol. Sci.* **20**, 5501 (2019).

[35] Snead, W. T. & Gladfelter, A. S. The control centers of biomolecular phase separation: how membrane surfaces, PTMs, and active processes regulate condensation. *Mol. Cell* **76**, 295–305 (2019).

[36] Borg, M. et al., Polyelectrostatic interactions of disordered ligands suggest a physical basis for ultrasensitivity. *Proc. Natl. Acad. Sci. U.S.A.* **104**, 9650–9655 (2007).

[37] Marsh, J. A., Teichmann, S. A. & Forman-Kay, J. D. Probing the diverse landscape of protein flexibility and binding. *Curr. Opin. Struct. Biol.* **22**, 643–650 (2012).

- [38] Song, J., Ng, S. C., Tompa, P., Lee, K. A. W. & Chan, H. S. Polycation- π interactions are a driving force for molecular recognition by an intrinsically disordered oncoprotein family *PLoS Comput. Biol.* **9**, e1003239 (2013).
- [39] Brangwynne, C. P., Tompa, P. & Pappu, R. V. Polymer physics of intracellular phase transitions. *Nat. Phys.* **11**, 899–904 (2015).
- [40] Chen, T., Song, J. & Chan, H. S. Theoretical perspectives on nonnative interactions and intrinsic disorder in protein folding and binding. *Curr. Opin. Struct. Biol.* **30**, 32–42 (2015).
- [41] Wang, Y. et al., Charge segregation in the intrinsically disordered region governs VRN1 and DNA liquid-like phase separation robustness. *J. Mol. Biol.* **433**, 167269 (2021).
- [42] Das, R. K. & Pappu, R. V. Conformations of intrinsically disordered proteins are influenced by linear sequence distributions of oppositely charged residues. *Proc. Natl. Acad. Sci. U.S.A.* **110**, 13392–13397 (2013).
- [43] Sawle, L. & Ghosh, K. A theoretical method to compute sequence dependent configurational properties in charged polymers and proteins. *J. Chem. Phys.* **143**, 085101 (2015).
- [44] Lin, Y.-H. & Chan, H. S. Phase separation and single-chain compactness of charged disordered proteins are strongly correlated. *Biophys. J.* **112**, 2043–2046 (2017).
- [45] Chang, L.-W. et al., Sequence and entropy-based control of complex coacervates. *Nat. Comm.* **8**, 1273 (2017).
- [46] Amin, A. N., Lin, Y.-H., Das, S. & Chan, H. S. Analytical theory for sequence-specific binary fuzzy complexes of charged intrinsically disordered proteins. *J. Phys. Chem. B* **124**, 6709–6720 (2020).
- [47] Lyons, H. et al., Functional partitioning of transcriptional regulators by patterned charge blocks. *Cell* **186**, 327–345 (2023).
- [48] Pal, T., Wessén, J., Das, S. & Chan, H. S. Differential effects of sequence-local versus nonlocal charge patterns on phase separation and conformational dimensions of polyampholytes as model intrinsically disordered proteins. *J. Phys. Chem. Lett.* **15**, 8248–8256 (2024).
- [49] Banerjee, P. R., Milin, A. N., Moosa, M. M., Onuchic, P. L. & Deniz, A. A. Reentrant phase transition drives dynamic substructure formation in ribonucleoprotein droplets. *Angew. Chem. Int. Ed.* **56**, 11354–11359 (2017).
- [50] Krainer, G. et al., Reentrant liquid condensate phase of proteins is stabilized by hydrophobic and non-ionic interactions. *Nat. Comm.* **12**, 1085 (2021).
- [51] Hong, Y. et al., Hydrophobicity of arginine leads to reentrant liquid-liquid phase separation behaviors of arginine-rich proteins. *Nat. Comm.* **13**, 7326 (2022).
- [52] Alshareedah, I. et al., Interplay between short-range attraction and long-range repulsion controls reentrant liquid condensation of ribonucleoprotein-RNA complexes. *J. Am. Chem. Soc.* **141**, 14593–14602 (2019).
- [53] Babinchak, W. M. et al., Small molecules as potent biphasic modulators of protein liquid-liquid phase separation. *Nat. Comm.* **11**, 5574 (2020).
- [54] Bertrand, T. & Lee, C. F. Diversity of phase transitions and phase separations in active fluids. *Phys. Rev. Res.* **4**, L022046 (2022).
- [55] Jain, S. et al., ATPase-modulated stress granules contain a diverse proteome and substructure. *Cell* **164**, 487–498 (2016).
- [56] Guilhas, B. et al., ATP-driven separation of liquid phase condensates in bacteria. *Mol. Cell*

79, 293–303.e4 (2020).

[57] Hayes, M. H., Peuchen, E. H., Dovichi, N. J., Weeks, D. L. Dual roles for ATP in the regulation of phase separated protein aggregates in *Xenopus oocyte* nucleoli. *eLife* **7**, e35224 (2018).

[58] Nguemaha, V. & Zhou, H.-X. Liquid-liquid phase separation of patchy particles illuminates diverse effects of regulatory components on protein droplet formation. *Sci. Rep.* **8**, 6728 (2018).

[59] Ghosh, A., Mazarakos, K. & Zhou, H.-X. Three archetypical classes of macromolecular regulators of protein liquid-liquid phase separation. *Proc. Natl. Acad. Sci. U.S.A.* **116**, 19474–1948 (2019).

[60] Ruff, K. M., Dar, F. & Pappu, R. V. Ligand effects on phase separation of multivalent macromolecules. *Proc. Natl. Acad. Sci. U.S.A.* **118**, e2017184118 (2021).

[61] Wright, R. H. G., Dily, F. L. & Beato, M. ATP, Mg²⁺, nuclear phase separation, and genome accessibility. *Trends Biochem. Sci.* **44**, P565–574 (2019).

[62] Martins, A. C. et al., Assessing the hydrotropic effect in the presence of electrolytes: Competition between solute salting-out and salt-induced hydrotrope aggregation. *Phys. Chem. Chem. Phys.* **24**, 21645–21654 (2022).

[63] Patel, A. et al., ATP as a biological hydrotrope. *Science* **356**, 753–756 (2017).

[64] Tian, Z. & Qian, F. Adenosine triphosphate-induced rapid liquid-liquid phase separation of a model IgG1 mAb. *Mol. Pharmaceutics* **18**, 267–274 (2021).

[65] Kota, D., Prasad, R. & Zhou, H.-X. Adenosine triphosphate mediates phase separation of disordered basic proteins by bridging intermolecular interaction networks. *J. Am. Chem. Soc.* **146**, 1326–1336.

[66] Kang, J., Lim, L. & Song, J. ATP enhances at low concentrations but dissolves at high concentrations liquid-liquid phase separation (LLPS) of ALS/FTD-causing FUS. *Biochem. Biophys. Res. Comm.* **504**, 545–551 (2018).

[67] Kang, J., Lim, L., Lu, Y. & Song, J. A unified mechanism for LLPS of ALS-FTLD-causing FUS as well as its modulation by ATP and oligonucleic acids. *PLoS Biol.* **17**, e3000327 (2019).

[68] Ren, C.-L., Shan, Y., Zhang, P., Ding, H.-M. & Ma, Y.-Q. Uncovering the molecular mechanism for dual effect of ATP on phase separation in FUS solution. *Sci. Adv.* **8**, eab07885 (2022).

[69] Dang, M., Lim, L., Kang, J. & Song, J. ATP biphasically modulates LLPS of TDP-43 PLD by specifically binding arginine residues. *Comm. Biol.* **4**, 714 (2021).

[70] Zhou, Q. et al., ATP regulates RNA-driven cold inducible RNA binding protein phase separation. *Protein Sci.* **30**, 1438–1453 (2021).

[71] Lin, Y.-H., Brady, J. P., Chan, H. S. & Ghosh, K. A unified analytical theory of heteropolymers for sequence-specific phase behaviors of polyelectrolytes and polyampholytes. *J. Chem. Phys.* **152**, 045102 (2020).

[72] MacAinsh, M., Dey, S. & Zhou, H.-X. Direct and indirect salt effects on homotypic phase separation. *eLife* preprint (2024) <https://elifesciences.org/reviewed-preprints/100282>; doi: <https://doi.org/10.1101/2024.05.26.596000>.

[73] Solomon, S. et al., Distinct structural features of caprin-1 mediate its interaction with G3BP-

1 and its induction of phosphorylation of eukaryotic translation initiation factor 2 α , entry to cytoplasmic stress granules, and selective interaction with a subset of mRNAs. *Mol. Cell. Biol.* **27**, 2324–2342 (2007).

[74] Towers, E. R., Kelly, J. J., Sud, R., Gale, J. E. & Dawson, S. J. Caprin-1 is a target of the deafness gene Pou4f3 and is recruited to stress granules in cochlear hair cells in response to ototoxic damage. *J. Cell Sci.* **124**, 1145–1155 (2011).

[75] Vu, L. et al., Defining the Caprin-1 interactome in unstressed and stressed conditions. *J. Proteome Res.* **20**, 3165–3178 (2021).

[76] Song, D. et al., Yin and yang regulation of stress granules by Caprin-1. *Proc. Natl. Acad. Sci. U.S.A.* **119**, e2207975119 (2022).

[77] El Fatimy, R. et al., Fragile X mental retardation protein interacts with the RNA-binding protein Caprin1 in neuronal RiboNucleoProtein complexes. *PLoS ONE* **7**, e39338 (2012).

[78] Ellis, J. A. & Luzio, J. P. Identification and characterization of a novel protein (p137) which transcytoses bidirectionally in Caco-2 cells. *J. Biol. Chem.* **270**, 20717–20723 (1995).

[79] Wang, B., David, M. D. & Schrader, J. W. Absence of Caprin-1 results in defects in cellular proliferation. *J. Immunol.* **175**, 4274–4282 (2005).

[80] Nakayama, K. et al., RNG105/caprin1, an RNA granule protein for dendritic mRNA localization, is essential for long-term memory formation. *eLife* **6**, e29677 (2017).

[81] Yang, T., Huang, L., Qin, H. & Mai, S. TRESS granule-associated RNA-binding protein CAPRIN1 drives cancer progression and regulates treatment response in nasopharyngeal carcinoma. *Med. Oncol.* **40**, 47 (2022).

[82] Pavinato, L. et al., CAPRIN1 haploinsufficiency causes a neurodevelopmental disorder with language impairment, ADHD and ASD. *Brain* **146**, 534–548 (2023).

[83] Wong, L. E., Kim, T. H., Muhandiram, D. R., Forman-Kay, J. D. & Kay, L. E. NMR experiments for studies of dilute and condensed protein phases: Application to the phase-separating protein CAPRIN1. *J. Am. Chem. Soc.* **142**, 2471–2489 (2020).

[84] Kim, T. H. et al., Interaction hot spots for phase separation revealed by NMR studies of a CAPRIN1 condensed phase. *Proc. Natl. Acad. Sci. U.S.A.* **118**, e2104897118 (2021).

[85] Toyama, Y., Rangadurai, A. K., Forman-Kay, J. D. & Kay, L. E. Mapping the per-residue surface electrostatic potential of CAPRIN1 along its phase-separation trajectory. *Proc. Natl. Acad. Sci. U.S.A.* **119**, e2210492119 (2022).

[86] Hornbeck, P. V. et al., PhosphoSitePlus, 2014: mutations, PTMs and recalibrations. *Nucl. Acids Res.* **43**, D512–520 (2015).

[87] Monahan, Z. et al., Phosphorylation of the FUS low-complexity domain disrupts phase separation, aggregation, and toxicity. *EMBO J.* **36**, 2951–2967 (2017).

[88] Dignon, G. L., Zheng, W., Kim, Y. C., Best, R. B. & Mittal, J. Sequence determinants of protein phase behavior from a coarse-grained model. *PLoS Comput. Biol.* **14**, e1005941 (2018).

[89] Carlson, C. R. et al., Phosphoregulation of phase separation by the SARS-CoV-2 N protein suggests a biophysical basis for its dual functions. *Mol. Cell* **80**, 1092–1103.e4 (2020).

[90] Das, S., Eisen, A., Lin, Y.-H. & Chan, H. S. A lattice model of charge-pattern-dependent polyampholyte phase separation. *J. Phys. Chem. B* **122**, 5418–5431 (2018).

[91] McCarty, J., Delaney, K. T., Danielsen, S. P. O., Fredrickson, G. H. & Shea, J.-E. Complete

phase diagram for liquid-liquid phase separation of intrinsically disordered proteins. *J. Phys. Chem. Lett.* **10**, 1644–1652 (2019).

[92] Danielsen, S. P. O., McCarty, I., Shea, J.-E., Delaney, K. T. & Fredrickson, G. H. Small ion effects on self-coacervation phenomena in block polyampholytes. *J. Chem. Phys.* **151**, 034904 (2019).

[93] Choi, J.-M., Dar, F. & Pappu, R. V. LASSI: A lattice model for simulating phase transitions of multivalent proteins. *PLoS Comput. Biol.* **15**, e1007028 (2019).

[94] Das, S., Lin, Y.-H., Vernon, R. M., Forman-Kay, J. D. & Chan, H. S. Comparative roles of charge, π , and hydrophobic interactions in sequence-dependent phase separation of intrinsically disordered proteins. *Proc. Natl. Acad. Sci. U.S.A.* **117**, 28795–28805 (2020).

[95] Hazra, M. K. & Levy, Y. Charge pattern affects the structure and dynamics of polyampholyte condensates. *Phys. Chem. Chem. Phys.* **22**, 19368–19375 (2020).

[96] Joseph, J. A. et al., Physics-driven coarse-grained model for biomolecular phase separation with near-quantitative accuracy. *Nat. Comput. Sci.* **1**, 732–743 (2021).

[97] Lin, Y.-H., Wessén, J., Pal, T., Das, S. & Chan, H.S. Numerical techniques for applications of analytical theories to sequence-dependent phase separations of intrinsically disordered proteins, in *Phase-Separated Biomolecular Condensates, Methods and Protocols; Methods in Molecular Biology* 2563 (eds. Zhou, H.-X., Spille, J.-H. & Banerjee, P. R.) 51–94 (Humana Press, 2023).

[98] Pal, T., Wessén, J., Das, S. & Chan, H. S. Subcompartmentalization of polyampholyte species in organelle-like condensates is promoted by charge-pattern mismatch and strong excluded-volume interaction. *Phys. Rev. E* **103**, 042406 (2021).

[99] Shen, K. & Wang, Z.-G. Electrostatic correlations and the polyelectrolyte self energy. *J. Chem. Phys.*, **146**, 084901 (2017).

[100] Dobrynin, A. V. & Rubinstein, M. Theory of polyelectrolytes in solutions and at surfaces. *Prog. Polym. Sci.* **30**, 1049–1118 (2005).

[101] Wessén, J., Pal, T., Das, S., Lin, Y.-H. & Chan, H. S. A simple explicit-solvent model of polyampholyte phase behaviors and its ramifications for dielectric effects in biomolecular condensates. *J. Phys. Chem. B* **125**, 4337–4358 (2021).

[102] Mahdi, K. A. & Olvera de la Cruz, M. Phase diagrams of salt-free polyelectrolyte semidilute solutions. *Macromolecules* **33**, 7649–7654 (2000).

[103] Ermoshkin, A. V & Olvera de la Cruz, M. A modified random phase approximation of polyelectrolyte solutions. *Macromolecules* **36**, 7824–7832 (2003).

[104] Orkoulas, G., Kumar, S. K. & Panagiotopoulos, A. Z. Monte Carlo study of Coulombic criticality in polyelectrolytes. *Phys. Rev. Lett.* **90**, 048303 (2003).

[105] Muthukumar, M. 50th Anniversary perspective: A perspective on polyelectrolyte solutions. *Macromolecules* **50**, 9528–9560 (2017).

[106] Muthukumar, M. Double screening in polyelectrolyte solutions: Limiting laws and crossover formulas. *J. Chem. Phys.* **105**, 5183–5199 (1996).

[107] Budkov, Yu. A., Kolesnikov, A. L., Georgi, N., Nogovitsyn, E. A. & Kiselev, M. G. A new equation of state of a flexible-chain polyelectrolyte solution: Phase equilibria and osmotic pressure in the salt-free case. *J. Chem. Phys.*, **142**, 174901 (2015).

[108] Shen, K. & Wang, Z.-G. Polyelectrolyte chain structure and solution phase behavior. *Macro-*

molecules **51**, 1706–1717 (2018).

[109] Dill, K. A., Alonso, D. O. V. & Hutchinson, K. Thermal stabilities of globular proteins. *Biochemistry* **28**, 5439–5449 (1989).

[110] Kaya, H. & Chan, H. S. Simple two-state protein folding kinetics requires near-Levinthal thermodynamic cooperativity. *Proteins: Struct. Funct. Genet.* **52**, 510–523 (2003).

[111] Statt, A., Casademunt, H., Brangwynne, C. P. & Panagiotopoulos, A. Z. Model for disordered proteins with strongly sequence-dependent liquid phase behavior. *J. Chem. Phys.* **152**, 075101 (2020).

[112] Eisenberg, H. & Mohan, G. R. Aqueous solutions of polyvinylsulfonic acid: Phase separation and specific interactions with ions, viscosity, conductance and potentiometry. *J. Phys. Chem.* **63**, 671–680 (1959).

[113] Zhang, P., Alsaifi, N. M., Wu, J. & Wang, Z.-G. Salting-out and salting-in of polyelectrolyte solutions: A liquid-state theory study. *Macromolecules* **49**, 9720–9730 (2016).

[114] Silmore, K. S., Howard, M. P. & Panagiotopoulos, A. Z. Vapor-liquid phase equilibrium and surface tension of fully flexible Lennard-Jones chains. *Mol. Phys.* **115**, 320–327 (2017).

[115] Shimizu, S. & Chan, H. S. Configuration-dependent heat capacity of pairwise hydrophobic interactions. *J. Am. Chem. Soc.* **129**, 2083–2084 (2001).

[116] Regy, R. M., Thompson, J., Kim, Y. C. & Mittal, J. Improved coarse-grained model for studying sequence dependent phase separation of disordered proteins. *Protein Sci.* **30**, 1371–1379 (2021).

[117] Dannenhoffer-Lafage, T. & Best, R. B. A data-driven hydrophobicity scale for predicting liquid–liquid phase separation of proteins. *J. Phys. Chem. B* **125**, 4046–4056 (2021).

[118] Tesei, G., Schulze, T. K., Crehuet, R. & Lindorff-Larsen, K. Accurate model of liquid–liquid phase behavior of intrinsically disordered proteins from optimization of single-chain properties. *Proc. Natl. Acad. Sci. U.S.A.* **118**, e2111696118 (2021).

[119] Wessén, J., Das, S., Pal, T. & Chan, H. S. Analytical formulation and field-theoretic simulation of sequence-specific phase separation of proteinlike heteropolymers with short- and long-spatial-range interactions. *J. Phys. Chem. B* **126**, 9222–9245 (2022). Correction: *J. Phys. Chem. B* **127**, 11100 (2023).

[120] Zheng, W. et al., Molecular details of protein condensates probed by microsecond long atomistic simulations. *J. Phys. Chem. B* **124**, 11671–11679 (2020).

[121] Brady, J. P. et al., Structural and hydrodynamic properties of an intrinsically disordered region of a germ cell-specific protein on phase separation. *Proc. Natl. Acad. Sci. U.S.A.* **114**, E8194–E8203 (2017).

[122] Fredrickson, G. H. *The Equilibrium Theory Of Inhomogeneous Polymers*; Oxford University Press Inc.:New York, 2006.

[123] Parisi, G. On complex probabilities. *Phys. Lett. B* **131**, 393–395 (1983).

[124] Klauder, J. R. A Langevin approach to fermion and quantum spin correlation functions. *J. Phys. A: Math. Gen.* **16**, L317–L319 (1983).

[125] Parisi, G. & Wu, Y.-S. Perturbation theory without gauge fixing. *Scientia Sinica* **24**, 483–496 (1981).

[126] Chan, H. S. & Halpern, M. B. New ghost-free infrared-soft gauges. *Phys. Rev. D* **33**, 540–547 (1986).

- [127] Fredrickson, G. H., Ganesan, V. & Drolet, F. Field-theoretic computer simulation methods for polymers and complex fluids. *Macromolecules* **35**, 16–39 (2002).
- [128] Lin, Y. et al., Narrow equilibrium window for complex coacervation of tau and RNA under cellular conditions. *eLife* **8**, e42571 (2019).
- [129] Garaizar, A. & Espinosa, J. R. Salt dependent phase behavior of intrinsically disordered proteins from a coarse-grained model with explicit water and ions. *J. Chem. Phys.* **155**, 125103 (2021).
- [130] Jedlinska, Z. M. & Riggleman, R. A. The effect of monomer polarizability on the stability and salt partitioning in model coacervates. *Soft Matter* (2023) DOI: 10.1039/D3SM00706E
- [131] Hazra, M. & Levy, Y. Cross-talk of cation- π interactions with electrostatic and aromatic interactions: A salt-dependent trade-off in biomolecular condensates. *J. Phys. Chem. Lett.* **14**, 8460–8469 (2023).
- [132] Kim, S. et al., Salt triggers the simple coacervation of an underwater adhesive when cations meet aromatic π electrons in seawater. *ACS Nano* **11**, 6764–6772 (2017).
- [133] Wadsworth, G. M. et al., RNAs undergo phase transitions with lower critical solution temperatures. *Nat. Chem.* **15**, 1693–1704 (2023).
- [134] Morishita, K., Watanabe, K., Naguro, I. & Ichijo, H. Sodium ion influx regulates liquidity of biomolecular condensates in hyperosmotic stress response. *Cell Rep.* **42**, 112315 (2023).
- [135] Fetahaj, Z., Ostermeier, L., Cinar, H., Oliva, R. & Winter, R. Biomolecular condensates under extreme Martian salt conditions. *J. Am. Chem. Soc.* **143**, 5247–5259 (2021).
- [136] Tesei, G. et al., Self-association of a highly charged arginine-rich cell-penetrating peptide. *Proc. Natl. Acad. Sci. U.S.A.* **114**, 11428–11433 (2017).
- [137] Liu, B. R., Chiou, S.-H., Huang, Y.-W. & Lee, H.-J. Bio-membrane internalization mechanisms of arginine-rich cell-penetrating peptides in various species. *Membranes* (Basel) **12**, 88 (2022).
- [138] Radhakrishna M. et al., Molecular connectivity and correlation effects on polymer coacervation. *Macromolecules* **50**, 3030– (2017).
- [139] Li, L. et al., Phase behavior and salt partitioning in polyelectrolyte complex coacervates. *Macromolecules* **51**, 2988–2995 (2018).
- [140] Herrera, S. E. et al., Polyelectrolyte-multivalent molecule complexes: physicochemical properties and applications. *Soft Matter* **19**, 2013–2041 (2023).
- [141] Qian, D. et al., Tie-line analysis reveals interactions driving heteromolecular condensate formation. *Phys. Rev. X* **12**, 041038 (2022).
- [142] Olvera de la Cruz, M. et al., Precipitation of highly charged polyelectrolyte solutions in the presence of multivalent salts. *J. Chem. Phys.* **103**, 5781–5791 (1995).
- [143] Lenton, S. et al., Impact of arginine-phosphate interactions on the reentrant condensation of disordered proteins. *Biomacromolecules* **22**, 1532–1544 (2021).
- [144] Crabtree, M. D. et al., Ion binding with charge inversion combined with screening modulates DEAD box helicase phase transitions. *Cell Rep.* **42**, 113375 (2023).
- [145] Nakashima, K. K., Baaij, J. F. & Spruijt, E. Reversible generation of coacervate droplets in an enzymatic network. *Soft Matter* **14**, 361–367 (2018).
- [146] Wessén, J., Pal, T. & Chan, H. S. Field theory description of ion association in phase separation of polyampholytes. *J. Chem. Phys.* **156**, 194903 (2022).

- [147] Adhikari, S., Leaf, M. A. & Muthukumar, M. Polyelectrolyte complex coacervation by electrostatic dipolar interactions. *J. Chem. Phys.* **149**, 163308 (2018).
- [148] Li, L., Rumyantsev, A. M., Srivastava, S., Meng, S., de Pablo, J. J. & Tirrell, M. V. Effect of solvent quality on the phase behavior of polyelectrolyte complexes. *Macromolecules* **54**, 105–114 (2021).
- [149] Ali, S., Bleuel, M. & Prabhu, V. M. Lower critical solution temperature in polyelectrolyte complex coacervates. *ACS Macro Lett.* **8**, 289–293 (2019).
- [150] Wiesner, S. et al., A change in conformational dynamics underlies the activation of Eph receptor tyrosine kinases. *EMBO J.* **25**, 4686–4696 (2006).
- [151] Stratonovich, R. L. On a method of calculating quantum distribution functions. *Soviet Physics Doklady* **2**, 416–419 (1958).
- [152] Hubbard, J. Calculation of partition functions. *Phys. Rev. Lett.* **3**, 77–78 (1959).
- [153] Lin, Y.-H., Song, J., Forman-Kay, J. D. & Chan, H. S. Random-phase-approximation theory for sequence-dependent, biologically functional liquid-liquid phase separation of intrinsically disordered proteins. *J. Mol. Liq.* **228**, 176–193 (2017).
- [154] Lin, Y. -H., Brady, J. P., Forman-Kay J. D. & Chan, H. S. Charge pattern matching as a ‘fuzzy’ mode of molecular recognition for the functional phase separations of intrinsically disordered proteins. *New J. Phys.* **19**, 115003 (2017).
- [155] Anderson, J. A., Glaser, J. & Glotzer, S. C. HOOMD-blue: A Python package for high-performance molecular dynamics and hard particle Monte Carlo simulations. *Comput. Mater. Sci.* **173**, 109363 (2020).
- [156] Anderson, J. A., Lorenz, C. D. & Travesset, A. General purpose molecular dynamics simulations fully implemented on graphics processing units. *J. Comput. Phys.* **227**, 5342–5359 (2008).
- [157] Dignon, G. L., Zheng, W. & Mittal, J. Simulation methods for liquid–liquid phase separation of disordered proteins. *Curr. Opin. Chem. Eng.* **23**, 92–98 (2019).
- [158] Das, S., Amin, A. N., Lin, Y.-H. & Chan, H. S. Coarse-grained residue-based models of disordered protein condensates: Utility and limitations of simple charge pattern parameters. *Phys. Chem. Chem. Phys.* **20**, 28558–28574 (2018).
- [159] Joung, I. S. & Cheatham, T. E. 3rd. Determination of alkali and halide monovalent ion parameters for use in explicitly solvated biomolecular simulations. *J. Phys. Chem. B* **112**, 9020–9041 (2008).
- [160] Tros, M., Zheng, L., Hunger, J., Bonn, M., Bonn, D., Smits, G. J. & Woutersen, S. Picosecond orientational dynamics of water in living cells. *Nat. Commun.* **8**, 904 (2017).
- [161] Kim, Y. C. & Hummer, G. Coarse-grained models for simulations of multiprotein complexes: Application to ubiquitin binding. *J. Mol. Biol.* **375**, 1416–1433 (2008).
- [162] Miyazawa, S. & Jernigan, R. L. Residue-residue potentials with a favourable contact pair term and an unfavourable high packing density term, for simulation and threading. *J. Mol. Biol.* **256**, 623–644 (1996).
- [163] Martyna, G. J., Tobias, D. J. & Klein, M. L. Constant pressure molecular dynamics algorithms. *J. Chem. Phys.* **101**, 4177–4189 (1994).
- [164] Tuckerman, M. E., Alejandre, J., López-Rendón, R., Jochim , A. L. & Martyna G. J. A Liouville-operator derived measure-preserving integrator for molecular dynamics simulations

in the isothermal–isobaric ensemble. *J. Phys. A: Math. Gen.* **39**, 5629–5651 (2006).

- [165] LeBard, D. N., Levine, B. G., Mertmann, P., Barr, S. A., Jusufi, A., Sanders, S., Klein, M. L. & Panagiotopoulos, A. Z. Self-assembly of coarse-grained ionic surfactants accelerated by graphics processing units. *Soft Matter* **8**, 2385–2397 (2012).
- [166] Wang, Z.-G. Fluctuation in electrolyte solutions: The self energy. *Phys. Rev. E* **81**, 021501 (2010).
- [167] Lennon, E. M., Mohler, G. O., Ceniceros, H. D., Garca-Cervera, C. J. & Fredrickson, G. H. Numerical solutions of the complex Langevin equations in polymer field theory. *Multiscale Modeling & Simulation* **6**, 1347–1370 (2008).